# Fabrication, Characterization and Optical Properties of Three-dimensional Colloidal Gold Nanostructures

by

Christopher James Addison
B.Sc. (Hons), University of Victoria, 2002

A Thesis Submitted in Partial Fulfillment of the
Requirements for the Degree of

MASTER OF SCIENCE

in the Department of Chemistry

Supervisor: Dr. A.G. Brolo

## ABSTRACT

3-Dimensional nanostructures were constructed through the alternate immersion of a derivatized glass slide in solutions of propanedithiol and gold nanoparticles. The size and shape of the surface features could be controlled based on the number of nanoparticle depositions. Characterization of the substrates was performed using UV-Vis spectroscopy and atomic force microscopy. The multilayer nanoparticle substrates were examined for their suitability in surface-enhanced Raman scattering (SERS) by obtaining the SERS spectrum of oxazine-720 on the substrates. A dramatic increase in the SERS signal is noted with increasing nanoparticle layers and reaches a maximum for 11 nanoparticle-layer depositions. The enhancement is attributed to the underlying surface morphology: Surface features on the order of 40 nm in size yield the greatest SERS enhancement due to surface plasmon (SP) excitation.

The non-linear optical properties of colloidal nanostructures were examined using second harmonic generation (SHG). A pronounced second harmonic emission was noted for 13 nanoparticle layers and was attributed to SP excitation to yield surface-enhanced SHG.

The self-assembly of gold nanorods to form 3-dimensional nanostructures was examined. While the self-assembly was not successful, the aggregated gold nanorods exhibited a large SERS enhancement. This suggests that the incorporation of gold nanorods into SERS substrates is a viable avenue for future research.

## Table of Contents

## List of Figures and Illustrations

## List of Abbreviations

| | |
|---|---|
| 4-ATP | 4-aminothiophenol |
| 4-CTP | 4-carboxythiophenol |
| AFM | Atomic force microscope/microscopy |
| AR | Aspect ratio |
| CT | Charge-transfer |
| CTAB | Cetyltrimethylammonium bromide |
| EM | Electromagnetic |
| ESA | Effective surface area |
| FIB | Focussed ion beam |
| FWHM | Full-width at half maximum |
| HOMO | Highest occupied molecular orbital |
| HWHM | Half-width at half-maximum |
| IR | Infrared spectroscopy |
| JPEG | Joint photographic experts group |
| LSP | Localized surface plasmon |
| LUMO | Lowest unoccupied molecular orbital |
| MPC | Monolayer-protected cluster |
| MPTMS | 3-mercaptopropyltrimethoxy silane |
| NLO | Non-linear optical |
| NP | Nanoparticle |
| NR | Nanorod |
| NSL | Nanosphere lithography |
| PAH | poly(allylamine hydrochloride) |
| PDDA | poly(diallyldimethylammonium chloride) |
| PDT | Propanedithiol |
| PPA | Periodic particle array |
| PS | Polystyrene |
| PSS | poly(sodium 4-styrenesulfonate) |
| RMS | Root-mean-square |
| SERRS | Surface-enhanced resonant-Raman scattering |
| SERS | Surface-enhanced Raman scattering |
| SESHG | Surface-enhanced second harmonic generation |
| SH | Second harmonic |
| SHG | Second harmonic generation |
| SP | Surface Plasmon |
| SSHG | Surface second harmonic generation |
| TEM | Transmission electron microscope/microscopy |
| UV | Ultraviolet |
| UV-Vis | Ultraviolet-visible spectroscopy |

**Acknowledgements**

There are too many people to thank, and certainly not enough space. Many people have helped me along the way and I would be amiss if I forgot to mention someone! Therefore, I offer this simple thanks:

*Those that have helped know who they are, and to them I say "Thank you".*

**Dedication**

*For Joshua*

May your yields be high, your products pure, and your experiments always successful!

I hope your interest in science continues to flourish

# Chapter One: Introduction

## 1.1 Research Objectives

The main objective of this research project was to construct and characterize a spectroscopic substrate consisting of alternating layers of colloidal gold and a dithiol linker molecule anchored onto a modified glass substrate. The overall structure of the substrate is shown in Figure 1-1:

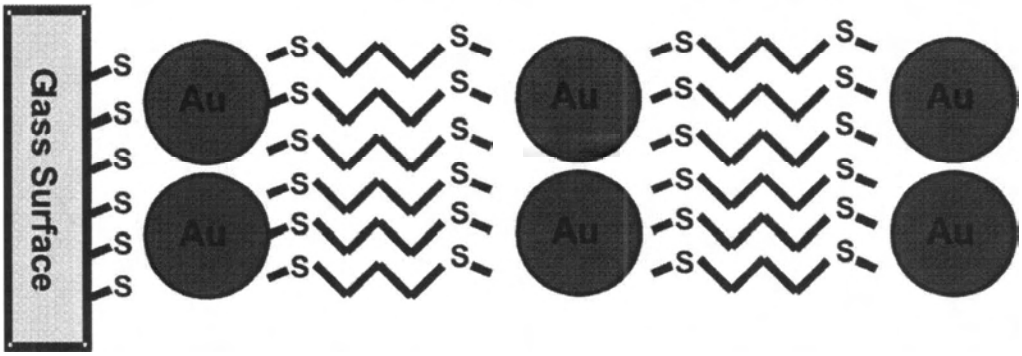


**Figure 1-1: Schematic of the proposed nanoparticle assembly consisting of alternating layers of colloidal gold and dithiol linker molecules anchored to a modified glass substrate. Here, a substrate consisting of 3 nanoparticle layers is shown.**

The modification of the glass substrate was accomplished through a silanization that results in a pendant thiol group protruding from the glass surface [1]. Using the well-known gold-thiol chemistry, a layer of colloidal gold was deposited onto the modified

glass surface using self-assembly techniques. While extensive research has already been performed on monolayers of colloidal gold deposited on glass [2-8], there exists a gap in the research of multilayer assemblies.

After assembly of one colloid layer, the substrate was immersed in a solution of a dithiol linker molecule, propanedithiol (PDT). One of the thiol moieties will attach to the colloid surface, while the other will remain unreacted [9-12]. This thiol group was then used to attach a subsequent layer of colloids. This process was repeated until the desired number of colloid layers was achieved.

The substrates were characterized using ultraviolet-visible spectroscopy (UV-Vis). Surface features and roughness were examined using Atomic Force Microscopy (AFM).

Subsequently, the substrates were coated with the Raman-active molecule Oxazine-720 for analysis using surface-enhanced Raman scattering (SERS). The SERS response of the substrates was correlated with the roughness features obtained from AFM to determine the optimum surface roughness for maximum enhancement of the Raman signal.

As an additional aspect to this research, the non-linear optical (NLO) properties of the spectroscopic substrates was examined by measuring their second harmonic generation (SHG).

One proposed extension of this work is to use anisotropic nanoparticles to construct spectroscopic substrates. Gold nanorods were synthesized, and their deposition onto glass substrates was attempted.

## 1.2 Structure of this thesis

A general introduction to the work performed in this thesis is provided in Chapter One. Chapter Two provides details about the experimental aspects of this research. Characterization of the synthesized colloidal gold using UV-Vis spectroscopy and transmission electron microscopy (TEM) is discussed in Chapter Three. Chapter Four deals with construction of the colloid multilayer nanostructures, and their characterization using UV-Vis spectroscopy and AFM. The suitability of these colloid multilayer structures as substrate for SERS is examined in Chapter Five. These substrates are then examined for their NLO properties using SHG in Chapter Six. The possibility of using anisotropic gold nanoparticles (nanorods) is discussed in Chapter Seven, and preliminary results are presented there. A summary of the results obtained in this thesis are presented and discussed in Chapter Eight.

## 1.3 Colloidal Gold

Gold, in all of its forms, has fascinated mankind for many centuries. Elemental gold has a long, intertwined history with civilization: Metallic gold was a sign of power and wealth that continues to this day. Another form of gold also managed to capture the interest of people thousands of years ago: Colloidal gold. Roughly defined, a colloid

describes the stable dispersion of one phase in another. In particular, it is often assumed to mean a suspension of metal nanoparticles (NP) in a liquid medium.

In the medieval era, gold colloids were used as a colouring pigment in stained glass windows. The intense ruby-red colour yielded beautiful results in many stained glass windows of Europe. The Rose Window at the Cathedral of Notre Dame in Paris is a well-known example of its use [13].

Since the Egyptian era, it was believed that colloidal gold possessed metaphysical and healing powers [14]. The idea that blood was equal to the life-essence, and the active principle of blood was redness, was widely accepted prior to the development of modern medicine. Because of the colour similarity between colloidal gold and blood, it was believed that colloidal gold was capable of curing many diseases, prolonging life, improving strength and rejuvenation [14]. By the eighteenth century, with advances in medicine came the realization that this concoction did not possess any medicinal quality: These colloidal solutions consisted of nothing more than tiny "chunks" of gold floating in an oily liquid.

In the seventeenth century, Paracelsus described the preparation of "*aurum potabile, oleum auri; uinta essential auri*" through the reduction of auric chloride with an alcoholic extract of plants [15]. One of the initial scientific studies into the nature of colloids was conducted by Faraday in 1857 [16]. Faraday was able to obtain stable, highly dispersive hydrosols of gold through the treatment of chlorauric acid with a variety of different

reducing agents. Faraday observed the influence of concentration and purity of the solutions on their colour, turbidity and stability [16]. Faraday also noted the dramatic colour change from red to blue upon the addition of electrolytes: Addition of electrolytes induces agglomeration of the minute gold particles, too small to be observed under a microscope, into larger aggregates that would eventually settle out [16]. His studies also showed that this aggregation could be avoided through the use of "protecting molecules" such as gelatin [16]. To this day, Faraday's samples of colloids reside at the Royal Institute of London – testament to the fact that colloidal gold solutions are extremely robust and possess long-term stability [16].

Near the turn of the twentieth century, the field of colloid chemistry was experiencing substantial growth through the works of Ostwald [17], Mie [18], and the Nobel-prize winning contributions of Svedberg and Zsigmondy [19, 20]. A multitude of reducing agents were found to produce colloidal gold. Yet all of the methods had major drawbacks and lacked reproducibility. The synthetic methods for producing colloidal gold will be discussed further in Section 1.3.1.

The size decrease from the bulk to the nanoscale also has dramatic effects upon the optical properties of a material. The pioneering work of Mie in 1908 revealed the nature of the ruby-red colour of gold nanoparticles by solving Maxwell's equation [18]. In essence, the colour is due to the coherent oscillation of the conduction band electrons interacting with an electromagnetic field [21]: a phenomenon known as surface plasmons (SP). Because spectroscopic methods yield information about the energy states for

allowed transitions, the change in electronic states results in very noticeable changes in the optical absorption spectra of nanoscale materials. For example, while bulk gold is yellow in colour, gold nanoparticles are an intense wine-red colour. This topic will be addressed further in Section 1.3.2.

Interest in the field waned, and colloidal gold was relatively forgotten until the publication of a landmark paper by Frens which described a simple and effective method for the production of colloidal gold using sodium citrate as a reducing agent [22]. Because it yields colloids of uniform and controllable size, the Frens paper has become one of the most useful papers in the field of colloidal science, and has been credited with reviving interest in the field itself [23].

It is important to note that in this work, the term colloidal gold and gold nanoparticle will be used interchangeably and seamlessly, as is the general custom in the field.

### 1.3.1 Synthetic Approaches

As discussed above, a variety of esoteric reagents were used to synthesize colloidal gold, prior to the work of Frens. Reagents that were used include formaldehyde [24], hydrogen peroxide [25], phosphorous [26], substituted ammonias [15], gases such as carbon monoxoide [15], hydrogen [20], nitrogen oxides [15] and acetylene [15]. Colloidal gold was also formed using a high voltage electrical discharge or flame source [27]. While there were many methods for the production of these colloids, these methods were very poorly understood and extremely sensitive to the procedure used. Producing colloids of

reproducible size was nearly impossible [23]. Frens' publication reported a method that was simple, effective and reproducible for the synthesis of colloidal gold. The method also used a reducing reagent that was cheap and easy to handle: sodium citrate.

All of the methods for the synthesis of colloidal gold are based on the premise of controlled reduction of an aqueous solution of tetrachloroauric acid, under varying conditions [23]. The formation of gold NPs is a delicate balance of two factors: The rate of nuclei formation and the rate of shell growth. Nuclei formation describes the formation of icosahedral nuclei formed at the beginning of the reaction, while shell growth is the growth of concentric layers around these icosahedral nuclei [23].

The use of very strong reductants (such as white phosphorous, tannic acid or sodium borohydride) results in a greater number of nuclei formed, which consumes the majority of tetrachloroauric acid and limits the amount available for shell growth: Smaller NPs are the result [23]. Conversely, using weak reducing agents will increase the size of the resultant NPs.

Sodium citrate is a much milder reducing agent than white phosphorous or tannic acid [23]. The citrate reduction method does offer some degree of synthetic control over the size of the resultant gold NPs. For example, adding excess citrate reagent increases nuclei condensation. The increased number of nuclei will then yield NPs that are smaller in size. Conversely, lowering the concentration of citrate reagent decreases the number of nuclei formed, and that results in an increase in NP size [2].

By using different reducing agents, or by varying the experimental conditions, gold NPs can be synthesized anywhere in the 0.8 to 100 nm size regime. However, as one increases the NP size above 20-30 nm, the colloids show increased particle eccentricity [23].

Colloids have a tendency to aggregate and form the thermodynamically stable bulk gold product [13]. Colloids are prevented from agglomeration through electrostatic or steric means. In electrostatic stabilization, an electrical double layer forms around the NP. First, the negatively charged (citrate) ions are attracted to the outer surface of the NPs. Then the positive (sodium) counter ions form a second layer, to complete the electrical double layer [28]. Colloids can be aggregated through the addition of electrolytes which compress the ionic double layer, which reduces electrostatic repulsion [23].

Steric stabilization can be accomplished by binding polymers, surfactant molecules, or other organic molecules to the NP surface [13]. These groups thus prevent NPs from approaching too close to each other, which is necessary for aggregation to occur. In the case of gold, organic thiol molecules have been extensively used to form what are called monolayer-protected clusters (MPCs) [29].

### 1.3.2 Optical Properties and Surface Plasmons

A reduction in particle size leads to vastly different physical and optical properties. Reducing the size of gold to the nanometer regime gives rise to a dramatic absorption

feature in the visible spectrum. This strong absorption is due to SP excitation, as described below.

Figure 1-2 shows the process behind SP oscillations. The incoming electric field induces a polarization in the conduction band with respect to the much-heavier ionic core of the spherical nanoparticle. The net charge difference occurs only at the nanoparticle boundaries (the surface), and this acts as a restoring force. This creates a dipolar oscillation of the electrons with the same phase, with a periodic oscillation of period T. When the frequency of the electromagnetic field becomes resonant with the coherent electron motion, a strong absorption is seen. This absorption is the origin of the observed colour in gold nanoparticles. The frequency and width of the SP absorption is strongly dependent upon the size and shape of the nanoparticles, and the medium surrounding it. Coincidentally, the noble metals (copper, silver and gold) exhibit a strong SP absorption which occurs in the visible region of the electromagnetic spectrum.

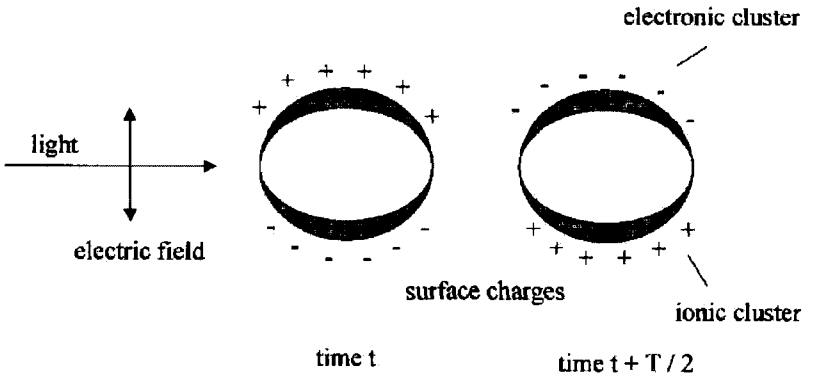


**Figure 1-2: Schematic demonstrating the excitation of the dipole surface plasmon oscillation. Figure reproduced from [13] with permission.**

The molar extinction coefficient for 20 nm gold nanoparticles is reported to be as high as $10^9$ $M^{-1}$ $cm^{-1}$ **[30]**, which is three to four orders of magnitude higher than that for the most strongly absorbing organic dye molecules.

In 1908, Mie was the first to explain the red colour of gold nanoparticles by solving Maxwell's equations for electromagnetic radiation interacting with small spheres that have the same dielectric properties as that of the bulk metal [18]. The solution to the electrodynamic calculation, with appropriate boundary conditions for spherical objects, leads to a series of multipolar oscillations for the extinction ($\sigma_{ext}$) and scattering ($\sigma_{sca}$) cross-sections of the nanoparticles, as a function of particle radius. The extinction and scattering cross-sections are related to the absorption cross-section by:

$$\sigma_{abs} = \sigma_{ext} - \sigma_{sca} \quad (1)$$

For larger particles (> 20 nm), higher-order modes become more dominant, causing the absorption band to red-shift along with increasing bandwidth. In essence, light can no longer completely polarize the sphere homogeneously, leading to excitation of higher-order modes (quadrupole, etc.).

For nanoparticles much smaller than the wavelength of the interacting light (< 20 nm), only the dipolar oscillation provides a significant contribution to the extinction cross-section. Mie's theory is thus reduced to the dipolar approximation, which is given by [21]:

$$\sigma_{ext}(\omega) = 9\frac{\omega}{c}\varepsilon_m^{3/2}V\frac{\varepsilon_2(\omega)}{[\varepsilon_1(\omega)+2\varepsilon_m]^2+\varepsilon_2(\omega)^2} \tag{2}$$

Where $V$ is the particle volume, $\omega$ is the angular frequency of the exciting light, $c$ is the speed of light, $\varepsilon_m$ is the dielectric of the surrounding medium and $\varepsilon(\omega) = \varepsilon_1(\omega) + i\varepsilon_2(\omega)$ is the complex dielectric function of the material itself.

The dielectric of the surrounding medium is assumed to be frequency independent, but the dielectric function for the material is a complex quantity that is dependent upon the frequency of the exciting light. Resonance occurs when the denominator of Equation (2) is at a minimum. That is to say, resonance occurs when $\varepsilon_1(\omega) = -2\varepsilon_m$.

### 1.3.3 Applications of Colloidal Gold

As a result of the Frens publication [22], colloidal gold was also examined as a labelling tool in the biological sciences [14]. Colloids were used to tackle problems involving endothelial transport, amoeba intracellular exchanges, lectins and antibodies. In particular, the labelling of antibodies using colloidal gold represented the first application as a specific cell marker in TEM [31]. Subsequently, colloidal gold was utilized as a probe in scanning electron microscopy [32], bright-field microscopy [33], dark-field microscopy [34] and fluorescent microscopy [35].

From a chemical and materials standpoint, gold colloids possess several attractive and important qualities. As a result of the decreasing dimensionality from the bulk to the nanoscale, the electronic properties undergo a substantial change due to the decrease in the density of states [13]. This size effect gives rise to exciting new optical and electronic properties [21].

Therefore, metallic nanoparticles stand to play a role in optical data storage and ultrafast communication [28, 36-38] because their optical properties can be easily tuned by changing particle size and shape, and they also show interesting NLO behaviour [13].

In addition, NPs could have potential uses in the field of catalysis because of their high surface-to-volume ratios [39-43]. To illustrate this point further, Link has noted that for a cube of iron with 1 cm edges, only $10^{-5}$% of the atoms are surface atoms [13]. Dividing that cube further into smaller cubes that are 10 nm on each edge yields 10% of the atoms

as surface atoms. Further decreasing to 1x1x1 nm cube means that ALL of the atoms are exposed [13]. The high degree of exposed atoms could dramatically increase catalytic throughput.

NPs also stand to play a role in the creation of spectroscopic substrates for the detection of analyte molecules using different spectroscopic techniques. This topic will be addressed further in Section 1.6.

In addition, the construction of two- and three-dimensional complex superstructures through self-assembly remains a goal of materials chemistry synthesis. The properties of such superstructures can be controlled through the nature of the constituent units and through the distances between particles or the overall morphology of the system. In that sense, gold nanoparticles are particularly useful because their surface and chemical reactivity can be easily tailored for specific applications [13]. As well, the size of the gold nanoparticles can be varied to produce a nanostructure of the desired morphology [4].

## 1.4 Spectroscopic Methods

Raman spectroscopy and Second Harmonic Generation will be utilized extensively in this work. The fundamentals of these two techniques are discussed in Sections 1.4.1 and 1.4.2.

### 1.4.1 Raman spectroscopy

When monochromatic radiation of energy $h\nu_0$ is incident upon a molecular system, the majority of such photons are elastically scattered and retain the same energy as the incident photon (Rayleigh scattering). Inelastic scattering can also occur, to the extent of one out of every $10^7$ incident photons. Inelastically scattered photons can possess less or more energy than the incident photon. This inelastic scattering is the underlying principle of the Raman effect. The interaction of a photon with a molecule and the possible outcomes are represented in Figure 1-3.

Since its first observation in 1928 [44], Raman spectroscopy has become an extremely valuable tool for the characterization of molecules in many research and industrial laboratories. When a photon is inelastically scattered by a molecule, vibrational energy ($h\nu_{vib}$) can be transferred to the molecule in a process known as Stokes scattering. The energy of the scattered photon will be $h(\nu_o - \nu_{vib})$, which is less than the incident radiation. Alternatively, the inelastically scattered photon can acquire vibrational energy from the molecule in anti-Stokes scattering: the energy of the scattered photon will then be $h(\nu_o + \nu_{vib})$. As mentioned earlier, the inelastic scattering is very weak and typically only one out of every $10^7$ incident photons will be scattered into either Stokes or anti-Stokes Raman emission.

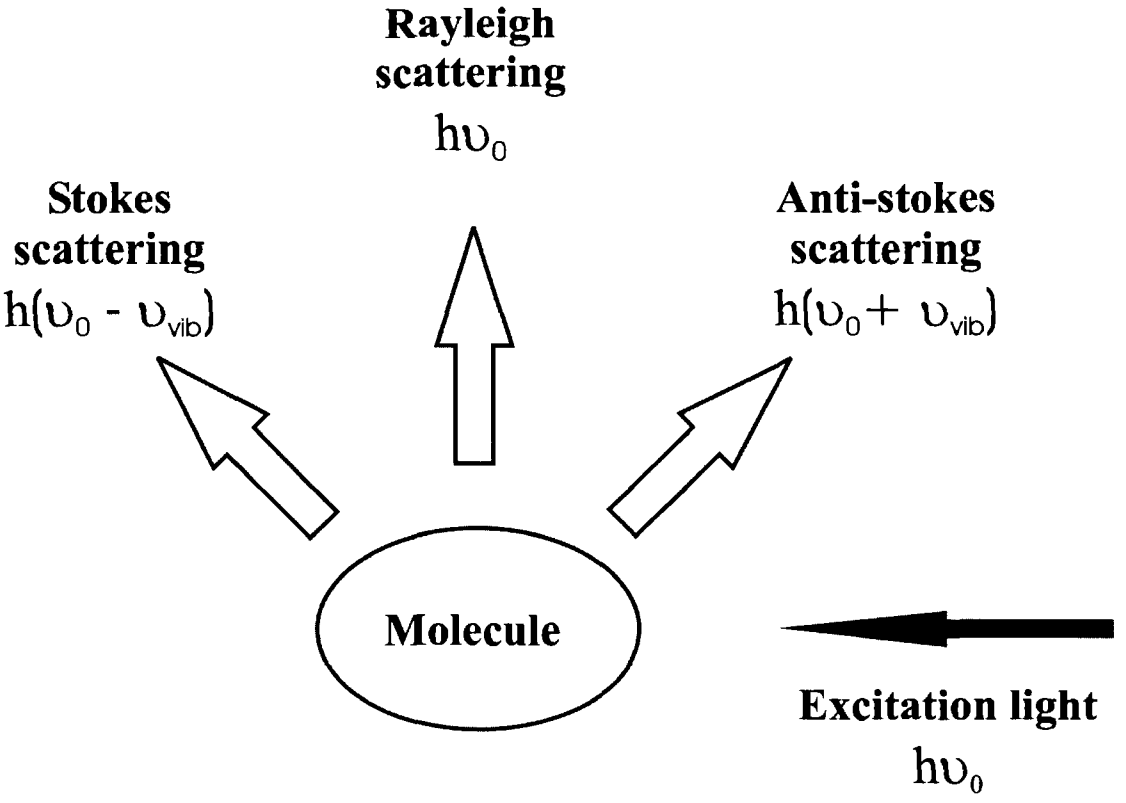


**Figure 1-3: Pictoral representation of three possible outcomes of a molecule interacting with a photon. The photon can be Rayleigh scattered, possessing the same energy as the incident photon. The system can scatter a photon with less energy, $h(\nu_0 - \nu_{vib})$, than the excitation source (Stokes scattering). Alternatively, a photon of greater energy, $h(\nu_0 + \nu_{vib})$, can be scattered (anti-Stokes scattering).**

The energy increase or decrease relative to the excitation photon is related to the vibrational energy spacing in the ground electronic state of the molecule: For Stokes scattering, there is a net energy increase of one vibrational quantum in the scattered photon, while in anti-Stokes scattering there is a net energy decrease of one vibrational quantum. Therefore, a Raman spectrum provides a direct measurement of the vibrational

energies of a molecule, and the corresponding Stokes and anti-Stokes lines will be equally spaced from the Rayleigh line (Figure 1-4).

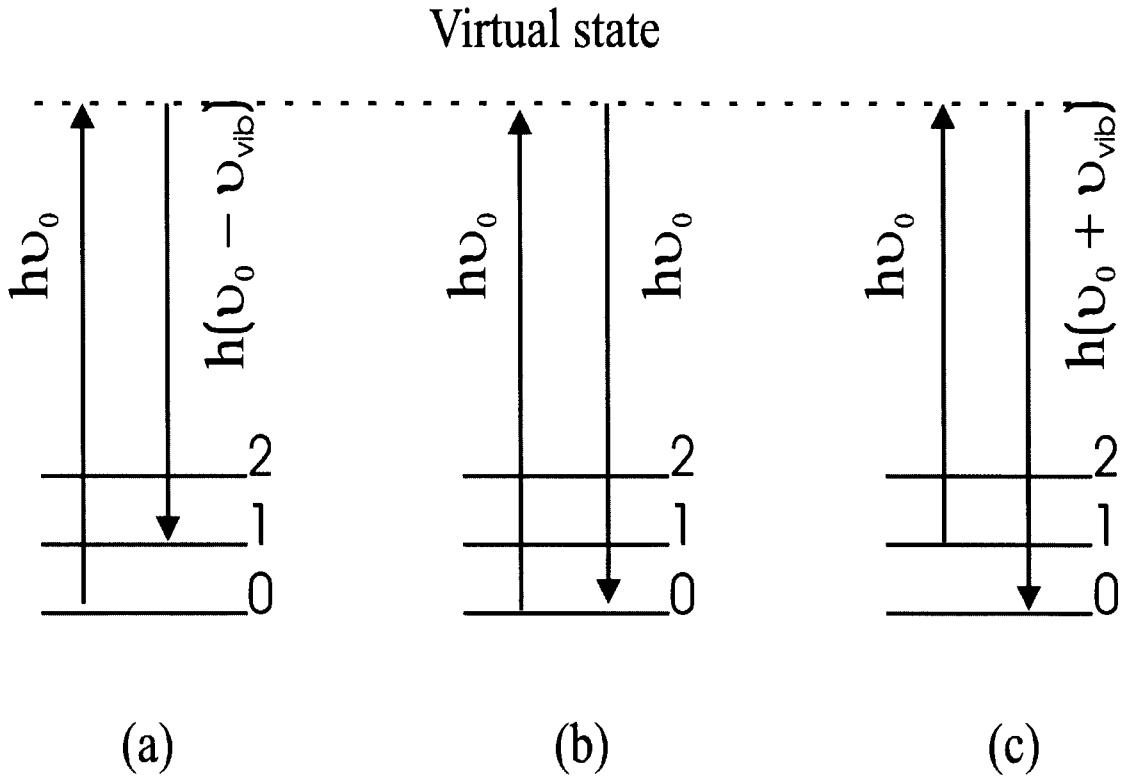


**Figure 1-4: Schematic showing the change in vibrational states for (a) Stokes, (b) Rayleigh and (c) anti-Stokes scattering.**

#### 1.4.1.1 Relative Intensity of the Raman bands

Of note is the fact that the anti-Stokes emission is typically less intense than the comparable Stokes transition. This is due to the fact that the anti-stokes transition relies upon molecules being vibrationally excited prior to the interaction with the incident light. In contrast, Stokes scattering involves molecules in the vibrational ground state prior to

the interaction. The vibrational ground state population is generally greater than the excited vibrational state population at room temperature. This population difference explains the difference in intensity between the Stokes and anti-Stokes bands.

#### 1.4.1.2 Classical derivation of the Raman Effect

Classically, the Raman effect is derived as follows. First of all, it is important to note that the electric field strength ($E$) of the excitation source (an electromagnetic wave) fluctuates with time ($t$), as given by:

$$E = E_0 \cos(2\pi \upsilon_0 t) \tag{3}$$

Where $E_0$ represents the amplitude and $\upsilon_0$ the frequency of the excitation source. When a molecule is irradiated by the field, a dipole $P$ is induced:

$$P = \alpha E \tag{4}$$

Where $\alpha$ is the polarizability of the molecule (The vector and tensor notation has been omitted for simplicity). Substituting Equation (3) into Equation (4) yields a time-dependence in the dipole moment:

$$P = \alpha E_0 \cos(2\pi \upsilon_0 t) \tag{5}$$

If the molecule vibrates with a frequency $v_{vib}$, the nuclear displacement ($q$) can be written as:

$$q = q_0 \cos(2\pi \upsilon_{vib} t) \tag{6}$$

Where $q_0$ is the equilibrium vibrational amplitude. For small vibrations, $\alpha$ is a linear function of $q$, and can be written as:

$$\alpha = \alpha_0 + \left(\frac{\partial \alpha}{\partial q}\right)_0 q \tag{7}$$

Where $\alpha_0$ is the polarizability at the equilibrium position and $\left(\frac{\partial \alpha}{\partial q}\right)_0$ is the rate of change of polarizability ($\alpha$) with respect to a change in the vibration of the molecule ($q$), at the equilibrium position.

Combining Equations (5), (6) and (7) yields:

$$\begin{aligned} P &= \alpha E_0 \cos(2\pi \upsilon_0 t) \\ &= \alpha_0 E_0 \cos(2\pi \upsilon_0 t) + \left(\frac{\partial \alpha}{\partial q}\right)_0 q E_0 \cos(2\pi \upsilon_0 t) \\ &= \alpha_0 E_0 \cos(2\pi \upsilon_0 t) + \left(\frac{\partial \alpha}{\partial q}\right)_0 q_0 E_0 \cos(2\pi \upsilon_0 t)\cos(2\pi \upsilon_{vib} t) \\ &= \alpha_0 E_0 \cos(2\pi \upsilon_0 t) + \left(\frac{1}{2}\right)\left(\frac{\partial \alpha}{\partial q}\right)_0 q_0 E_0 [\cos\{2\pi(\upsilon_0 - \upsilon_{vib})\} + \cos\{2\pi(\upsilon_0 + \upsilon_{vib})\}] \end{aligned} \tag{8}$$

Where the following trigonometric identity was used in the derivation of Equation (8):

$$\cos A \cos B = \frac{1}{2}\{\cos(A+B)+\cos(A-B)\} \tag{9}$$

In regards to Equation (8), it should be noted that the first term represents an oscillating dipole that radiates light of frequency $v_o$, which corresponds to Rayleigh scattering. The second term contains the Raman scattering of frequency $(\upsilon_0 - \upsilon_{vib})$ (Stokes) and $(\upsilon_0 + \upsilon_{vib})$ (anti-Stokes).

The intensity of a Raman transition is described by:

$$I_{Raman} = k \cdot \upsilon_0^4 \cdot I \cdot \left| \sum_{\sigma\rho} \alpha^{\sigma\rho} \right|^2 \tag{10}$$

Where the term $k$ is comprised of various natural constants such as $\pi$ and the speed of light, $v_0$ is the frequency of the incident radiation, $I$ is the intensity of the incident radiation, and the last term represents the Raman polarizability tensor [45, 46].

#### 1.4.1.3 Raman selections rules

While IR and Raman spectroscopy are similar because they both yield information on the vibrational frequencies of molecules, the nature of the selection rules for both are

markedly different. For a transition to be Raman active, it can be seen from equation (8), that the quantity $\left(\frac{\partial \alpha}{\partial q}\right)_0$ cannot equal zero. That is to say, the rate of change of polarizability ($\alpha$) with the vibration must be non-zero.

In IR spectroscopy, a transition will be active only when there is a change in the dipole moment with the vibrational coordinate. For example, the symmetric stretch of carbon dioxide is not IR active because no change in dipole moment occurs. In Raman spectroscopy, a symmetric stretch results in a change in the polarizability ellipsoid for the molecule and is therefore Raman active [45, 46]. From group theory, it can be shown that if a molecule has a centre of symmetry, vibrations which are Raman-active will be inactive in IR spectroscopy, and vice versa [45, 46].

### 1.4.2 Second Harmonic Generation

The phenomenon of optical SHG was first observed in 1961 when Franken et al. measured the evolution of 347.1 nm laser light when a ruby laser of 694.2 nm was passed through a quartz crystal [47]. While harmonic generation of electromagnetic waves had been observed before at low frequencies, this represented the first observation of optical waves undergoing SHG. This phenomenon had not been observed previously because field strengths of up to 1 kV / cm are required: Powers of this level can only be generated through the use of lasers, which had only been recently invented at the time of this discovery [48]. A demonstration of the second harmonic (SH) process is shown in Figure 1-5.

In SHG, a beam of monochromatic electromagnetic energy of frequency $\omega$ impinges on an asymmetric medium (such as an asymmetric crystal or a surface). The lack of symmetry at the interface can allow for the generation of light at twice the frequency of the incident light ($2\omega$ - the second harmonic).

The key to surface SHG is that, within the dipole approximation, SHG is forbidden in any bulk material that exhibits inversion symmetry, such as any face-centred cubic (fcc) crystal. Most metals possess such symmetry and therefore no signal is produced from the bulk of the material. At the surface the inversion symmetry is broken and SHG can be generated at the metal-dielectric interface. SHG from metals is therefore an inherently surface-specific spectroscopic technique that probes only the topmost 3-5 layers of the surface under investigation.

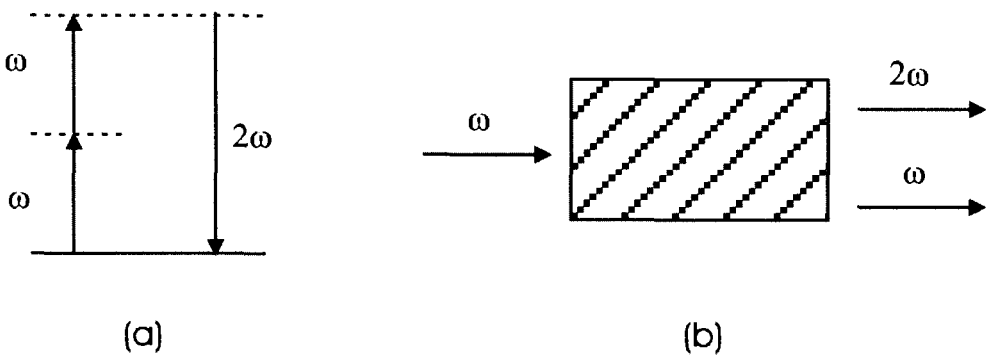


**Figure 1-5: Schematic of the SHG process. (a) Two photons of frequency ω combine, and a photon of twice the frequency ($2\omega$) is emitted. (b) Photons of frequency ω pass through a material with a large second-order susceptibility. The large majority of photons retain the same frequency, but a small number combine and are emitted at the second harmonic frequency ($2\omega$) [49].**

The theory behind SHG is detailed in many excellent books on NLO [49-51], and only a cursory presentation is discussed here. At high optical intensities, the material polarization response becomes nonlinear with respect to input power, as represented by:

$$P \propto \left(\chi^{(1)}E + \chi^{(2)}E^2 + \chi^{(3)}E^3 + \ldots\right) \tag{11}$$

Where $P$ represents the material polarization, and $\chi^{(n)}$ represent the first, second, third, etc. susceptibility. When $n > 1$, this is referred to as the non-linear susceptibility. In general, the non-linear susceptibilities are small, which makes observations of the SH signal onerous.

For SHG, the intensity of the SH signal produced is proportional to the square of the second-order susceptibility:

$$I(2\omega) \propto \left[\chi^{(2)}\right]^2 I^2(\omega) \tag{12}$$

Note that $\chi^{(2)}$ is a third-rank tensor. The symmetry of the system under examination will dictate which of the elements are nonzero.

## 1.5 Enhanced Spectroscopy

The signals obtained from Raman spectroscopy and SHG are extremely minute. The limited signal strength could thus limit the applicability of these techniques to specialized situations only. Enhancements of the signals is possible through the excitation of surface plasmons to yield surface enhanced Raman scatterings (SERS) or surface enhanced second harmonic generation (SE-SHG). These enhancements yield exciting potential new uses for these techniques.

### 1.5.1 Surface Enhanced Raman Scattering (SERS)

Surface enhanced Raman scattering (SERS) is one of the most sensitive methods for the detection of adsorbate molecules on nanostructured metal surfaces [52-54]. Signal enhancements on the order of $10^4$ - $10^6$ are routinely observed, and in some systems

enhancements of up to $10^{14}$ can be obtained [55]. Such enhancement makes this technique readily applicable to the study of submonolayer quantities of analyte.

The SERS effect was first observed in 1974 by Fleischman et al. for pyridine adsorbed on an electrochemically roughened silver electrode [56]. However, the anomalous Raman signals were attributed to a large increase in the surface area through the oxidation-reduction cycling of the electrode. In 1977, Van Duyne and Jeanmaire [57] and, at nearly the same time, Albrecht and Creighton [58], were the first to attribute this phenomenon to an actual anomalous increase in the Raman signal, and not to an increase in the surface area.

Typically, the SERS effect occurs when a species is adsorbed onto a rough surface of a free electron metal such as Au, Ag, or Cu [53]. Excitation with visible light (usually red or green) and near IR is generally used [54].

#### 1.5.1.1 The Nature of the SERS

The origin of SERS stems from two different mechanisms. In the first, called the electromagnetic mechanism (EM), the excitation and localization of surface plasmons within the metallic nanostructure enhance the local electromagnetic field. In the second, known as the chemical mechanism, an enhanced polarizability of the adsorbate associated with charge transfer from the metal also causes an enhancement in the Raman signal.

When chemical enhancement occurs, the molecular polarizability ($\alpha$) increases due to the formation of a charge-transfer (CT) metal-molecule complex. This increase in $\alpha$ causes an increase in the induced molecular dipole and hence an increased Raman signal (See Equation 4) [59, 60].

In the EM mechanism, the local electric field ($E_{local}$) experienced by the adsorbed molecule is increased through the excitation of the surface plasmons of the supporting metal. The increase in $E_{local}$ is tantamount to an increase in laser intensity in Equation (10), because laser intensity (I) is proportional to the square of the electric field.

Much debate has occurred in the literature as to which of the two mechanisms is dominant in the SERS effect [53]. Although it is now accepted that the EM mechanism is generally dominant, researchers agree that both mechanisms contribute to a certain degree in every system [52, 54, 60]. The design of the experiment itself can also influence to a great extent the relative contributions from each of these enhancements.

The nature of the chemical and electromagnetic contributions will be examined in more detail in Sections 1.5.1.2 and 1.5.1.3.

#### 1.5.1.2 Electromagnetic (EM) Enhancement

The EM enhancement arises from an increase in the local electromagnetic field produced at the surface of the metal. This occurs when the incident light couples with the electron

oscillations at the metallic surface. These coherent electron oscillations at the metal surface are known as surface plasmons (SP).

To illustrate this concept, one can consider the example of a metal sphere in an external electric field. Excitation of the surface plasmons of the particle greatly increases the local field experienced by a molecule absorbed on the particle [54, 61]. This is accomplished when the particle localizes the plane wave of light into a dipole field which is centered in the sphere, and then decays outwards from the surface in all directions [54]. The particle will not only enhance the electric field from the incident laser, it will also enhance the Raman scattered field from the molecule. In this sense, the particle acts as an antenna which amplifies the scattered light intensity [61, 62]. This process is demonstrated in Figure 1-6, for a rough metal surface. This system is analogous to having many spherical particles deposited on the surface: certain rough spots will be of sufficient geometry and will act as polarizing spheres that enhance the Raman signal.

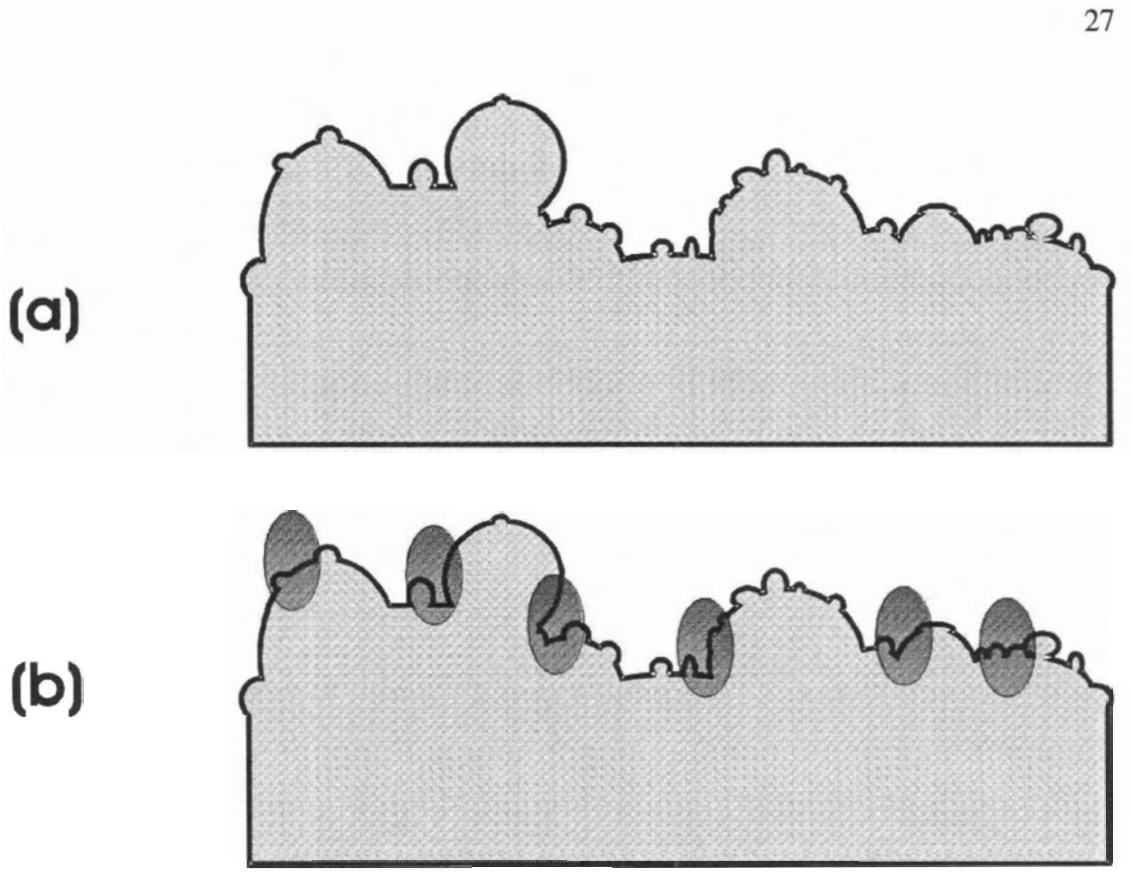


**Figure 1-6: Demonstration of the "hot spots" when a rough surface is irradiated with electromagnetic radiation. (a) A rough metal surface (b) Following irradiation by an electromagnetic field, "hot spots" on the surface are generated via SP excitation. The electromagnetic field at the hotspots is greatly amplified.**

To a first approximation (i.e.: small Stokes shift), the electromagnetic enhancement factor is dependent upon the fourth power of the ratio of the total electric field at the molecule location and the incident excitation field:

$$^{em}G_{SERS} = \left|\frac{E_{Local}}{E_{inc}}\right|^4 \qquad (13)$$

On a smooth surface, the SP are confined and cannot be exited by an incident photon due to a momentum mismatch [63]. On a rough or corrugated surface, these surface protrusions provide additional momentum to the photon, which allows for SP excitation.

When the diameter of the bumps on the surface are smaller than the wavelength of light, the incoming electric field polarizes the sphere and induces a dipolar response (for a polarizable sphere). The calculated local electric field ($E_{local}$) is proportional to:

$$E_{local} \propto g = \frac{(\varepsilon_1(\omega) - \varepsilon_2)}{(\varepsilon_1(\omega) + 2\varepsilon_2)} \tag{14}$$

Where $\varepsilon_2$ is the optical dielectric constant for the surrounding medium and $\varepsilon_1(\omega)$ is the dielectric function of the metal. This complex function is given by:

$$\varepsilon_1(\omega) = \mathrm{Re}|\varepsilon_1(\omega)| + i\,\mathrm{Im}|\varepsilon_1(\omega)| \tag{15}$$

From Equations (14) and (15), $E_{local}$ will be maximized when the divisor of (14) is minimized. That is to say, minimization will occur when the real component of the complex dielectric function is equal to $-2\varepsilon_2$ (and $Im(\varepsilon_1(\omega))$ is small). It is for this reason that SERS has only been observed on specific metals (Cu, Ag, Au) using visible excitation: The dielectric functions of these metals are the only ones that allow for SP excitation in the visible region [64].

Calculations have also shown that there is a strong dependence of the enhancement factor on the morphology of the enhancing surface feature [55]. In particular, strong enhancement of the electromagnetic field for sharp features and large curvature regions are predicted theoretically [55]. Coupling of the incident photons and the surface plasmons concentrates the electromagnetic field in certain regions of the surface, producing a very large field gradient when the molecule is positioned at these particular locations. This phenomenon is described as the lightning rod or antenna effect [65].

Electromagnetic enhancement factors of $10^6 - 10^7$ are typical for most experiments [55].

#### 1.5.1.3 Chemical Enhancement – The CT Mechanism

Previous research observed that different molecules (with similar polarizability) deposited onto the same surface yielded very different enhancement factors [60]. This could not be fully explained through the EM mechanism. As a result, the charge transfer (CT) mechanism has been proposed.

In CT, the mechanism arises from the specific interactions of a molecule with the metal through electronic coupling (Figure 1-7). In essence, a charge-transfer (CT) complex is formed between an adsorbed molecule and the atomic scale roughness of the metal surface (adatoms). As a result of complex formation, the frontier molecular orbitals of the adsorbed molecule become similar in energy to the metal's Fermi level. The difference in energy between the frontier molecular orbitals and the Fermi level is close

to that of the incident light. Such an enhancement is similar to that observed for resonance Raman processes.

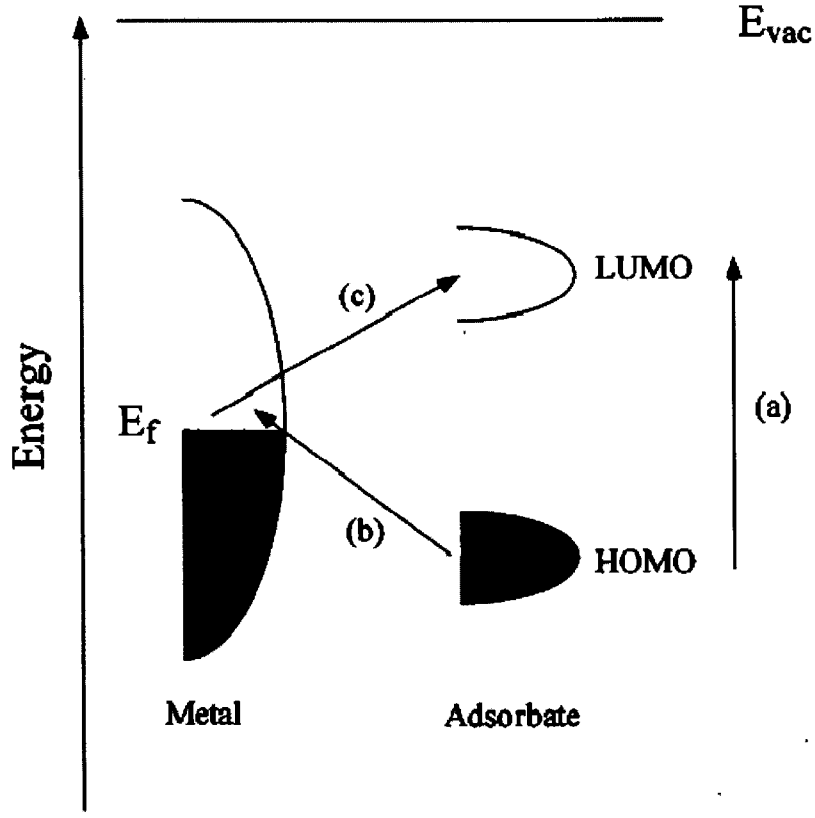


**Figure 1-7: Demonstration of the CT mechanism. (a-c) correspond to different charge transfer excitations. For example, (c) corresponds to a transfer of an electron from the metal to the lowest unoccupied molecular orbital of the adsorbate. Figure originally from [54] – Reproduced by permission of The Royal Society of Chemistry.**

In general, the magnitude of the chemical enhancement is much smaller than that observed for the electromagnetic enhancement. Estimated enhancement values of 10-100 are typical for this mechanism [55].

### 1.5.2 Surface enhanced SHG

The enhancement mechanism behind SHG from nanostructured surfaces has some similarities to that of EM-SERS. In SHG, the surface plasmons can also enhance the local EM fields. This process is characteristically dependent upon the surface roughness when the microscopic surface structures are small in comparison to the wavelength $\lambda$ of the excitation electromagnetic wave. The coupling is particularly efficient for spherical or ellipsoidal clusters that have diameters smaller than $\lambda$, and results in a strong electromagnetic field enhancement of the nonlinear optical response.

The literature on the SHG of colloids is rather sparse. The main contributions in this area have been produced by Antoine *et al.* In their 1992 study, the SH response of colloidal gold embedded in an aluminum matrix was examined [66]. The SH response was monitored as a function of the energy of the fundamental incident beam. It was shown that the spectrum exhibits a narrow resonance band near 520 nm which is due to the coupling of the second harmonic field with the surface plasmons of the particles.

In 1999, the same group aggregated colloidal gold using pyridine and monitored the SH response. Initially, a strong enhancement of the SH signal was observed upon the addition of pyridine. At larger pyridine concentrations, the SH signal levelled off owing

to the formation of larger aggregate structures [67]. A further paper from the same research group showed that the hyperpolarizability ($\beta_{colloid}$), and consequently the SH response, from colloids is intrinsically dependent upon the size of the colloids [68]. Thus, this would allow for a separate and distinct method for the determination of colloid size. Note that the hyperpolarizability is related to the second-order susceptibility by:

$$\chi^{(2)} \propto N\langle\beta\rangle \tag{16}$$

Where N is the number of molecules being probed.

Further work has also been performed in the study of the SH of colloidal gold. In the work of Clark *et al.* [69], gold nanoparticles were combined with a fluorescent dye. Both of these species provide a weak SH signal, and it was shown that the combination of both produce a significantly enhanced SH signal, relative to either component [69].

Srinivasan *et al.* produced work involving the deposition of gold nanoparticles onto a H-Si(111) surface [70]. In their work, the SH response was noted to have a definite dependence on the size of the aggregate structure. With initial nanoparticle deposition, there is a dramatic increase in the SH response. The response reaches a maximum for lateral aggregate structures on the order of 90 – 100 nm in diameter. Structures larger than this critical dimension result in suppression of the SH response.

Metal-island films, which consist of a two-dimensional arrangements of metal nanoparticles, were expected to yield a strong SH enhancement [71]. However, these structures have not lived up to their expected promise in terms of SH enhancement. Experimental SH factors of up to 10 have been obtained, which is much lower than expected. One possible reason for the surprisingly weak enhancement could be due to the altered symmetry induced by the particle structure at the surface: It has been shown that granular films possess a high degree of centrosymmetry. As a result, the bulk second-order susceptibility will be inhibited [72].

To counteract this, Tuovinen *et al.* produced a nanoscopic array of noncentrosymmetric nanoparticles using electron-beam lithography [73]. They also showed that the orientation of these L-shaped nanoparticles has a dramatic effect on the SH response – differences of up to 60% were observed experimentally.

## 1.6 Development of spectroscopic substrates

Surface-enhanced Raman scattering (SERS) has attracted the attention of analytical chemists because of its simultaneous ability to yield structural and quantitative information about molecular species. However, SERS has not lived up to its potential because of a lack of suitable reproducible substrates for sample analysis.

In a typical experiment, the analyte molecule will be deposited onto the substrate surface, with the net result being an enhancement of the Raman signal through the SERS mechanism, to yield a signal that can be easily detected and quantified. For analytical

applications, the requirements of an ideal SERS substrate are numerous, but the most important include low cost, highly-enhancing, rugged and reproducible [53].

Colloidal gold and silver, and in particular their aggregates, were first observed to be highly SERS enhancing [8, 74-76]. Structures containing aggregates in the 100-1000nm size regime were particularly useful for trace analytical applications [55, 74]. The aggregate structures were prepared by the "Activation" (or aggregation) of the colloidal solution using a NaCl solution, in the presence of a small amount of analyte. While this method does provide a remarkable enhancement of the Raman signal, it does not provide a reproducible aggregate structure. As a consequence, obtaining reproducible SERS signals becomes troublesome.

Many different surfaces, geometries and compositions have been examined for their ability to provide SERS-active surfaces. In general, these substrates can be separated into two distinct categories: Substrates produced from physical means (vapour deposition), or those prepared in the solution phase (self-assembly). Each of these categories will be dealt with separately, and the highlights of research in each area will be presented.

### 1.6.1 Physical methods for the preparation of substrates

SERS-active substrates can be prepared by the vapour deposition of metals (Au, Ag and Cu) onto supporting surfaces such as glass or $SiO_2$/Si [77, 78]. The temperature of the substrates, the film thickness and rate of deposition have all been modulated in order to provide a substrate with increased enhancement [79-81]. Metals have also been

evaporated on rough surfaces such as alumina-covered glass, $TiO_2$-coated glass and filter paper [82].

An alternative preparation strategy for SERS substrates is one pioneered by the van Duyne research group, which provides a method for creating controllable, predictable and reproducible SERS substrates [77]. In nanosphere lithography (NSL), polystyrene (PS) nanoparticles (typically hundreds of nanometers in diameter) are spin coated onto a glass surface to form a two-dimensional hexagonal array. The PS beads act as a "mask" for the layer of silver that is then vapour deposited over top of the assembly. Silver deposits at the interstices of the beads, after which the beads are removed by sonication. What remains behind is a periodic particle array (PPA) of silver islands dispersed across the glass surface (Figure 1-8). This PPA can be tuned by varying the diameter of the PS beads, the angle of vapour deposition and the amount of silver deposited to give structures of different geometry or separation. This will allow for a tunability of the surface roughness to correspond to a particular excitation wavelength, and thus to yield maximum SERS enhancement.

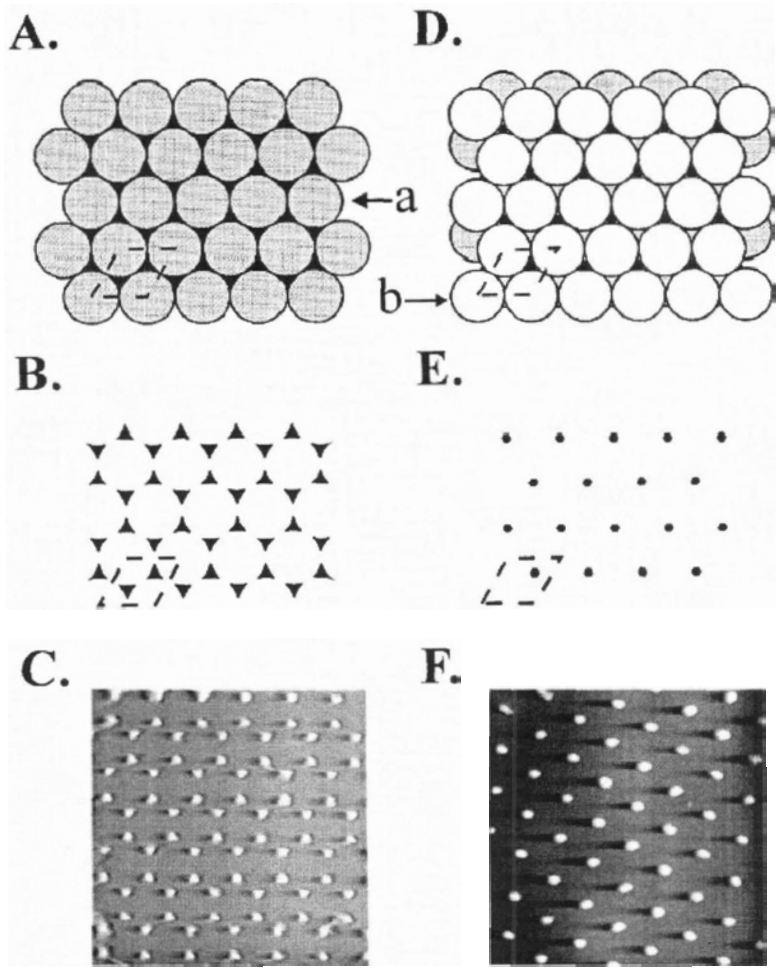


**Figure 1-8: Demonstration of the NSL process. (A) Deposition of PS spheres onto a glass surface. The dotted line indicates the unit cell. (a) is the first layer nanosphere (B) Deposition of silver over top of the PS spheres, and subsequent removal of the PS spheres leaving silver islands that form a PPA. There are two particles per unit cell. (C) AFM image of the PPA. (D) A double layer of PS spheres deposited. (b) is a second layer nanosphere. (E) Deposition of silver and removal of PS spheres to form a PPA. (F) AFM image of the PPA. Figure reproduced from [77] with permission. Copyright 1995 AVS, The Science & Technology Society.**

The creation of nanostructured arrays can also be accomplished through the use of electron-beam lithography. Gold or silver is vapour deposited onto a $SiO_2$/Si wafers, and then an electron beam is used to create arrays with patterns of features ca. 100 nm in size [73]. Focussed ion beams (FIB) have also been used to generate nanohole arrays which are highly Raman enhancing [83].

"Sandwich" structures have been prepared by Zhang *et al.* and characterized based on their SERS enhancement [78]. This method involved the assembly of functionalized azobenzene thiols onto surfaces that consisted of gold, silver foil or etched silver foil. What made this investigation particularly interesting was that a further layer of silver was vapour deposited on top of the azobenzene to give a sandwich-like architecture. Stretches from the azobenzene were particularly enhanced when protrusions of 100 nm were created on the surface on the substrate. Features larger or smaller than this size showed a decrease in SERS signal. In addition, Zhang also showed that the enhancement factor decreases exponentially with increasing distance of the azobenzene group from the underlying substrate or the overlying silver layer. This is a critical reminder that this enhancement is a surface effect, and decays rapidly away from the surface.

### 1.6.2 Solution-phase assembly of substrates

Solution-based assembly strategies for the development of SERS-active substrates has been a focal point of research in the past several years [5-8, 10, 84-86]. In particular, the assembly of gold nanoparticles on to a glass surface has been heavily studied. Cotton *et*

*al.* initially demonstrated the utility of depositing colloidal gold on derivatized glass slides as a substrate in surface-enhanced spectroscopy [87]. Another initial paper in this field was produced by the Natan group and similarly involved the deposition of gold nanoparticles onto a derivatized glass surface [6]. These substrates were characterized for their suitability and were found to be SERS-active. Many papers were produced by this research group characterizing these new substrates, and the underlying theory behind them [2-4, 84].

Subsequently Bright *et al.* published an article in which a layer of silver was chemically deposited over top of a colloid monolayer [5]. It was believed that the combination of silver (a strong SERS-active metal) and the underlying morphology of the surface would yield a highly enhanced SERS signal. While a large signal enhancement was observed, the electrochemical deposition process must be precisely tuned to yield optimum results.

Another paper from Bright *et al.* document the deposition of Ag colloids onto a derivatized surface to yield a two-dimensional Ag colloid structure [88]. However, it was noted that these substrates did not provide enhancement similar to what has been observed from roughened bulk Ag metal.

An extension of Natan's work involved the construction of multilayer substrates consisting of alternative layers of colloid monolayers and a bifunctional linker molecule [89]. However, a thorough SERS investigation was not performed. Instead, it was suggested that this structure could be an interesting SERS substrate because it could offer

roughness tunability based on the number of colloid layers deposited [89]. It is this paper that provides the motivation for this thesis.

One final extrapolation of Natan's work was performed by Mulvaney *et al.* involved the construction of three-layer substrates consisting of a combination of nanoparticle assembly and evaporated thin films [90]. A layer of colloidal gold was deposited onto a glass surface with subsequent chemical deposition of Ag onto this surface, and then vapour deposition of a layer of Ag. The well-defined surface morphology of the Au colloid layer and the optical properties of the Ag layers were expected to yield enhanced SERS signals. Enhancement factors on the order of $10^4$ and picogram detection limits were observed. Note that this paper by Mulvaney is similar to that of Zhang [78] presented in Section 1.6.1, except the underlying layer here is a monolayer of colloids, instead of gold or silver foil.

# Chapter Two: Experimental

## 2.1 Chemicals

Unless otherwise noted, ACS reagent grade chemicals were used. $HAuCl_4$, sodium citrate dihydrate, ascorbic acid, cetyltrimethylammonium bromide (CTAB), poly(sodium 4-styrenesulfonate) (PSS – Average molecular weight 70,000), poly(allylamine hydrochloride) (PAH), propanedithiol (PDT), poly(diallyldimethylammonium chloride) (PDDA, 200,000-350,000 molecular weight, 20 weight percent in water) and a colloidal gold solution (10 nm mean diameter) were obtained from Sigma-Aldrich.

$AgNO_3$, NaCl and $NaBH_4$ were obtained from ACP. 3-mercaptopropyltrimethoxy silane (MPTMS, 97+%) was obtained from Fluka. $H_2O_2$ was obtained from EM Science. Methanol (MeOH) was obtained from Caledon Laboratories Ltd. Oxazine-720 was obtained from Lambdachrome. HCl, $H_2SO_4$, $HNO_3$ and $NH_4OH$ were obtained from Anachemia.

Unless otherwise indicated, all water used was obtained from a Barnstead NANOpure Diamond water purification system. The ultrapure water had a resistivity greater than 18.2 MΩ·cm.

The chemical structure of some of the reagents is presented in Figure 2-1.

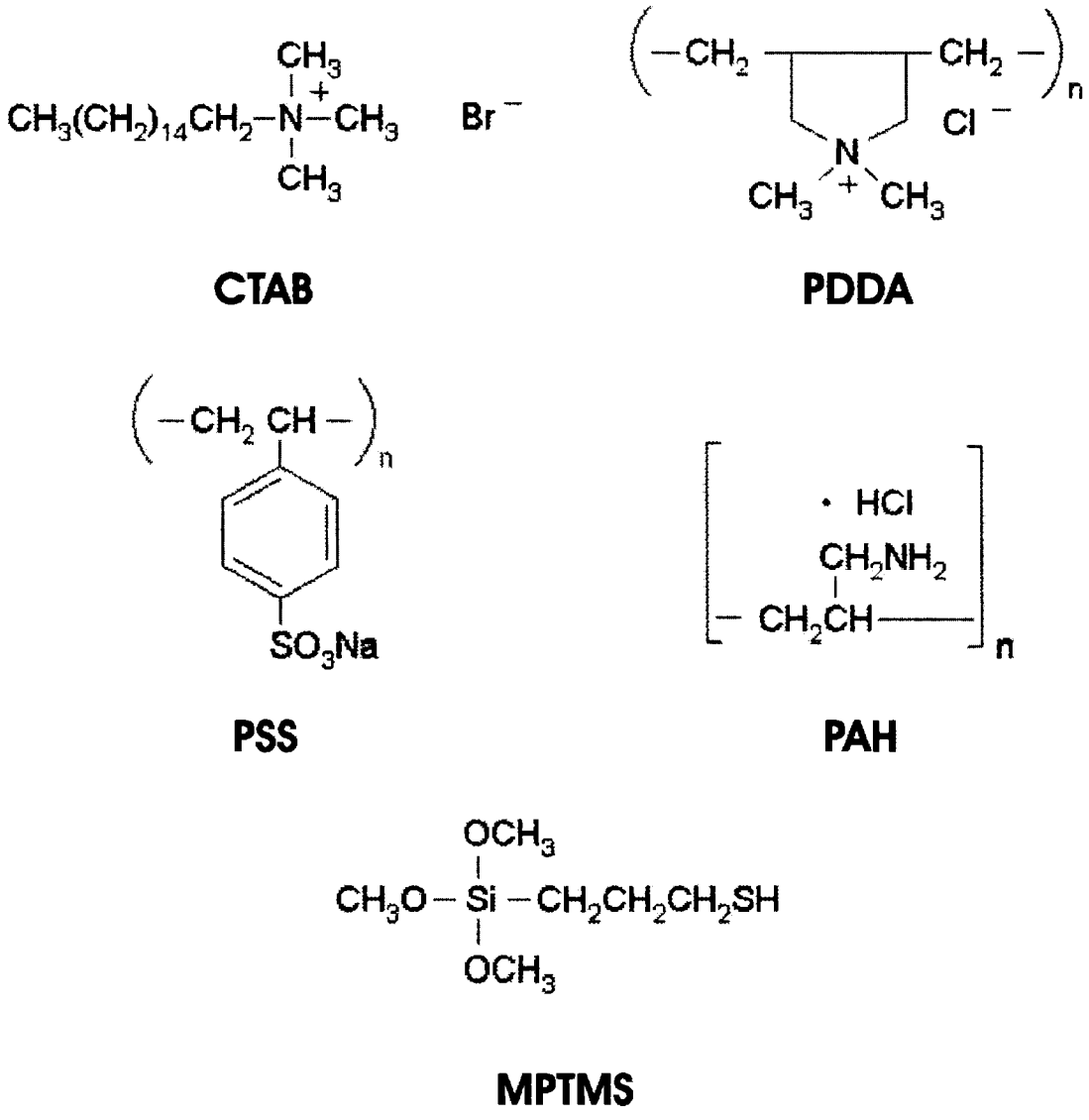


**Figure 2-1: Chemical structures of some of the reagents encountered in this work.**

## 2.2 Colloidal Gold Preparation

The use of clean glassware is critically important for the successful synthesis of gold NPs. All glassware used here followed a rigorous cleaning procedure, which involved

soaking in a hot (ca. 100°C) $H_2SO_4$ bath overnight. The glass was subsequently rinsed with deionized water and heated at 110°C in an oven to dry. To remove any remaining impurities, the glassware was immersed in a bath of Aqua Regia solution (3:1 HCl / $HNO_3$) for 20 minutes and rinsed with deionized $H_2O$. The glassware was then heated at 110°C to remove residual $H_2O$.

The standard procedure for the synthesis of colloidal gold is a method published by Frens [22]. In this work, a slight modification to the Frens procedure published by Grabar et al. was used [6]. 500 mL of a 1 mM solution of $HAuCl_4$ was brought to a rolling boil with stirring, and then 50 mL of 38.8 mM sodium citrate was added. The solution colour instantly changed from yellow to colourless. Heating and stirring was continued for 10 minutes, which resulted in the solution changing to a wine-red colour. After this time period, heating was discontinued and stirring was allowed to continue for another 15 minutes to complete the reaction.

To improve the longevity of the prepared colloidal gold solutions, they were stored in an amber bottle at 4°C. Colloid solutions were observed to be stable for up to 1 year without appreciable aggregation or bacterial growth.

### 2.2.1 Colloid Aggregation

Aggregation of the colloidal gold solution was accomplished through the addition of 100 μL of 1 M NaCl to a cuvette containing 1 mL of the colloidal gold solution. The reaction

was allowed to take place for 5 minutes, and then the UV-Vis spectrum was obtained. Acquisition settings for the UV-Vis spectrum are as described in 2.4.1.

## 2.3 Gold Nanorod Preparation

Gold nanorods were prepared using the seed-mediated method published by Nikoobakht and El-Sayed [91]. The synthesis is a two-step process in which a seed solution is prepared, and then used to mediate growth when added to a growth solution.

The seed solution was created by adding 5 mL of 0.2 M CTAB to 5.0 mL of 500 μM $HAuCl_4$. This solution was stirred and then 0.60 mL of 1.0 mM $NaBH_4$ was added. This results in a brownish-yellow solution. Stirring of this solution continued for 2 minutes after the addition, and was then stored at 25°C in a constant-temperature water bath.

While the seed solution was being incubated in the constant-temperature water bath, the growth solution was prepared through the addition of 5 mL of 0.2 M CTAB to 0.25 mL of 4.0 mM $AgNO_3$ solution at 25°C. 5.0 mL of 1.0 mM $HAuCl_4$ was added to this solution, and the mixture was gently stirred. Subsequently, 70 μL of 78.8 mM ascorbic acid was added. The addition of the reducing agent (ascorbic acid) results in a change in solution colour from milky-yellow to colourless. The temperature of the growth solution was then increased to 30°C in a constant-temperature water bath.

The gold nanorods were prepared by adding 12 μL of the seed solution to the growth solution. While it is noted in the literature method that 10-20 min is required for a

change in solution colour [91], it has been observed experimentally that in fact it can take up to 45 minutes for this process to occur.

Crystallization of the excess surfactant is noted in the subsequent hours and days after synthesis. Therefore, it is important to remove the excess surfactant immediately after synthesis. This is accomplished by centrifuging the nanorod solution at 9000 rpm for 15 minutes. As a result of the centripetal force, the nanorods will end up in the bottom of the centrifuge tube. The supernatant, which contains the surfactant, is removed and the volume replaced with deionized water. This process is repeated one more time, and after completion, no crystallization of the surfactant was noted.

Care must be taken with the centrifugation procedure, because a critical amount of surfactant is required to prevent aggregation of the nanorods [92]. It has been observed here that centrifuging more than 3 times will result in irreversible aggregation of the nanorods.

Nanorod solutions were stored in an amber bottle at 4°C, and were used within four months of synthesis.

## 2.4 Colloid characterization

### 2.4.1 UV-Vis Characterization

UV-Vis characterization of the colloidal solutions was performed using a Cary 50 UV-Vis instrument. Operation of the Cary 50 was performed using Cary WINUV software. The scan range was 900-400 nm with a scan rate of 600 nm/min and 2 nm resolution. Disposable cuvette cells were used for all measurements. A deionized water spectrum, obtained under the same experimental conditions as other measurements, was used as a background.

### 2.4.2 TEM Characterization

To characterize the shape, size, and size distribution of the prepared colloidal sol, a Hitachi H-7000 transmission electron microscope (TEM) was employed. 10 μL of the colloidal solution was placed onto a formvar coated-TEM grid, and the water allowed to evaporate. This resulted in the deposition of the colloids onto the TEM grid. The grid was then placed into the TEM. All TEM images were obtained at 75 kV magnification, and at least 100 individual particles were measured.

The TEM instrument was not calibrated to give accurate size measurements at this specific magnification level. Therefore, some form of calibration was required. This was accomplished by obtaining a TEM image of a commercially-available colloidal solution (of known size) in a manner similar to that described above.

Images were obtained as photographic negatives and were transferred to a digital format. The negatives were scanned using a Polaroid Sprintscan 4" x 5" film scanner. Scanner settings varied for each image to provide optical image quality, but in general a lightness setting of 10, a contrast of 0 and a sharpness of 100 were employed. Images were scanned at a 300 dpi resolution. The resultant image was saved in the Joint Photographic Experts Group (JPEG) format. Image manipulation and measurements was performed using the Adobe Photoshop software package. The experimentally-determined scale bar was added to the images using Adobe Photoshop.

## 2.5 Colloidal-based Nanostructure Synthesis

### 2.5.1 Surface Derivatization

3" x 1" glass microscope slides (Fisher) were cut into approximately 1" x 1" squares using a glass cutter. Slides were then sonicated in 95% Ethanol, followed by deionized water for 10 minutes to dislodge any visible particulate matter.

Slides were then submerged in a 70°C piranha solution for 10 minutes to remove any organic material. Piranha solution consists of a 3:1 (v/v) mixture of concentrated $H_2SO_4$ and 30% $H_2O_2$. The slides were then rinsed copiously with $H_2O$ followed by MeOH.

Once cleaned, the glass slides were placed in a 5% (v/v) solution of MPTMS in MeOH. Slides were allowed to derivatize for a minimum of 12 hours. Afterwards, they were

removed from the silane solution and rinsed copiously with MeOH, followed by $H_2O$, and then dried under a gentle stream of nitrogen.

Derivatized slides were placed into a colloidal solution and allowed to sit for 24 hours to complete nanoparticle self-assembly and form a single nanoparticle-layer substrate. After the prescribed time period, the substrates were removed from the colloid solution and rinsed with $H_2O$. Substrates were stored in $H_2O$ when not being immediately used.

### 2.5.2 Multilayer Preparation

To add further nanoparticle layers on to the substrates, the substrates were immersed in a 5 mM methanolic solution of PDT for 15 minutes, removed and rinsed with copious amounts of methanol followed by $H_2O$. Substrates were then immersed in a colloidal solution for 1 hour. The substrates were then removed and rinsed with copious amounts of $H_2O$ followed by methanol. This process was repeated until the desired number of colloid layers was obtained.

## 2.6 Nanorod Deposition

Nanorod deposition onto a glass slide was attempted using the method provided by Niidome [93]. This method involves the deposition of the positively charged NRs onto a negatively-charged glass surface. Firstly, a glass surface is made hydrophilic by immersing the slides for 5 minutes in a 1:1 mixture of ammonia and peroxide. Slides were then rinsed with water and subsequently immersed in a 1 mg/mL solution of the

polycation polymer PAH for 20 minutes to generate positive charges on the surface. After rinsing with water, the PAH-treated substrates were then placed in an aqueous 3 mg/mL solution of PSS for 20 minutes to produce a negative charge on the substrate surface.

The substrate, with a negatively charged surface, was rinsed with water and then immersed in the nanorod solution for 30 minutes. To prevent aggregation of the nanorods on the substrate, the slides were then treated with a 1 mg/mL solution of PDDA for 20 minutes.

## 2.7 Characterization of Nanoparticle Substrates

### 2.7.1 UV-Vis Characterization

Colloid nanostructures were characterized using a Cary 1E UV-VIS Spectrophotometer in absorbance mode. Instrument control was performed using the Cary WinUV software. For *ex-situ* measurements, a filter holder (Melles-griot) was attached to a machined metal plate. This allowed for the substrate to be placed in the sample beam of the instrument. *Ex-situ* scans were acquired from 400-900 nm at 333 nm/min and a resolution of 2 nm. The UV-Vis spectrum of a silane-derivatized slide was obtained as a background scan using the same instrumental settings.

For *in-situ* measurements, a 10 cm x 10 cm glass cell (spectrocell) was used to house the substrates. This cell was then mated to a metal plate which allowed the substrate to be

positioned in the sample beam of the instrument. Scans were acquired from 400-900 nm at 333 nm/min with a resolution of 2 nm. All *in-situ* measurements were performed in water, unless otherwise indicated. A background scan consisting of a silane-derivatized slide was obtained using the same instrumental settings.

### 2.7.2 AFM Characterization

AFM scans were obtained using a ThermoMicroscopes Digital AFM instrument operated under ambient conditions. Non-contact mode was used for all scans.

Non-contact AFM tips were obtained from Thermomicroscopes (Model 1650-00). AFM tips are of the I-type geometry and made of silicon. The nominal dimensions of the tips were 120 μm in length, 26-28 μm in width and a thickness of 3.6-4.4 μm. The tips had a force constant of 28-56 N/m, and a nominal resonant frequency between 307-384 kHz.

Scans were obtained at a 1000 nm by 1000 nm scan range, with a total of 200 lines scanned. The scan speed was 1000 nm/s. Detector settings (Proportional, Integral and Derivative) and the tip set point were optimized for each scan.

## 2.8 Second Harmonic Generation Measurements of Nanoparticle Substrates

The SH response of the colloidal structures was measured in a manner similar to that reported previously by the Brolo research group [94]. A schematic of the instrumental setup employed is show in Figure 2-2. Briefly, the pumping laser (Coherent Innova 400

$Ar^+$ ion laser) provided 13 W that was directed into a Ti/sapphire laser (Coherent Mira 900 F). The mode-locked Ti/sapphire laser produced a 76-MHz pulse train, but the pulse-repetition rate was reduced to 4.75 MHz by a pulse-picker system (Coherent Model 9200). This results in pulses of 200 fs in duration and a pulse energy of approximately 10 nJ. The working wavelength was 820 nm.

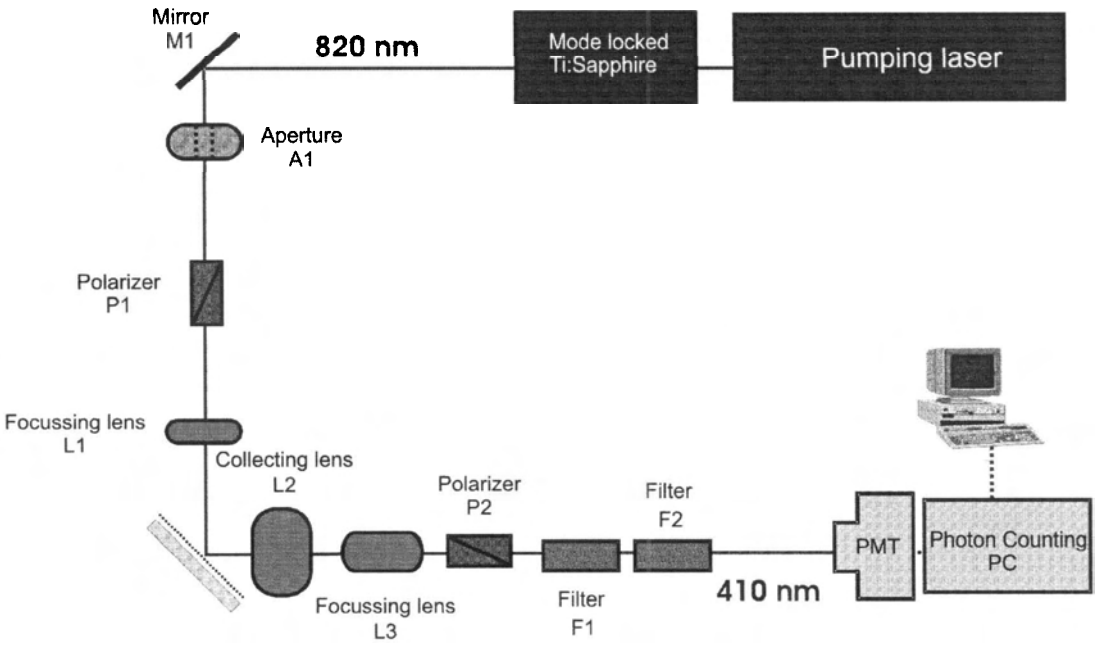


**Figure 2-2: Schematic of the Second Harmonic Generation apparatus utilized in these experiments.**

The laser light is directed onto a laser mirror M1 (CVI) and then through an optical aperture A1 (CVI) to confirm alignment and remove scatter. The laser signal then passes through polarizer P1 (Glan laser, CVI), to further improved the polarization purity of the

laser radiation. For all SH experiments, light with the polarization vector parallel to the physical plane of incidence (p-polarized) was used.

The laser radiation is then focused by means of a lens L1 (5 cm focal length) onto the surface of the substrate. It is estimated that the pulsed laser power density at the surface is on the order of 5 MW $cm^{-2}$.

The light from the surface was collected by a 50-mm photographic lens L2 (Cannon) and directed into lens L3 (CVI). Lens L3 was used to collimate the SH signal. Polarizer P2 (Glan laser, CVI) allowed for the selection of the polarization output. The SH signal then passes through a $CuSO_4$ filter (F1) to remove the bulk of the incident IR beam. The resulting beam then passes through an interference filter F2 (CVI) to ensure that any residual infrared light (ca. 820 nm) was removed before reaching the detector.

The SH signal was monitored using a photomultiplier tube (RCA) housed in a thermoelectric refrigerated chamber (Products for Research) operated at ca. -20°C. The photon counting system consists of an amplifier/discriminator (PAR) and a high-speed ratemeter (PAR). The PAR ratemeter also provides the high voltage necessary for the PMT. The analog readings from the photon-counting system was fed to a Pentium computer equipped with a data acquisition board (PCI 6024E from National Instruments (NI)) and a connector accessory (BNC 212, NI). The signal was digitized using customized data acquisition software written in LabView (NI).

## 2.9 Raman Measurements

All Raman measurements were performed on a Renishaw inVia Raman microscope system. The Raman signal output was sent to a PC computer running the WiRE Software (version 2.0, Renishaw Instruments). The acquisition parameters used to obtain the Raman spectra were varied depending on the experiment being performed.

### 2.9.1 Raman Measurements of Oxazine Deposited on Nanoparticle Substrates

Oxazine 720 was employed as the Raman analyte for SERS. A 5 mM methanolic solution of oxazine was prepared, and this solution was placed onto the SERS substrate so as to cover the entire surface. The ethanol was allowed to evaporate over a period of 10 minutes and resulted in the deposition of oxazine onto the nanoparticle surface. Residual or excess oxazine was removed by rinsing the substrate with copious amounts of water. The substrates were then dried under a gentle stream of nitrogen. Substrates were then placed in the Raman microscope system for measurement.

The excitation source was 785 nm laser light and was operated at 50% of total laser power (approximately 10 mW). A 50x objective was used for all measurements. Spectra were acquired from 100-2000 $cm^{-1}$ at 4 $cm^{-1}$ resolution with a 5 s acquisition time.

### 2.9.2 Raman Measurements of Oxazine Deposited on Gold Nanorods

To probe the enhancement of molecules absorbed on gold nanorods, the aggregation of nanorods in the presence of an analyte (Oxazine-720) was employed. To a 1 mL sample

of the as-prepared nanorod solution, 20 μL of a 5 mM methanolic Oxazine-720 solution was added and the resultant sample was mixed. Subsequently, 100 μL of 1 M NaCl was added to the sample to induce aggregation of the nanorods.

After allowing five minutes for aggregation to occur, a sample was placed onto a microscope slide and covered with a cover slip. The sample was then placed in the Raman microscope system for measurement. Acquisition parameters are as described in Section 2.9.1.

### 2.9.3 Raman Measurements of Powder Samples

Raman spectra of powder samples were obtained by placing a small amount of the powdered analyte between a microscope slide and a cover slip. The sample was then placed in the Raman microscope system for measurement. Raman spectra were obtained using 514.5 nm excitation, 50% laser power and a 50x objective. Spectra were acquired from 100-2000 $cm^{-1}$ at 4 $cm^{-1}$ resolution with a 60 s acquisition time.

# Chapter Three:UV-Vis and TEM Characterization of Colloidal Solutions

The characterization of the synthesized colloidal gold is critical because it is an important property of the nanostructures that were created in this work. In this chapter, the optical absorption spectra of the colloids will be examined to yield information about the size of the synthesized colloids. The sensitivity of the localized surface plasmons (LSP) to their environment will be demonstrated when the colloids are aggregated using a concentrated electrolyte solution. In addition, imaging of the colloids using a transmission electron microscope (TEM) will provide solid evidence as to the size distribution of the colloids.

## 3.1 UV-Vis Measurements of Colloidal Gold Solution

Colloidal gold solutions are intensely coloured due to absorption caused by the excitation of localized surface plasmons (LSP) [13]. These LSPs consist of coherent excitation of the conduction band electrons. The coherent excitation of the LSPs gives rise to a prominent absorption feature in the visible region of the electromagnetic spectrum [2].

### 3.1.1 Visible spectrum of Colloidal Gold

Shown in Figure 3-1 is the visible absorption spectrum of one of the samples of colloidal gold synthesized in this work.

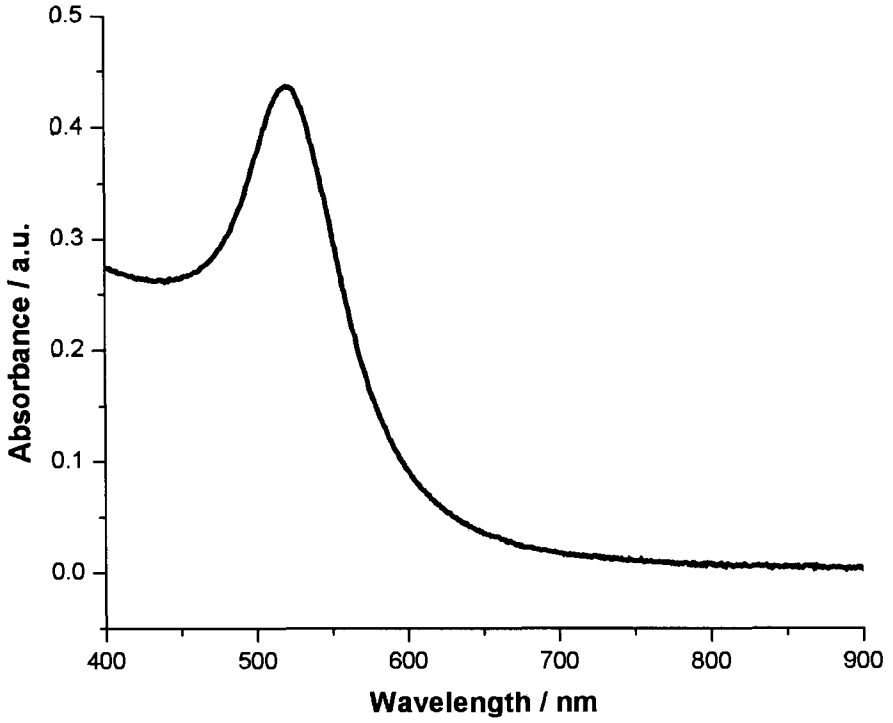


**Figure 3-1: UV-Vis Spectrum of 14 nm colloidal gold solution. Excitation of the localized surface plasmons results in the absorbance feature near 520 nm.**

There are several pieces of information that can be extracted from the UV-Vis spectrum of a gold colloid: the relative size of the colloids, the size distribution of the colloids, and the relative concentration of the colloidal solution. Each of these factors will now be discussed individually.

#### 3.1.1.1 Effect of Colloid Size on the Visible Spectrum

The approximate size of the colloids can be determined based on the wavelength location of the SP band. With increasing colloid size, the location of the LSP band undergoes a bathochromic shift [13, 21]. Conversely, colloids with decreasing size will undergo a

hypsochromic shift [2]. The location of the LSP band does not provide the absolute size of the colloids, because the shift of the LSP band is on the order of nanometers in the UV-Vis spectrum. Instead, for two colloid solutions, one can infer the relative size of the colloids based on their LSP band location. In the present case, the maximum absorption at 520 nm suggests that the colloids prepared here are somewhere near the 14 nm size regime based on comparisons from the literature [6].

Another option is to use a theoretical model for the absorption of colloidal gold, and to vary the size parameter until the theoretical curve exhibits a close resemblance to the experimentally-obtained curve [13, 21, 95, 96]. This method was not utilized here.

#### 3.1.1.2 Peak Width and the Size Distribution

The distribution of the colloid sizes can be qualitatively estimated based on the width of the absorption band in the UV-Vis spectrum. Samples which exhibit a large, broad absorption band over a large region suggest that the colloids have a large variation in their sizes, and would require further purification prior to use. Conversely, those possessing a UV-Vis spectrum consisting of a sharp absorption feature suggest colloids that have small size distribution. Using the synthetic method here, colloids with a coefficient of variation less than 20% [23] or with a standard deviation of 2 nm [2] are achievable.

One common method to describe the width of a peak is to measure the full-width at half maximum (FWHM) [2]. The points on the signal curve that correspond to one-half of the

maximum vertical value are initially located. The horizontal distance between these two points describes the width of the peak at one-half of its maximum intensity. An example of a FWHM measurement is shown in Figure 3-2.

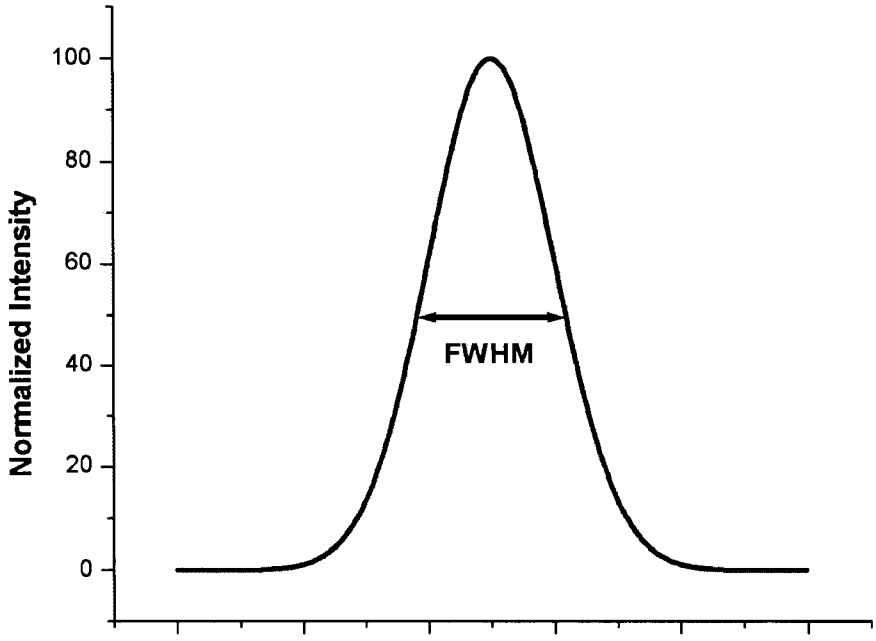


**Figure 3-2: Hypothetical example of a full-width at half-maximum (FWHM) measurement.**

The FWHM technique cannot be employed in the UV-Vis spectrum in Figure 3-1 due to the asymmetric nature of the absorption peak. This is the result of the bulk gold absorption feature at lower wavelengths than the LSP band [23].

One alternative is to measure the half-width at half-maximum (HWHM). As shown in Figure 3-3, the HWHM is obtained by first determining the half-maximum of the peak as

done when obtaining the FWHM (i.e.: The value on the y-axis that is one-half of the overall maximum). The half-width of the peak is determined from the edge of the peak (at this half-maximum) to the centre of the peak.

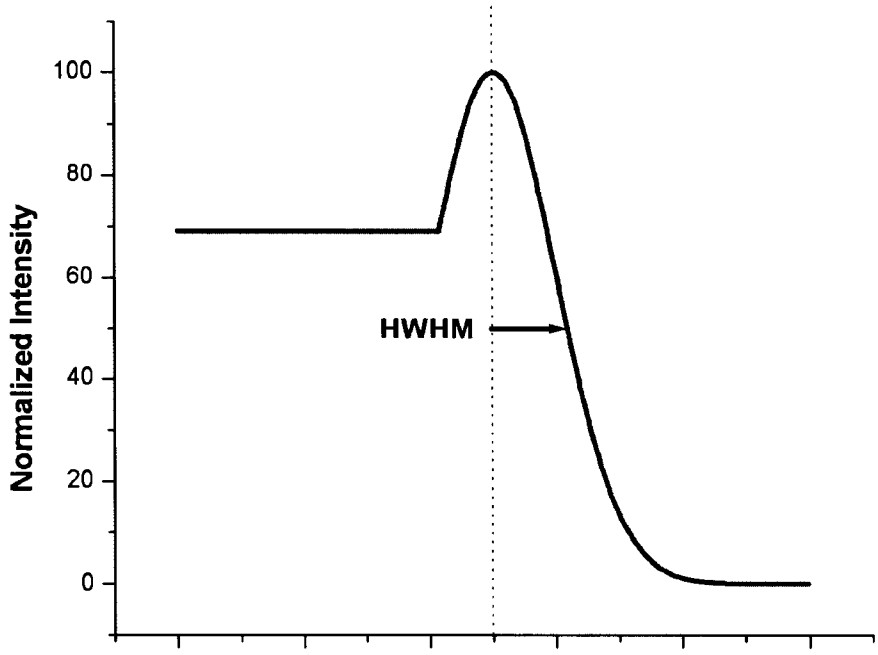


**Figure 3-3: Hypothetical example of a half-width at half-maximum (HWHM) measurement.**

The process for determining the HWHM for the UV-Vis spectrum from Figure 3-1 is demonstrated in Figure 3-4. In the case of Figure 3-4, the maximum occurs at 520 nm and has a maximum absorbance of 0.43612. One-half of the maximum absorbance, required for the HWHM, corresponds to 0.21806. Now one must travel along the spectrum until this absorbance value reaches the desired value. Transferring down from this point to the x-axis indicates that the UV-Vis spectrum has a value of 0.21806 at 560

nm. Therefore, the HWHM span corresponds to the distance between the absorption maximum and this point on the curve (560 nm – 520 nm = 40 nm). The HWHM can be multiplied by a factor of two, to yield the equivalent FWHM measurement (80 nm).

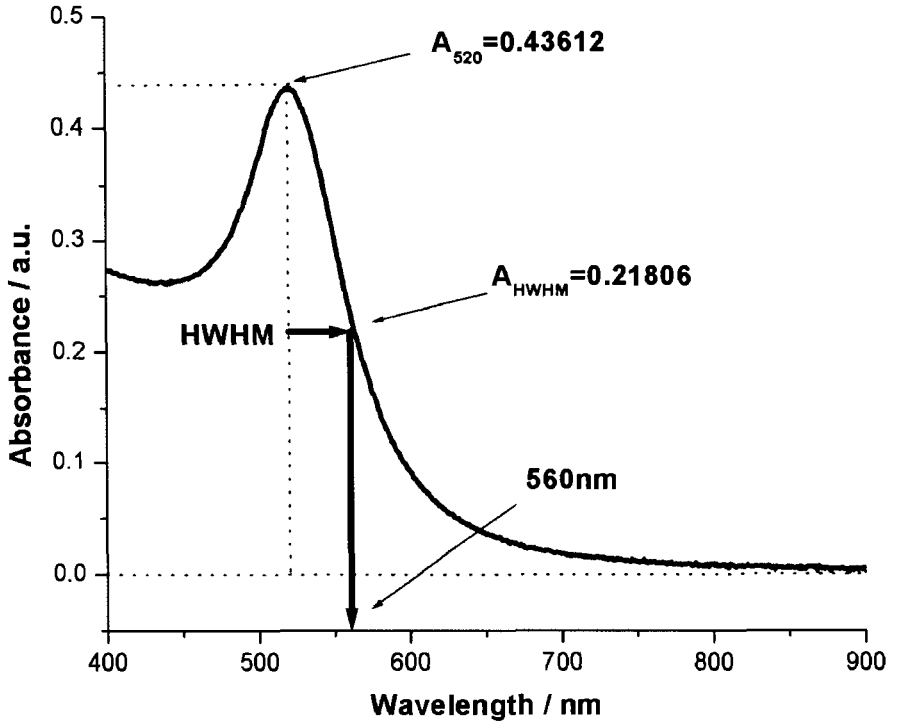


**Figure 3-4: UV-Vis spectrum from Figure 3-1, with overlays to demonstrate the HWHM measurement made here.**

Qualitatively, the shape of the UV-Vis spectrum is consistent with other preparations in the literature [4, 6, 8, 89, 95, 97]. The spectrum also lacks any overly-broad absorption features. Therefore, this suggests that the colloids are within the 2 nm standard deviation which is possible using this synthetic method.

### 3.1.1.3 Concentration of Colloid Solutions and its effect on the UV-Vis spectrum

When visible radiation passes through a medium, the amount of radiation absorbed (called the absorbance) is directly proportional to the path length ($\ell$) and the molar concentration ($C$) of the absorbing species. The relationship is often described as:

$$A = \varepsilon \cdot C \cdot \ell \tag{17}$$

Where $\varepsilon$ is a proportionality constant called the molar absorptivity. The molar absorptivity describes the "ability" or probability of an analyte to absorb radiation at a specific wavelength. This relationship between absorbance, molar absorptivity, concentration and path length is referred to as the Beer-Lambert law (or Beer's law). Thus, one can see that there is a direct-relationship between the concentration of an absorbing species and its absorbance.

Although the determination of the concentration of the colloid species was not performed here because it was not relevant to the work being undertaken, others have made this determination from the absorption spectrum [2, 4, 6]

### 3.1.2 Effect of colloid aggregation on the SP band

Colloidal solutions (as they are referred) are technically a suspension, but do not "settle out" (or separate) as would be expected. This is due to a net charge which is inherent on the outer shell of the colloids [15]. This electrostatic charge ensures that colloids maintain a minimum distance from each other and therefore cannot aggregate.

The surface plasmons of gold colloids are extremely sensitive to their local environment [30]. When aggregation of the colloids occur, that is to say, when the colloids irreversibly approach too closely, the dipole approximation breaks down [98]. Instead, one must treat each of the colloids as a multipole, because adjacent colloids thus have an affect on each other [98]. This results in the formation of an absorption feature that is red shifted and is characteristic for aggregated colloids.

Aggregation can be accomplished through the addition of a variety of electrolytes [23]. When an electrolyte is added to the colloid, the electrostatic repulsion that prevents the colloids from "settling out" is inhibited. The electrolyte essentially screens the outermost charged layer enveloping the colloids, and allows for close contact of individual colloids. The most common anions used to induce aggregation are those belonging to the halide series: bromide, chloride and iodide are routinely used [23]. Here, a small amount of a concentrated (ca. 1 M) solution of NaCl was added to the colloid solution to induce aggregation.

Colloid aggregation produces very prominent changes in the UV-Vis spectrum, as demonstrated in Figure 3-5:

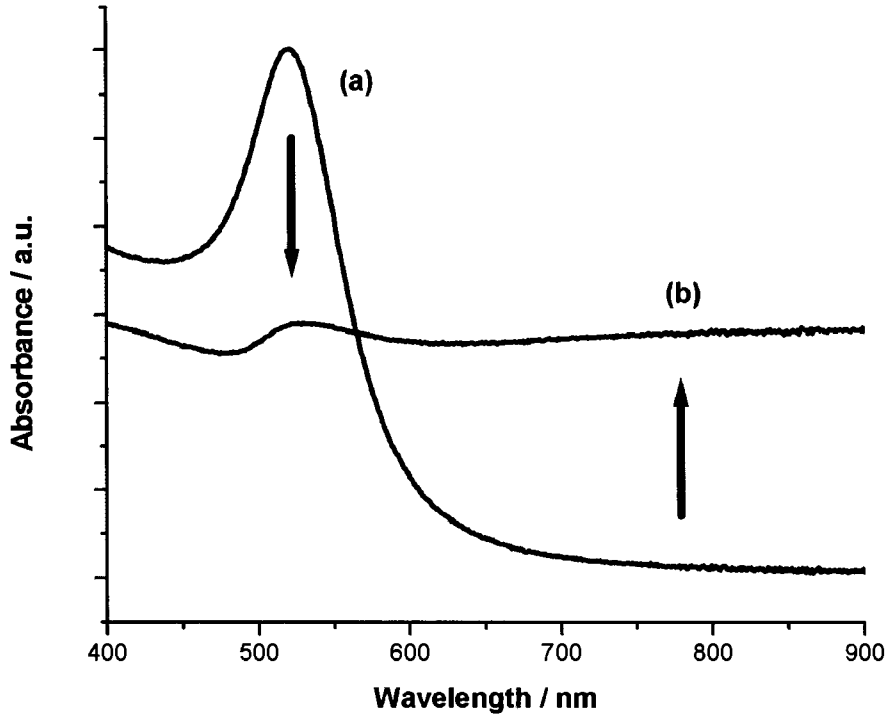


**Figure 3-5: UV-Vis spectrum of a (a) 14 nm colloidal gold solution and (b) the 14 nm colloidal gold solution after the addition of an electrolyte to induce aggregation. Aggregation results in the attenuation of the LSP near 520 nm while an increased absorption at longer wavelengths is observed.**

Figure 3-5(a) shows a typical UV-Vis spectrum of a 14 nm colloidal gold solution. As expected, a pronounced absorption near 520 nm occurs due to the excitation of the LSP. When colloid aggregation occurs, there is an attenuation in the LSP band at 525 nm. Concomitantly, there is an increase in absorbance at longer wavelengths (ca. 800 nm) resulting from the aggregate structures (Figure 3-5(b)).

The inherent sensitivity of the LSP of colloids to aggregation, and the dramatic changes in the UV-Vis spectrum that it entails, will be exploited in the construction of the multilayer nanostructures. The position of the LSP band provides an indication of the local environment that the colloids are residing in: If bands appear at longer wavelengths, this suggests aggregation of the colloids in the multilayer nanostructures.

### 3.1.3 Colloid Aging

To use colloidal gold as a major building block in the multilayer nanostructures, it must be demonstrated that this building block is stable under normal storage conditions. When stored under proper conditions (in an amber bottle, and at 4°C), colloidal gold is extremely stable.

The most common problem encountered with colloidal solutions is the growth of bacteria [23]. One way to prevent flocculation is to add a small amount of preservative, such as gelatin or sodium azide [14]. When such care is taken, colloidal samples can survive indefinitely. This is demonstrated by Faraday's samples of colloidal gold that exist to this day at the Royal museum in London [16].

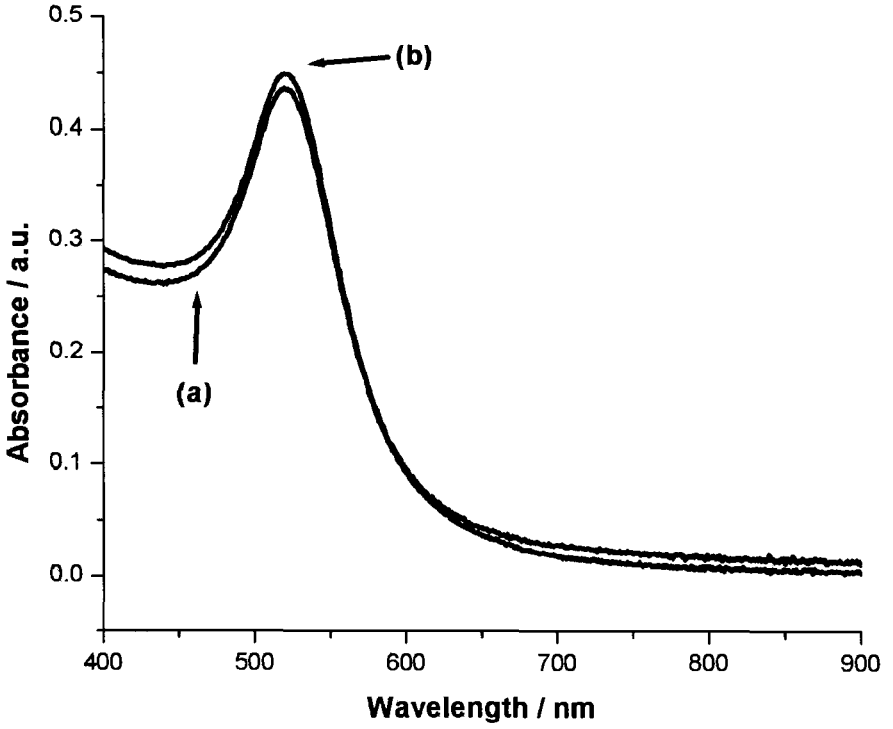


**Figure 3-6: UV-Vis spectrum of (a) 14 nm colloid solution (as prepared) (b) The same sample of colloids, after being stored for 12 months in an amber bottle at 4°C.**

The versatility and stability of the colloidal gold prepared in this work is demonstrated in Figure 3-6. It can be seen that there is virtually no change in the optical response of the colloidal solution after being stored for twelve months.

## 3.2 TEM Characterization of Colloidal Gold Solution

The transmission electron microscope (TEM) allows for the ability to make observations at the sub-micron level [99]. Whereas light microscopes are limited in resolution by the wavelength of light, TEM provides increased resolution and ability to image materials

because of the shorter wavelength of an electron beam [100]. In fact, TEM offer approximately four orders of magnitude (10,000 times) greater resolving power than a light microscope and can image features down to 3 nm in size [99, 100].

The TEM was invented in 1932 by Ernst Ruska and Max Knoll, who received a Nobel prize in 1986 for their work. TEM, along with its variants, still has an impact in fields such as biology, chemistry, geology and materials science [101].

The theory of TEM imaging is analogous in many ways to that of a light microscope [102]. In a light microscope, light from a white source is focussed on to a sample (usually) on a glass slide. The light is transmitted through the sample, through an objective lens and to the observer's eye through a second magnifying lens, called the ocular or eyepiece. The resultant magnification is from the product of the objective and ocular lenses [103]. The viewer then observes differences in light intensity due to the differential absorption of light by the sample.

In TEM, a high voltage (ca. 40,000 to 100,000 V) is used to accelerate a finely focused electron beam on to a sample deposited onto a support grid (the support grid is analogous to glass slides when using a light microscope). The electron beam is then focussed onto a photographic plate or fluorescent screen for detection [102]. In TEM, contrast is obtained from the scattering of electrons by the sample in a manner analogous to that of a light microscope.

When an electron beam passes through a material and is diffracted, dark grey or black areas appear in the resultant TEM image. Conversely, areas that do not contain any specimen or have not been appropriately stained will appear as a white or light grey colour [103].

In general, atoms with higher atomic numbers are more capable of scattering electrons because of their greater electron density [101]. Therefore, biological materials are often stained for visualization using salts of heavy metals such as uranium, lead, osmium, and of course, gold [100].

### 3.2.1 Calibration of TEM using Commercial Colloidal Gold Solution

As with other imaging techniques, it is necessary to calibrate the instrument response to obtain accurate images of a known scale. In this case, imaging must be performed on a sample of known size, and the size of the features in the obtained TEM image must be correlated to the actual feature size, to produce a scaling/correction factor. Theoretically, this produces a one-point calibration, and it will be assumed that the instrument response is linear with feature size being measured.

To accomplish this, the electron voltage and other instrumental parameters were kept constant for all images obtained here, and calibration was accomplished through the use of a commercial colloidal gold solution of known size.

This colloidal gold solution has a particle diameter distribution between 8-12 nm with a 10 nm nominal diameter. A sample of this colloidal solution was deposited onto a TEM grid using the procedure described in the experimental section, and the TEM image was obtained (Figure 3-7).

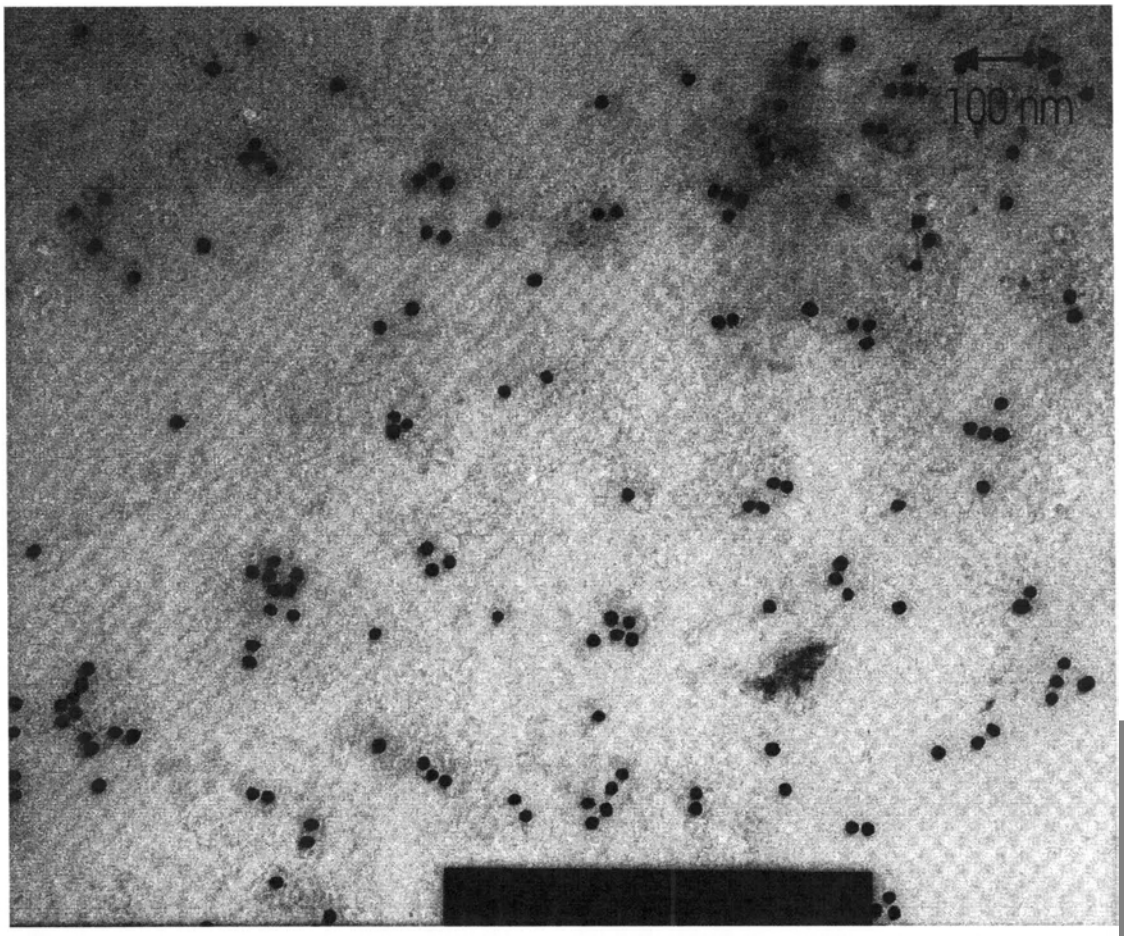


**Figure 3-7: TEM image of commercially-available colloidal gold solution.**

After the images had been transferred to the JPEG format, they were examined using the Adobe Photoshop software package. To measure the size of the colloids, all particles

were assumed to be spherical in shape. Using the circle drawing tool, a circle was drawn around each of the colloids, and the area of the colloid was measured (in terms of square pixels per colloid).

The area values obtained were adjusted to yield the diameter of the colloid. The values obtained from the software program listed the result in terms of pixels. A correction factor was employed to obtain results in a more palatable unit (nm).

Measuring a large sample population should result in a Gaussian distribution of values around a mean value. This mean value should correspond to the mean value of the colloid size distribution as stated by the supplier (10 nm). So the average colloid diameter (in pixels) will correspond to the mean value (in nm). From this, the scaling factor can be obtained.

The average colloid diameter was determined to be 17.86 pixels. The "true" diameter is known to be 10 nm. This gives a scaling factor of 1.78571 pixels / nm (or 0.560 nm / pixel).

All TEM images were obtained under the same experimental conditions. Therefore, it is assumed that this scaling factor was applicable to all images obtained here.

### 3.2.2 TEM Imaging of Colloidal Gold Solutions

With the experimentally-obtained calibration factor, it was then possible to make accurate size measurements of the synthesized gold colloids. In a manner similar to that described in 3.2.1, the TEM image of the colloidal gold was obtained, and the resultant image was scanned into a digital (JPEG) format for manipulation and analysis (Figure 3-8).

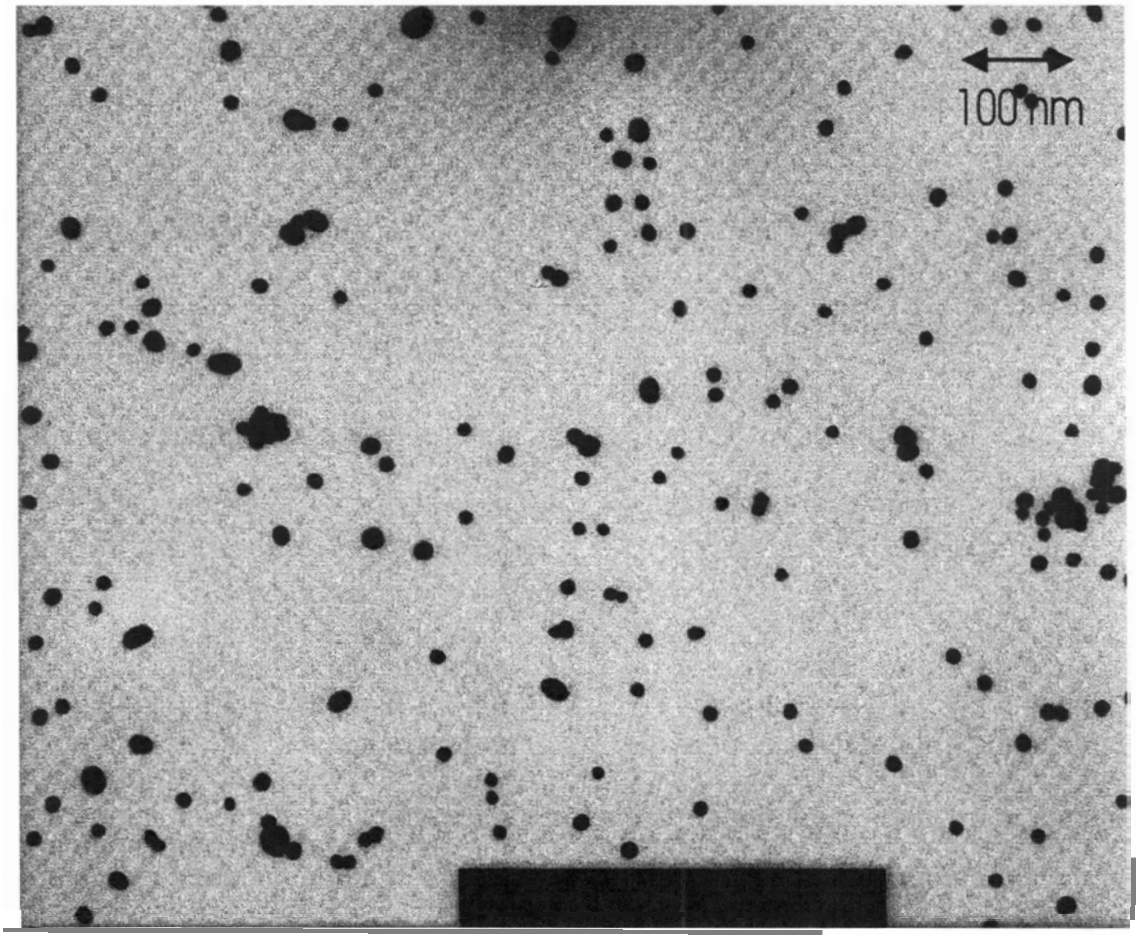


**Figure 3-8: TEM image of colloidal gold solution synthesized in this work.**

At least 100 individual colloids were analyzed, and their area obtained using the circle drawing tool in Adobe Photoshop. Aggregates, or particles that were not circular in diameter were omitted. The diameter of the colloids was thus determined to be (14 ± 2) nm. The mean value and standard deviation are in good agreement with previously reported results for this synthetic method [6, 22]. While the value is slightly higher than the expected 12 nm colloid diameter, this can be adjusted during the colloid synthesis: Increasing the amount of reducing agent added will result in a decrease in the average colloid diameter [23]. Nonetheless, a discrepancy of 2 nm in the colloid diameter will have no detrimental effect upon the work performed here.

It is also possible to plot a histogram of the diameter of colloids obtained to observe the size distribution (Figure 3-9). It can be seen that the size distribution of colloids obtained here is roughly Gaussian in nature, as would be expected [23]. An anomalously low number of colloids in the 15 nm diameter range were observed. This deviation could indicate a potential bias in the method used to obtain these results. Alternatively, it could be the result of the small number of sample observations made.

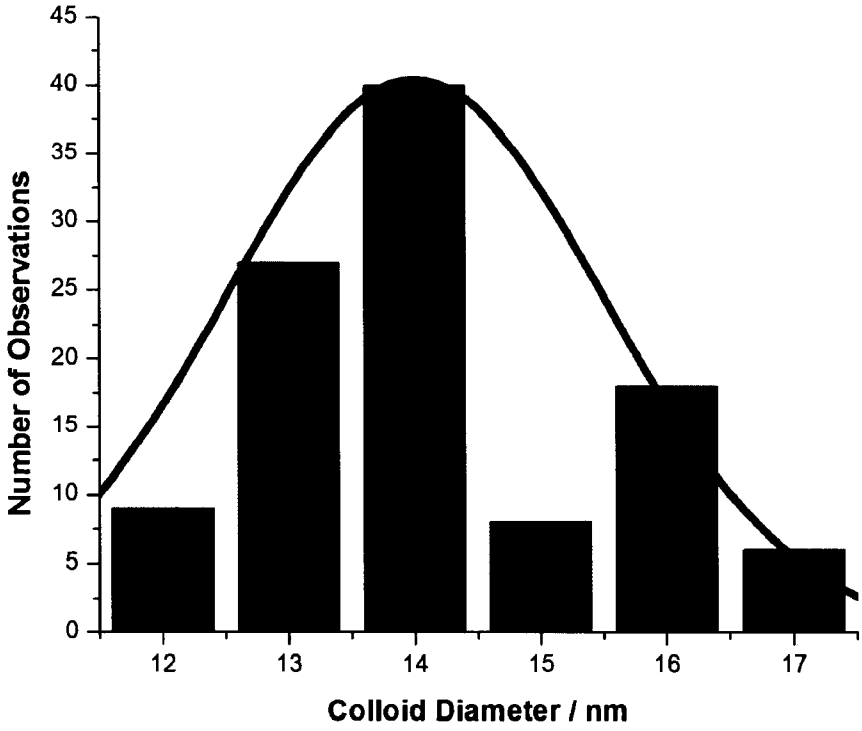


**Figure 3-9: Distribution of colloid diameters in the synthesized colloidal gold solution. The solid black line represents a Gaussian distribution with mean value 14 nm and a 2 nm standard deviation.**

# Chapter Four: Characterization of Colloidal Multilayer Structures

In this chapter, it will be described how multilayer substrates consisting of alternating layers of gold nanoparticles and dithiol linker molecules are constructed and characterized. In Section 4.1, glass slides are derivatized using a modified silane in order to facilitate the deposition of gold nanoparticles onto the glass surface. In Section 4.2, the characterization of a single gold nanoparticle layer deposited onto the derivatized glass slide will be presented. The optical response of the system was recorded using UV-Vis spectroscopy, while the resultant surface morphology was monitored using an AFM. In Section 4.3, deposition of further gold nanoparticle layers are explored, and once again the systems will be characterized using UV-Vis spectroscopy and AFM.

## 4.1 Surface derivatization using 3-mercaptopropyltrimethoxy silane

Colloidal gold does not irreversibly bind to a glass surface [6, 8]. This is shown in Figure 4-1, in which an ordinary a microscope slide was immersed in a solution of colloidal gold for 24 hours. The UV-Vis spectrum of the slide was taken before and after the immersion. No change in the optical response of the slide is observed in Figure 4-1, indicating that no deposition of colloidal gold has occurred.

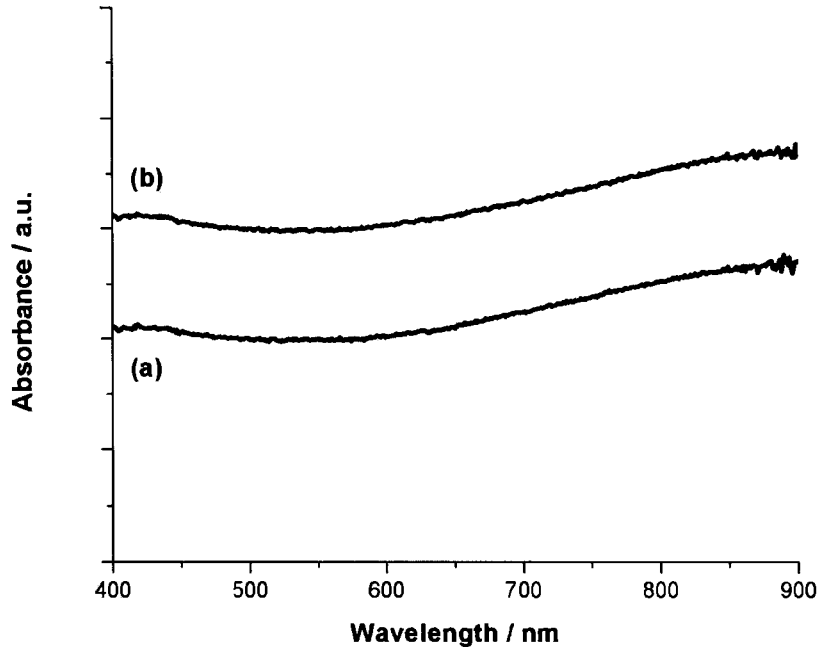


**Figure 4-1: UV-Vis spectrum of (a) a glass slide and (b) the same glass slide placed in colloidal gold for 24 hours. The spectra have been offset to allow for easier comparison.**

Hence, chemical derivatization of the glass surface is a necessary first step in the synthesis of the nanoparticle substrate. There are two common methods for the deposition of colloidal gold onto glass surfaces: Electrostatic deposition of the colloids onto a charged glass surface [104], or the use of the well-known gold-thiol chemistry [29, 105]. The electrostatic deposition method involves modifying the gold colloids to produce monolayer-protected clusters (MPCs) with a charged chemical group. A charged group of the opposite charge is then placed onto the surface to allow for deposition through electrostatic means [104, 106, 107]. A schematic representation of this method is shown in Figure 4-2.

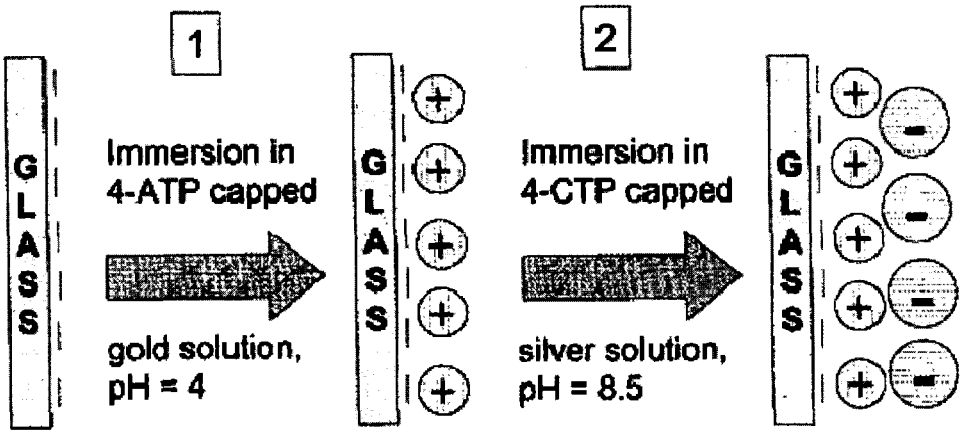


**Figure 4-2: Schematic demonstrating the electrostatic deposition of positively-charged gold nanoparticles (4-aminothiophenol; 4-ATP) onto a negatively-charged glass surface (Step 1). At pH 4, the glass surface is inherently negatively charged. Subsequently, negatively-charged silver nanoparticles (4-carboxythiophenol; 4-CTP) are deposited on top of the gold nanoparticle layer (Step 2). Reprinted with permission [106]. Copyright 2000 American Chemical Society.**

A slight modification of this method is to use polymer networks containing charged moieties in order to facilitate gold nanoparticle deposition [95, 108, 109].

The more popular alternative is to utilize gold-thiol chemistry to facilitate nanoparticle deposition [10-12, 29, 105]. The gold-thiol bond is very stable and irreversible in nature [12, 105, 110] and therefore is highly desirable to use in the construction of nanoparticle arrays. The half-reaction of a thiol molecule with gold can be represented by:

$$RSH + Au \rightarrow Au(SR)_{(ads)} + H^+ + e^- \quad (18)$$

The goal, therefore, is to modify the glass surface to yield a pendant thiol moiety that is capable of reacting with the gold nanoparticles to yield the desired gold-thiol bond. One such method involves the derivatization of the glass surface using MPTMS [6]. The glass surface is first treated with piranha solution (3:1 $H_2SO_4/H_2O_2$) to produce pendant hydroxyl groups [1, 89]. When the glass slides are introduced into a methanolic solution of MPTMS, the pendant hydroxyl groups on the glass surface react with the methoxy group of MPTMS. The net result is the loss of a proton from the hydroxyl group to that of the methoxy moiety, and subsequent production of methanol as a by-product, and formation of the thermodynamically stable Si-O bond [95, 111, 112]. The reaction scheme representing the derivatization of the glass surface is shown in Figure 4-3:

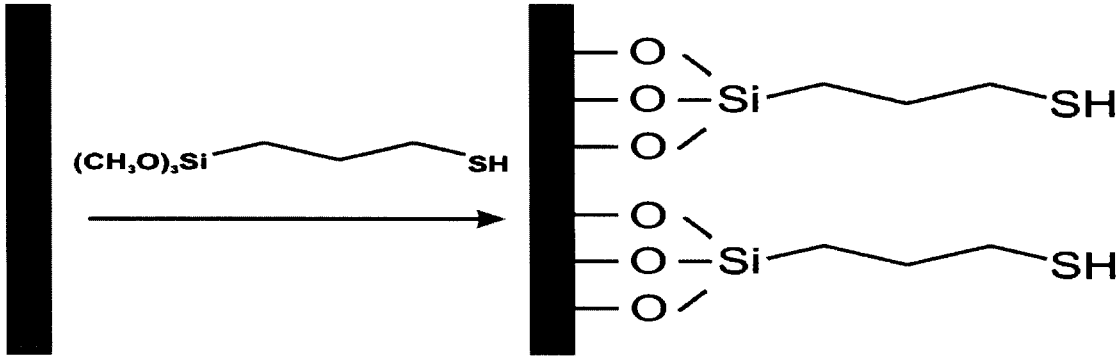


**Figure 4-3: Surface derivatization of a glass slide using MPTMS. This results in a pendant thiol moiety which will allow for nanoparticle deposition.**

### 4.1.1 UV-Vis response of derivatized surface

Surface derivatization, while greatly affecting the chemical properties of the glass surface, have little or no effect on the optical properties of the glass itself, as demonstrated in Figure 4-4.

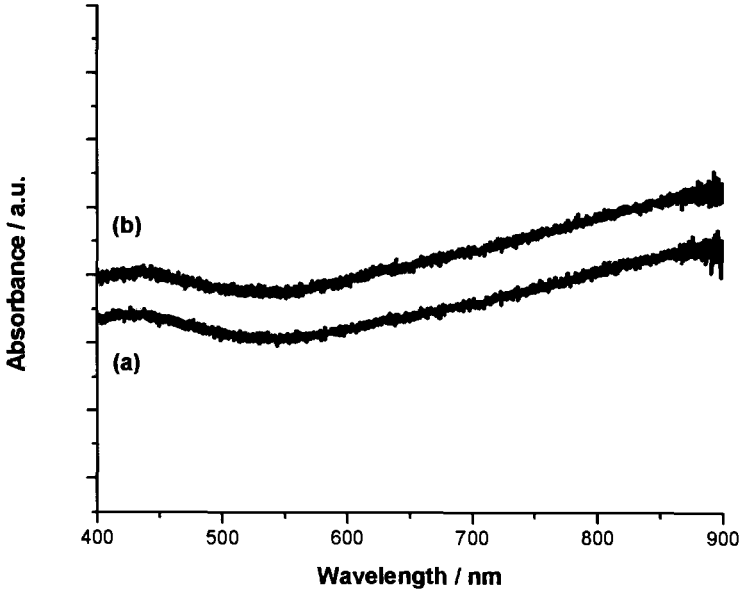


**Figure 4-4: UV-Vis spectrum of a (a) glass slide and (b) a glass slide derivatized with MPTMS. The spectra have been offset to allow for easier comparison.**

There are no chromophores in MPTMS that show appreciable absorption within the optical region of interest here (400 – 900 nm), therefore no change in the optical properties would be expected [1, 112].

### 4.1.2 AFM characterization of derivatized surface

Derivatization of the glass surface with MPTMS has a slight affect on the physical roughness of the glass slides. Shown in Figure 4-5 are AFM images of a glass substrate before and after modification with MPTMS.

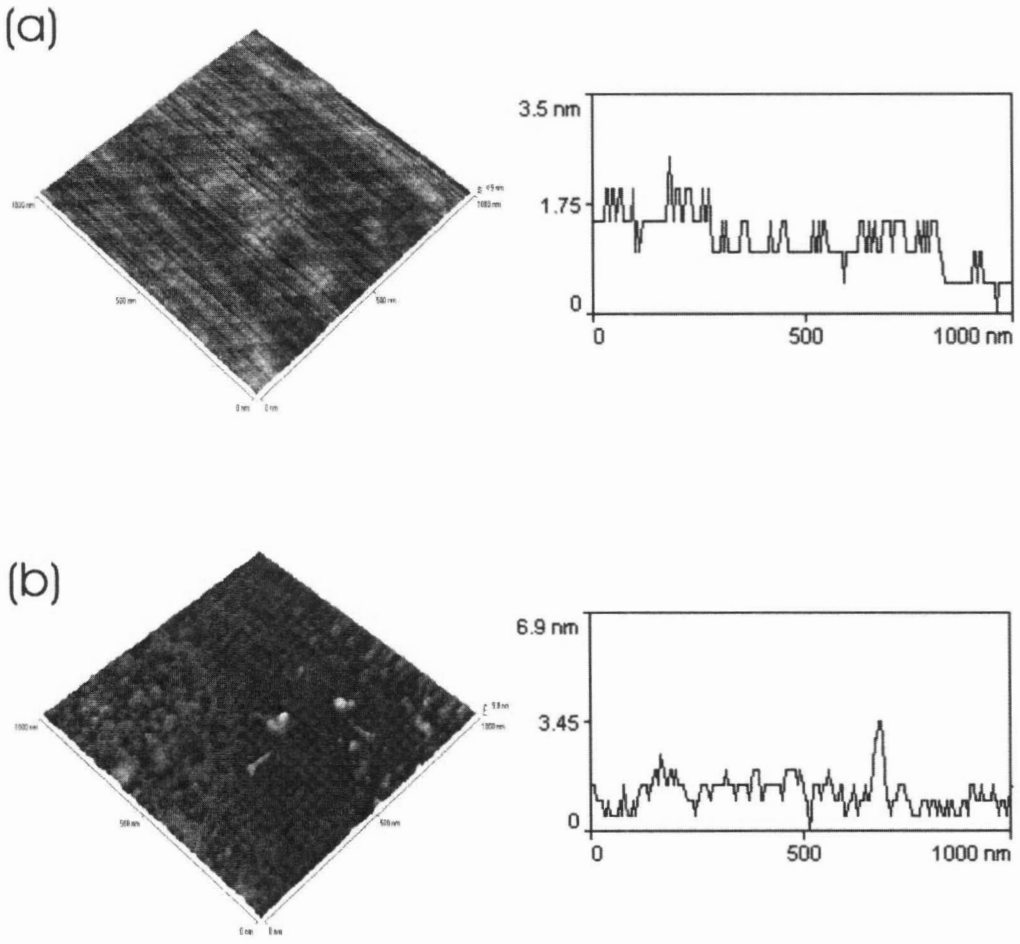


**Figure 4-5: AFM image and representative line scan of (a) a glass slide and (b) a silane-derivatized glass slide.**

One common method to describe the roughness of a surface is to calculate the root-mean-square (*RMS*) roughness. This parameter is given by:

$$RMS = \sqrt{\frac{1}{N}\sum_{i=1}^{N}\langle Z_i - Z\rangle^2} \tag{19}$$

Where $N$ is the number of data points, $Z_i$ is the height of the image at a particular data point, and $Z$ is the mean height across the entire image. A lower RMS value indicates a surface with smaller protrusions or surface features.

The RMS value obtained for the underivatized glass slide was (0.5 ± 0.2) nm. The low RMS value suggests a smooth, flat surface with very few protrusions or features on the glass surface. After derivatization of the silane on the glass surface, the RMS roughness increases slightly to (0.7 ± 0.2) nm. The slight increase in roughness after derivatization is expected based on reports in the literature, suggesting that the thin-film is not necessarily flat and homogenous [113]. Instead, small protrusions exist, as can be seen in Figure 4-5(b). These values also agree with those published by Seitz *et al*, who obtained a RMS roughness of 0.388 nm and 0.785 for glass and silane derivatized glass, respectively [114].

## 4.2 Deposition of one colloidal layer onto modified glass substrates

With derivatization of the glass surface complete, nanoparticle deposition can now occur owing to the reaction of the pendant thiol moiety with the gold nanoparticle. The surface

coverage of a monolayer of gold nanoparticles on the glass surface approaches 30% at saturation, as determined by Grabar *et al.* using field-emission scanning electron microscopy [4]. This low surface coverage is due to the interparticle repulsion experienced between individual nanoparticles, as described previously (Section 1.3.1).

### 4.2.1 UV-Vis spectrum of one colloid layer

After immobilization of a nanoparticle layer onto a glass surface, this system was monitored using UV-Vis spectroscopy. The *in-situ* UV-Vis spectrum of a monolayer of gold nanoparticles deposited onto a derivatized glass surface is shown in Figure 4-6.

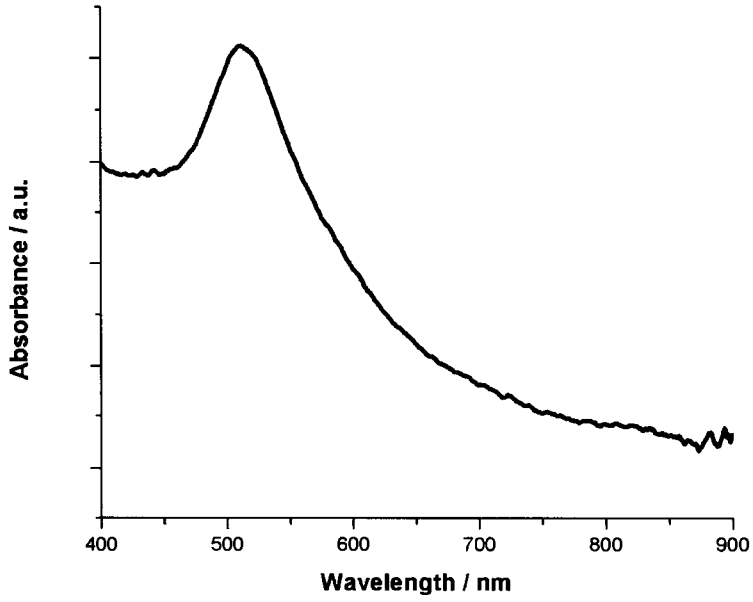


**Figure 4-6: *In-situ* UV-Vis spectrum of 14 nm gold nanoparticles deposited onto a glass surface modified with MPTMS.**

Qualitatively, the spectrum provided in Figure 4-6 is similar to that of the gold nanoparticle solution presented in Figure 3-1. The spectrum in Figure 4-6 exhibits a pronounced absorption band near 520 nm due to the excitation of the SP of the gold nanoparticles. This absorption band is responsible for the intense red colour of the gold nanoparticles. The fact that the location of the SP band is the same as that for the nanoparticle solution indicates that the nanoparticles assembled onto the surface are indeed well-separated.

When the nanoparticle assembly is removed from solvent and allowed to dry, a pronounced morphological change occurs: Electrostatic repulsion between the individual nanoparticles are not as strong in air due to the local dielectric conditions [115]. Therefore, an irreversible aggregation of the nanoparticles occurs, resulting in a shift in the SP resonance to longer wavelengths. This effect is demonstrated in Figure 4-7.

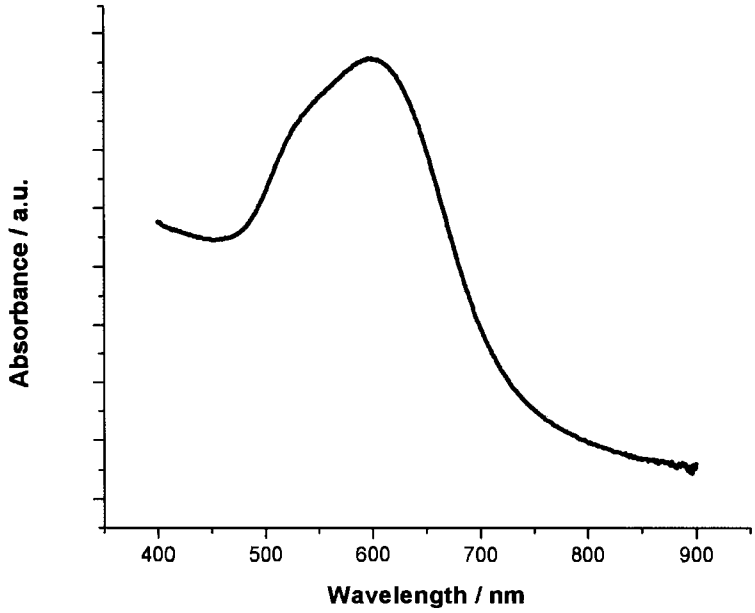


**Figure 4-7: *Ex-situ* UV-Vis spectrum of 14 nm gold nanoparticles deposited onto a glass surface modified with MPTMS.**

The *ex-situ* UV-Vis spectrum in Figure 4-7 exhibits a broad SP band from 500-700 nm. This band consists of an absorption near 600 nm, with another smaller absorption feature centered at 520 nm as a shoulder of the larger peak. The latter is the SP band for colloids that are well-spaced on the surface and are non-interacting. The former is a red-shifted SP band which is indicative of colloid aggregation on the surface. Therefore, a mixture of aggregate structures and non-aggregated nanoparticles exists in this state. Particle aggregation can be avoided by depositing a layer of dithiol molecule on top of the nanoparticle layer [116]. In that case, the SP band will remain at the same location in water and in air, indicating that no aggregation has occurred. Presumably, the dithiol molecule attached to the colloidal gold inhibits aggregation by acting as a "blocking group".

### 4.2.2 AFM characterization of one colloid layer

Morphological information about the nanoparticle assembly may be obtained through the use of atomic force microscopy (AFM). In AFM, a sharp tip is mounted at the end of a cantilever, and the tip is raster scanned across a surface. A laser beam, focussed onto the cantilever, is reflected onto a set of four photosensitive diodes. In contact-mode AFM, the tip scans the surface, and deflection in the tip due to repulsion between the tip and the surface is monitored on the four photosensitive diodes [117].

Under high loads, changes in the sample morphology can be induced [117]. To circumvent this undesirable outcome, it becomes necessary to avoid direct sample-tip interactions. In tapping-mode AFM, the cantilever is oscillated at its resonant frequency and positioned just above the sample surface, resulting in tip-surface contact for a very small fraction of its oscillating period. The short tip-sample interaction period dramatically reduces the lateral forces exerted on the surface during scanning, and thus allows for imaging of "soft" samples. The phase difference between the oscillations of the cantilever driving piezo, and the detected oscillations are used to construct the AFM image [117].

Lateral measurements observed using AFM are larger than the true dimension due to an effect known as tip-sample convolution [3, 10, 111, 118]. Tip-sample convolution arises from the finite-size of the AFM tip as it scans over a surface. The resultant measurement

of the surface features are influenced by the size of the AFM tip. This process is illustrated in Figure 4-8.

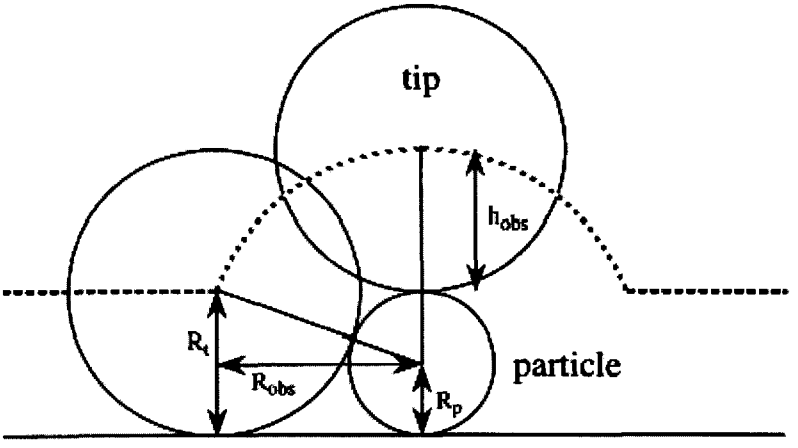


**Figure 4-8: Pictoral representation of an AFM tip passing over a single spherical nanoparticle of radius $R_p$. Because of the finite size of the AFM tip (radius $R_t$), the actual size of the nanoparticle imaged is $R_{obs}$. Figure rerinted from [111] with permission from Elsevier.**

As can be seen from Figure 4-8, tip-sample convolution limits the observation of nanometric details. This effect is often described using a hard-ball model [111]. When an AFM tip of radius $R_t$ nears a particle (of radius $R_p$), the radius of curvature travelled by the tip is $R_{obs}$. This convolution results from the side-wall interaction of the AFM tip against the nanoparticle surface. The relationship between these quantities can be described using [111]:

$$R_{obs} = 4\left(R_p \cdot R_t\right)^{\frac{1}{2}} \tag{20}$$

While lateral dimensions are affected by tip-sample convolution, height measurements are not [111, 118]. The measured height ($h_{obs}$) generally corresponds well to the actual particle diameter ($2R_p$).

Shown in Figure 4-9 is the topographic image and representative line scan of one layer of colloidal gold deposited onto a derivatized glass surface.

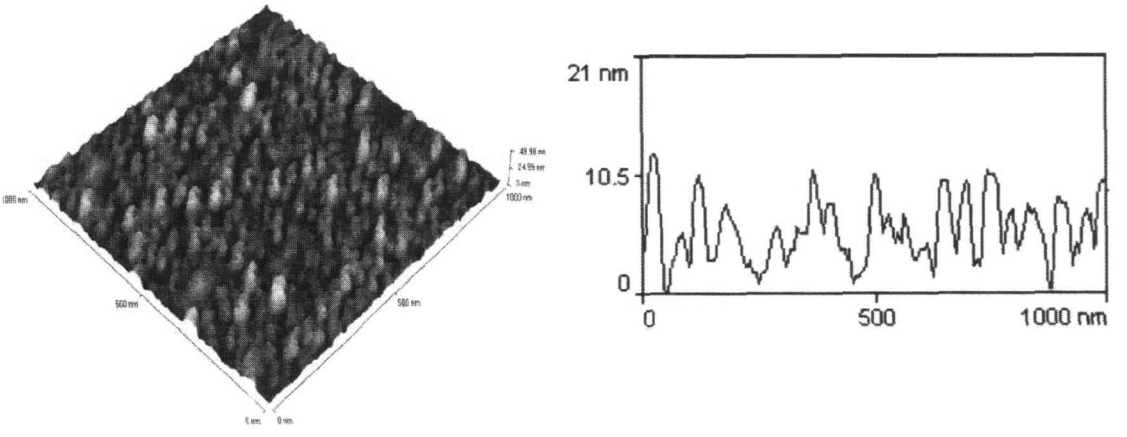


**Figure 4-9: AFM topographic image and representative line scan of 14 nm colloidal gold deposited onto a glass surface modified with MPTMS.**

The AFM topographic image in Figure 4-9 shows protrusions on the sample surface. The resultant line scan indicates that these protrusions are approximately 10.5 nm in height, which is on the order of the nanoparticle diameters (14 nm) determined by TEM (Section 3.2.2) and estimated from the UV-Vis spectrum (Section 3.1.1). The observed lateral

dimensions of these features are approximately 50 nm. Using Equation (20) and a nominal tip radius of 20 nm, this yields a particle diameter on the order of 14 nm.

The measured RMS roughness value was determined to be (3.1 ± 0.4) nm. Seitz *et al.* obtained RMS roughness values ranging from 3.17 to 5.53 nm for a single colloid layer, depending upon the time allowed for colloid deposition [114].

## 4.3 Construction of multilayer substrates

The construction of multilayer substrates can be easily accomplished by alternately immersing the substrate in solutions of dithiol linker molecule and gold nanoparticles [89]. The process for constructing the multilayer substrates is shown in Figure 4-10.

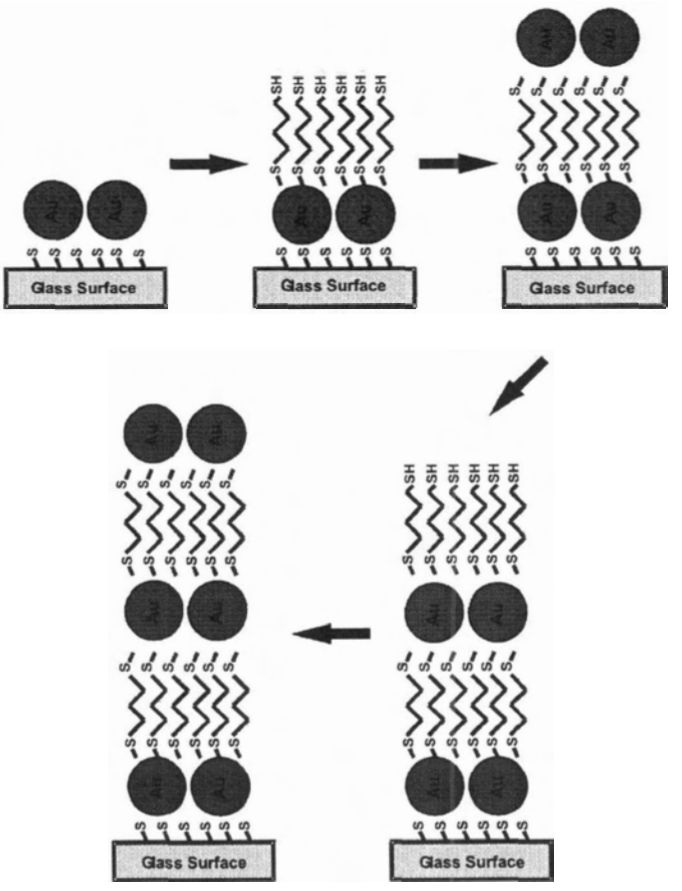


**Figure 4-10: Schematic demonstrating the stepwise construction of multilayer substrates through the alternating immersion in a dithiol or gold nanoparticle solution. In this example, a substrate consisting of 3 nanoparticle layers has been constructed. Note that this schematic assumes that samples have not been exposed to air, at which time aggregation of the colloids would occur.**

Once prepared, the substrates of varying nanoparticle layers were characterized using UV-Vis spectroscopy and AFM.

### 4.3.1 UV-Vis response of multilayer structures

Because gold colloids are coloured, it is possible to monitor the deposition of colloids using spectrophotometric means. Shown in Figure 4-11 are the *ex-situ* UV-Vis spectra for nanostructured substrates ranging from 1 to 17 nanoparticle layers (for odd number of nanoparticle layers).

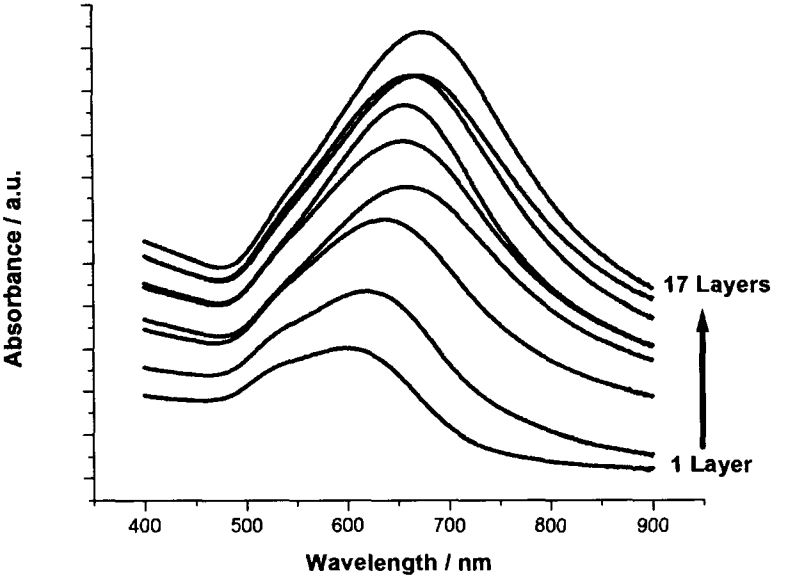


**Figure 4-11: *Ex-situ* UV-Vis spectra of multilayer structures for odd number of colloid layers. Increasing nanoparticle deposition results in an increase in the overall absorbance, as well as a shift in the plasmon maximum to longer wavelengths.**

There are two particular features that can be extracted from Figure 4-11: the increase in absorbance with increasing number of nanoparticle layers, and the concomitant shift in the wavelength of maximum absorption.

The former occurs because of the increase in the number of colloids as more layers are formed. In previous work, it has been assumed that the number of colloids deposited remains the same for each layer deposited [89]. The concentration of an absorbing species can be related to the absorbance using Beer's law, which was discussed previously in Section 3.1.1.3. There should then be a linear increase in absorbance with increasing number of layers.

One common method to examine this relationship is to plot the absorbance at the wavelength of maximum absorption against number of nanoparticle layers. The net result, as discussed above, should be a linear increase in the absorption of the system [89, 95]. This method cannot be utilized here because of the shift in the wavelength of maximum absorption as an increasing number of nanoparticle layers are deposited.

One way to overcome this fact is to utilize the integrated peak area for the absorption due to the deposited nanoparticles. It has been established that the absorption feature between 475 and 900 nm is due to the gold nanoparticles [4, 6]. Therefore, integration between these boundaries will yield a representative quantity, the integrated absorption coefficient, which should be proportional to the number of layers of gold nanoparticles deposited onto the glass surface [95]. If the number of colloids is doubled, then the integrated peak absorption would also double, as dictated by Beer's law. The integrated peak areas for the UV-Vis spectra from Figure 4-11 is presented in Figure 4-12.

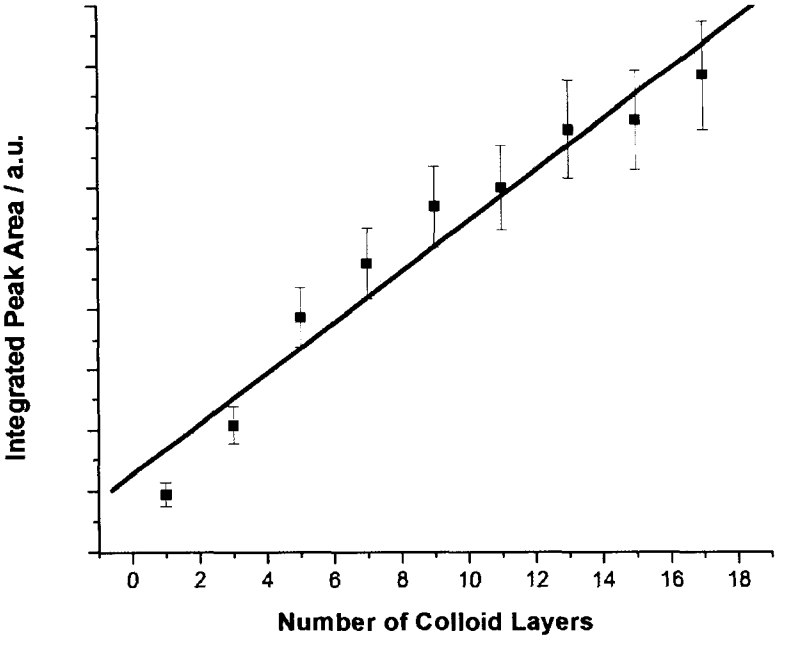


**Figure 4-12: Integrated peak area of localized surface plasmon band with increasing deposition of colloid layers. Based on replicate data, uncertainties are estimated to be ±10%.**

As expected, there is a linear increase in the overall absorbance with increasing number of deposited layers of gold nanoparticles.

A shift in the wavelength of the plasmon absorption band provides information about the spacing distribution between the nanoparticles [6]. As demonstrated in Section 3.1.2, when colloids approach too closely to each other, aggregation occurs and this results in pronounced effects on the absorption spectrum. In particular, a decrease in the interparticle spacing, such as aggregation of the nanoparticles, results in the plasmon absorption band shifting to longer wavelengths.

In Figure 4-11, it can be seen that there is a pronounced shift in the plasmon maximum to longer wavelengths as additional nanoparticle layers are deposited. This indicates that aggregation is occurring within the colloid structure. Figure 4-13 shows a plot of the wavelength of maximum absorption versus the number of colloidal layers. There is initially a dramatic increase in the wavelength of maximum absorption, shifting from 595 nm for one colloidal layer to 655 nm for the 7-layered substrate. After this, the magnitude of the wavelength shift with increasing nanoparticle layers is substantially lower, due to the colloids reaching the minimum approachable distance between each other [10]. This behaviour is similar to that obtained by Li *et al.* [86].

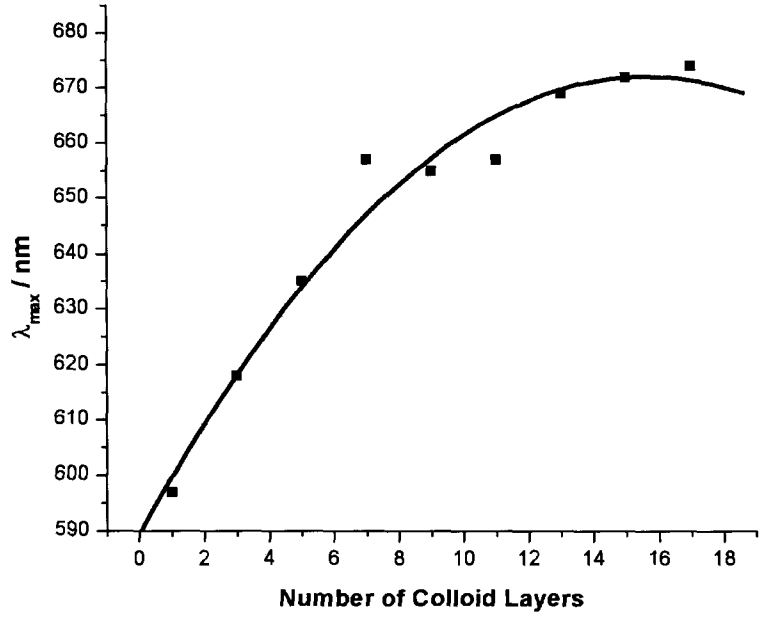


**Figure 4-13: Maximum wavelength of the absorption feature ($\lambda_{max}$) with increasing colloid layer depositions. The solid line is intended merely as an aid for the eye to demonstrate the overall trend.**

Further characterization of the aggregate structure must be done using an imaging technique such as AFM. The results of the AFM study are discussed in 4.3.2.

### 4.3.2 AFM characterization of multilayer structures

Surface roughness is a particularly important factor in the suitability of substrates for SERS [52-54]. One method for monitoring surface roughness is AFM [117].

Shown in Figure 4-14(a)-(h) are the topographic images and representative line scans for several of the coated-glass substrate used in this work, ranging from 3 nanoparticle layers through 17 layers of nanoparticles:

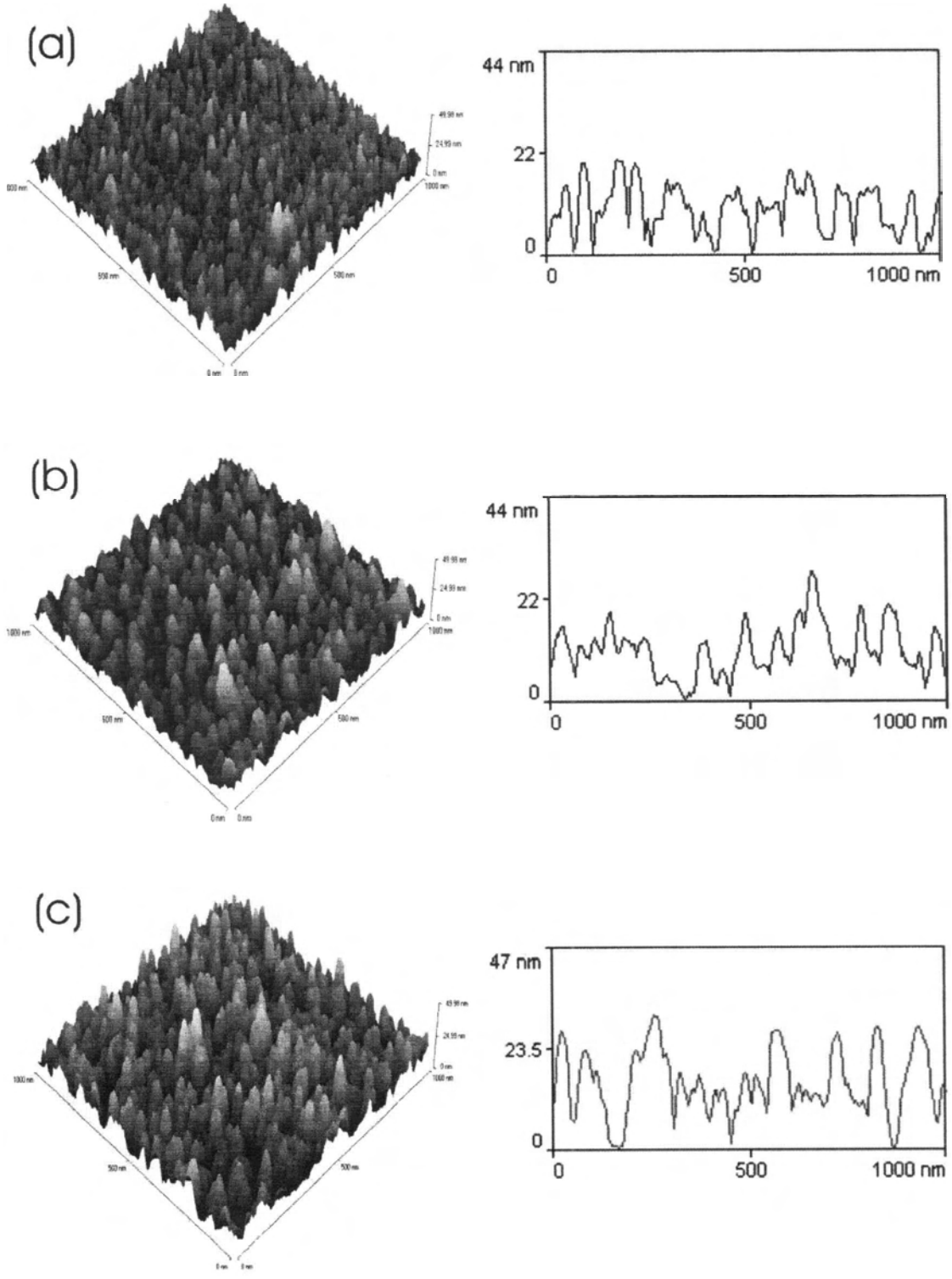
(a)
44 nm
22
0
0
500
1000 nm
(b)
44 nm
22
0
0
500
1000 nm
(c)
47 nm
23.5
0
0
500
1000 nm

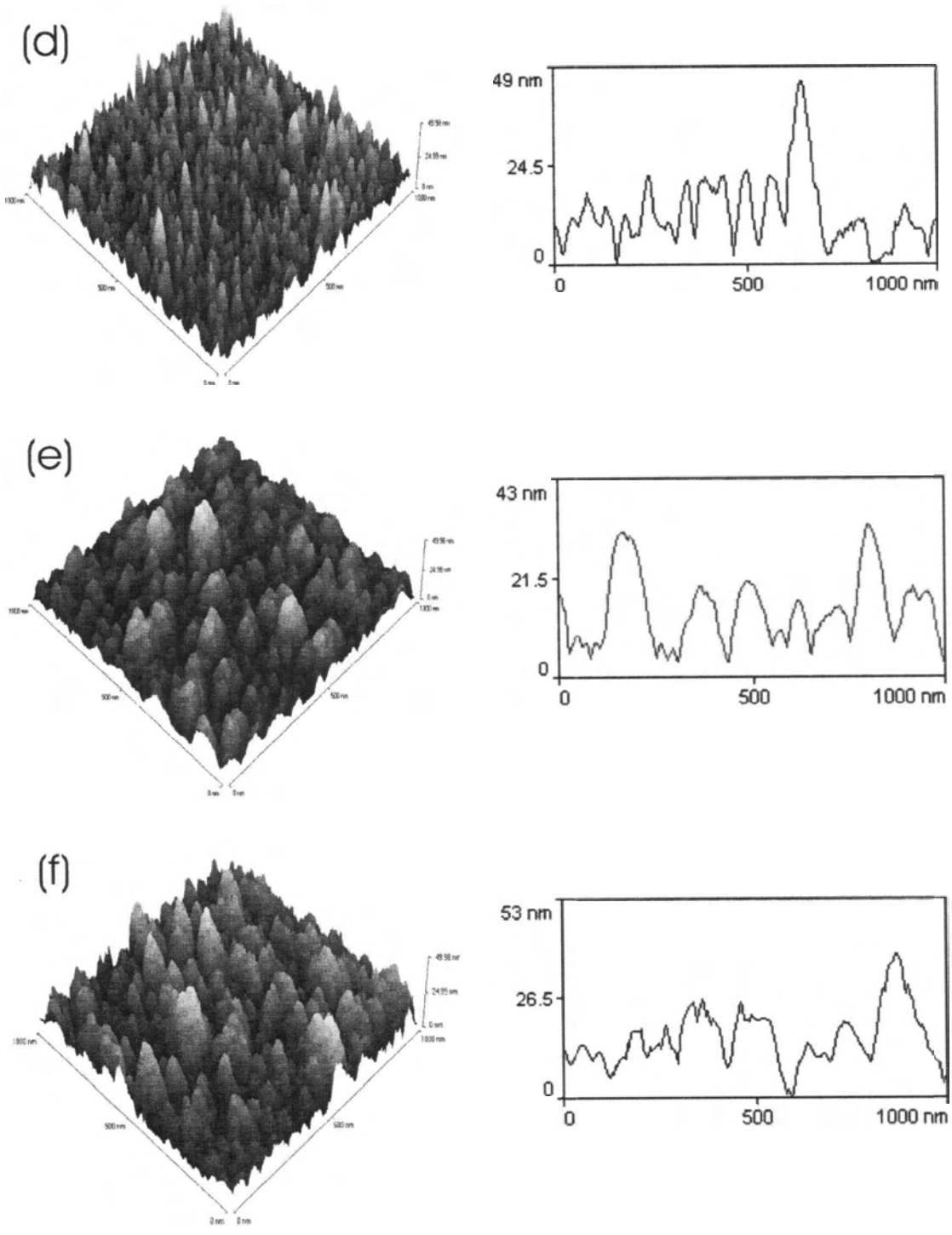
(d)
49 nm
24.5
0
0
500
1000 nm
(e)
43 nm
21.5
0
0
500
1000 nm
(f)
53 nm
26.5
0
0
500
1000 nm

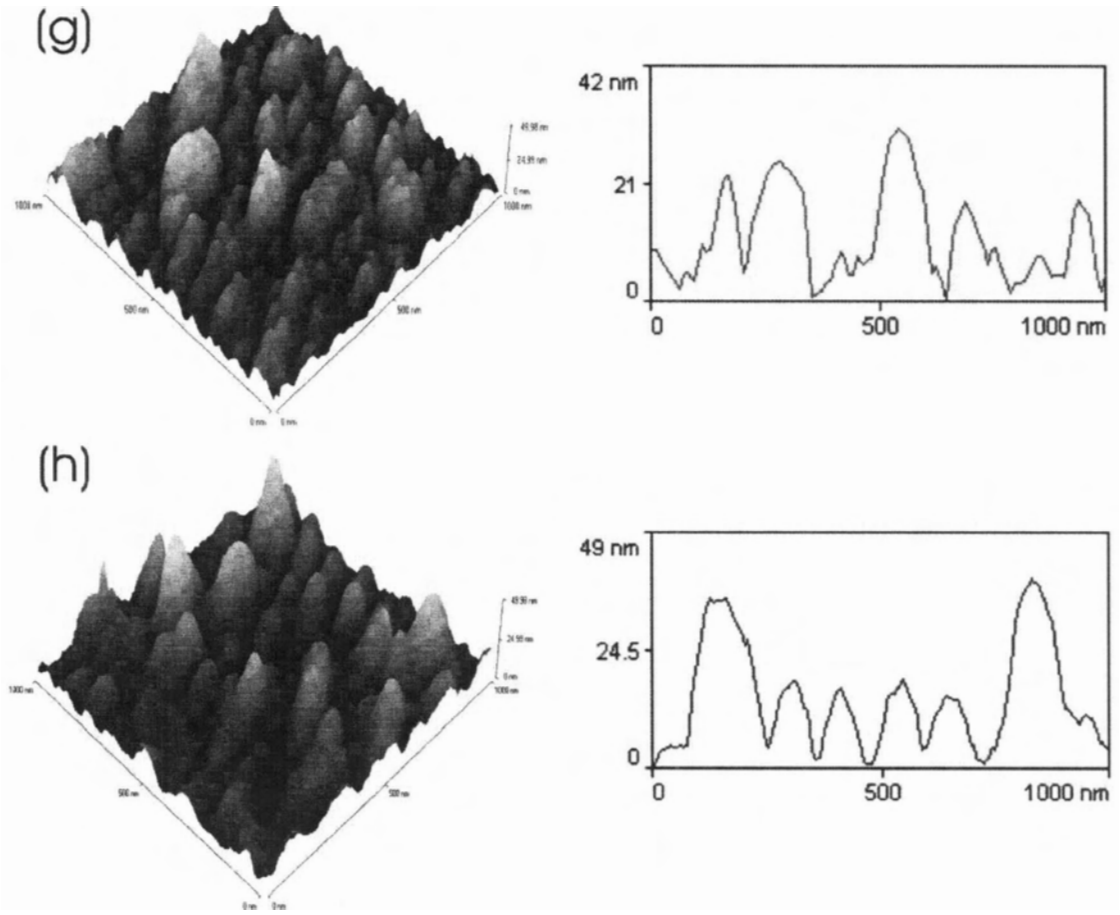


**Figure 4-14: AFM topographic images and representative line scans of substrates with increasing colloid depositions. (a) 3 layers (b) 5 layers (c) 7 layers (d) 9 layers (e) 11 layers (f) 13 layers (g) 15 layers (h) 17 layers.**

When examining the topography images in Figure 4-14, one can see that there is a substantial change in the overall morphology of the nanostructured substrates for different numbers of colloidal layers. For the 3-layer sample (Figure 4-14(a)), there are sharp, well-defined features from the imaging of individual nanoparticles. These features are on the order of 20 nm in height, which is too small to represent the span from

the glass surface to the top of the third nanoparticle layer. Instead, it seems likely that the AFM is predominantly imaging the top most nanoparticle layer of the nanostructure, but also some of the underlying structure below the top-most layer. This is consistent with other literature reports, in which a spaghetti-like structure was observed, and the AFM imaged not only the top-most layer, but also some of the underlying structure [89].

As more nanoparticle layers are deposited, there is a transition to large, mountainous-like peaks within the structure. In particular, as one approaches 11 nanoparticle layers (Figure 4-14(e)) these mountain-like structures becomes predominant. The size and span of these structures continues to increase with increasing number of nanoparticle layers.

The ability to fine-tune the overall substrate morphology based on the number of nanoparticle layer depositions makes this technique particularly interesting for use in SERS. The underlying roughness can be tuned until the substrate yields the maximum enhancement factor through the SERS mechanism.

#### 4.3.2.1 Characterization of surface features using fractal dimensions

One quantitative method to characterize the size and dimensions of features on the substrate surface is to analyze the fractal dimension of the substrate [79-81, 119]. The line profile obtained in the AFM image is overlaid with a uniform grid of span $b$. A count is made of the "non-empty" boxes ($N$) for which any portion of the profile falls within the box. Then the box size is divided in half, and the count is repeated. The box division process continues until the box size is on the order of the pixel size. The count

vs. box size is plotted on a log scale. The slope of this plot thus represents the fractal dimension ($R_f$), as given by:

$$N \propto b^{-R_f} \tag{21}$$

The dependence of fractal dimension with nanoparticle layers is shown in Figure 4-15:

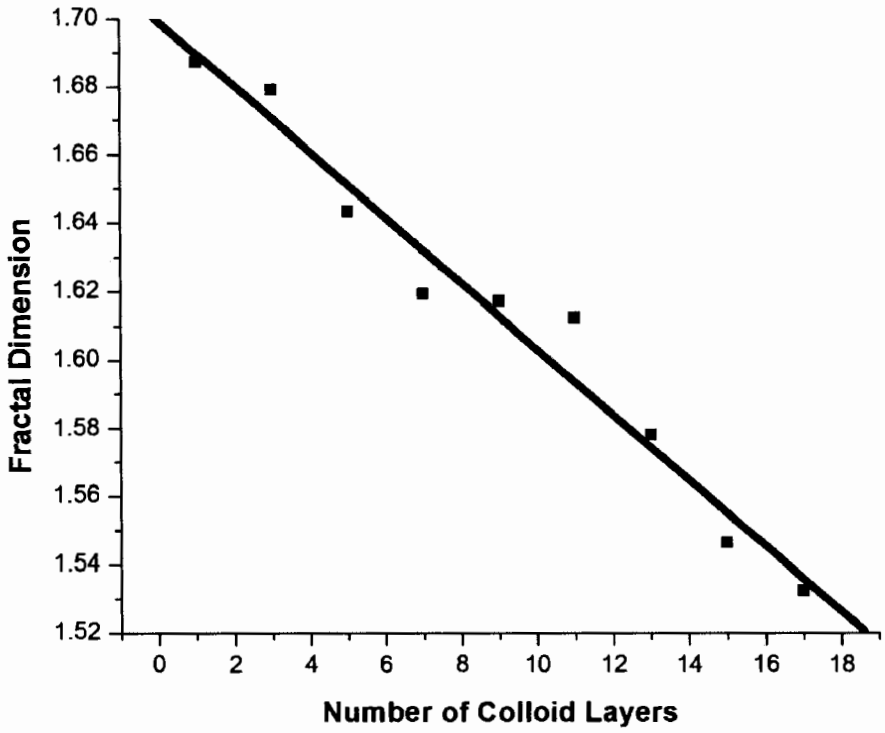


**Figure 4-15: Magnitude of the fractal dimension ($R_f$) with increasing number of nanoparticle depositions. The fractal dimension decreases as more layers are added.**

Surfaces which possess sharp, well-defined surface features have a higher fractal dimension than surfaces that have smooth, large-spanning features [79, 80, 119]. Indeed, when comparing the topographic images in Figure 4-14, one can see that there is such a transition from sharp, minor peaks to large, mountainous features. This change in topography will result in a decrease in the fractal dimensions. The surface topography was briefly discussed in 4.3.2.

#### 4.3.2.2 Bearing ratio analysis of nanoparticle structures

A bearing ratio analysis can provide information about the surface roughness and the features on the surface with nanoparticle multilayers [113]. The bearing ratio determines the total percentage of data that exists at different levels above the sample surface. The bearing ratio is given by:

$$\text{Bearing Ratio} = \frac{(\text{Data above z - height})}{(\text{Total data})} \times 100\% \tag{22}$$

A bearing ratio plot consists of the $z$-height on the x-axis, and the corresponding bearing ratio on the y-axis. Initially the $z$-height will be 0 nm above the surface, and the amount of data above this $z$-height will be 100% (All data will be above this lowest level). As the $z$-height increases from this point, the amount of data above this height will correspondingly decrease until no data is above the $z$-height (Which corresponds to the maximum height of the AFM image). A bearing ratio plot essentially consists of a sigmoidal curve in which there are two nearly-flat regions of little change in bearing ratio

at the minimum and maximum *z*-height values. There is also a transition region between these two points. A hypothetical bearing ratio plot is shown in Figure 4-16:

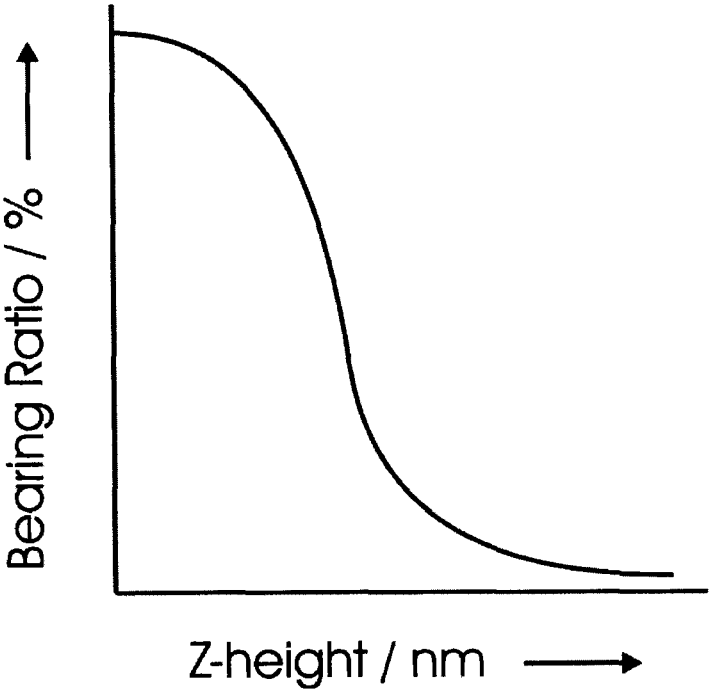


**Figure 4-16: Hypothetical bearing ratio plot. Note the two nearly-flat regions at 0 and 100% bearing ratio. There is also a transition region between the two.**

The length of the two flat regions, as well as the transition region, provides information as to the overall surface features and morphology.

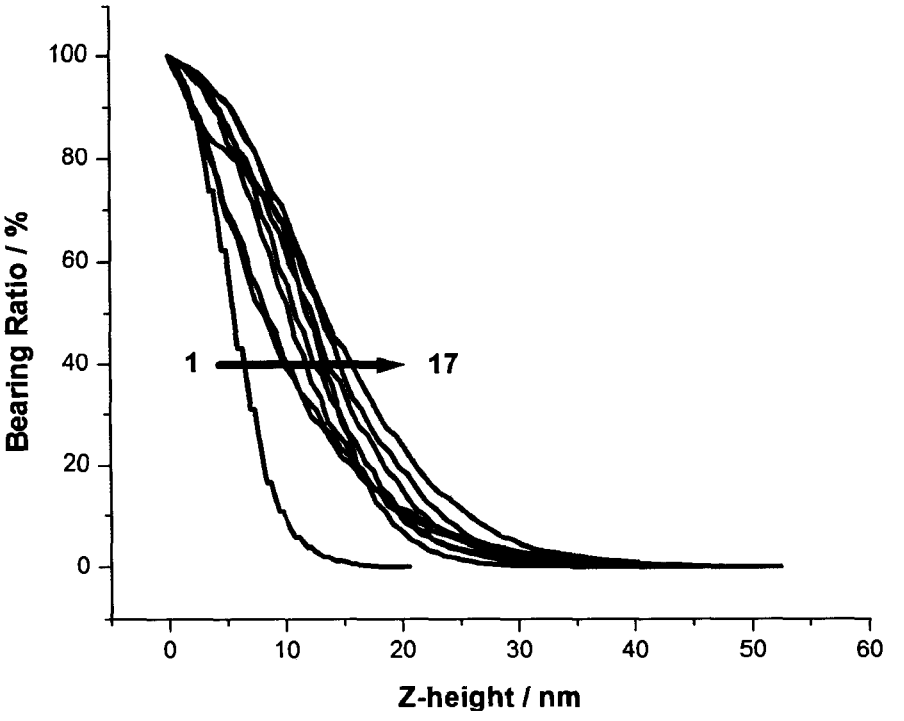


**Figure 4-17: Bearing ratio plot for nanoparticle substrates.**

As can be seen from Figure 4-17, there is a sigmoidal nature to the bearing ratio plot obtained from colloids deposited onto glass. Also of note is the fact that the length of the first plateau region increases as increasing layers of nanoparticles are deposited. This is due to the fact that the overall *z*-height of the images is increasing with increasing number of nanoparticle layers: In essence, the bearing ratio plot is being "Stretched" along the x-axis with increasing number of layers. As a consequence, the location of the transition region will also move to greater *z*-heights.

#### 4.3.2.3 Surface area changes

For a 1000 x 1000 nm scan, the projected surface area is $1x10^6$ $nm^2$. When protrusions or other features exist on the surface, this has a net result of increasing the actual surface area. An example of a flat and rough surface is shown below:

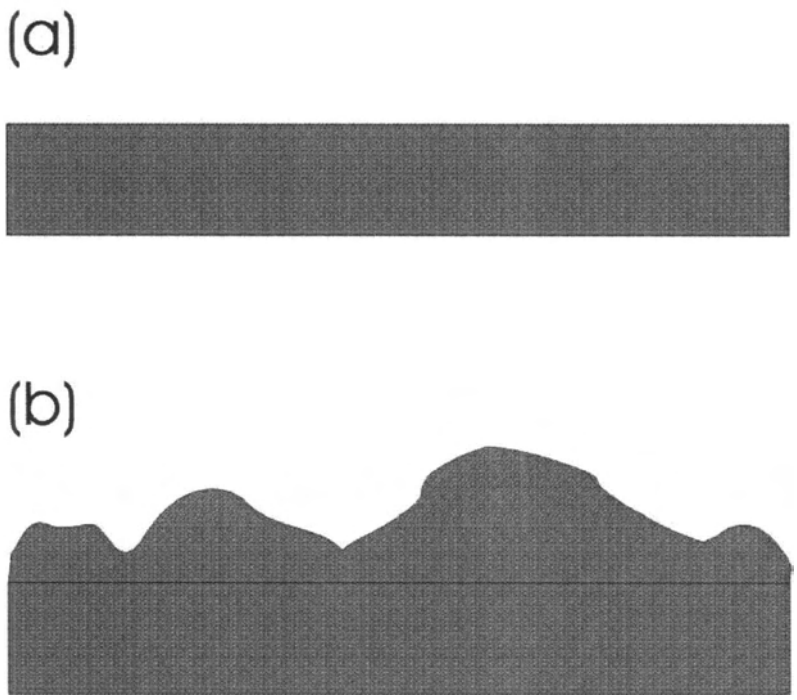


**Figure 4-18: Example picture showing the change in surface area with a change in surface geometry: (a) Smooth, flat surface. (b) Roughened surface.**

In the above example, the roughened surface will have a greater surface area than the smooth, flat surface. The change in surface area, as calculated by the AFM software, with increasing number of nanoparticle layers is shown in Figure 4-19.

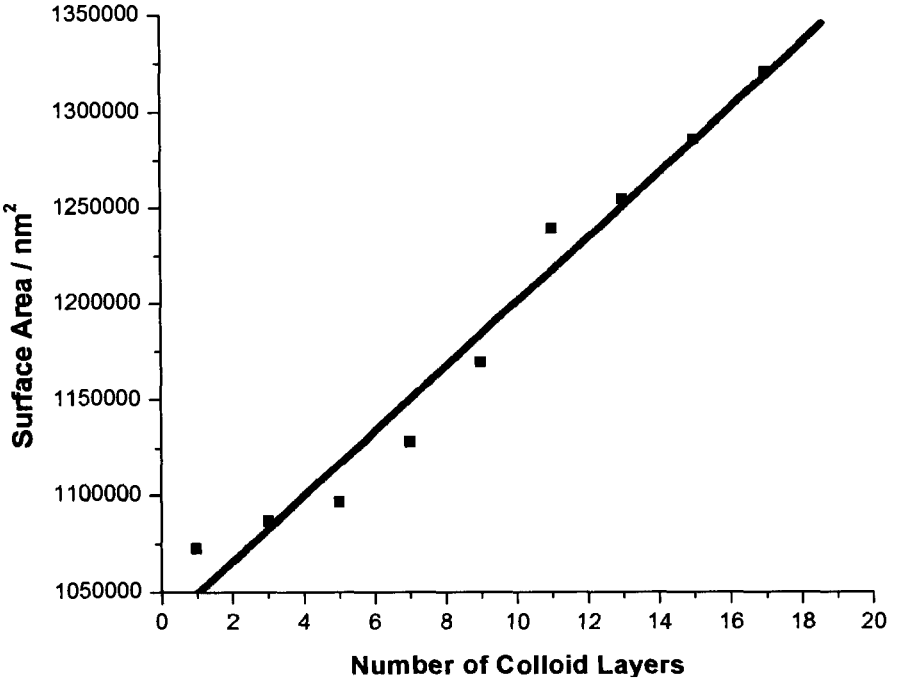


**Figure 4-19: Increase in surface area with increasing number of nanoparticle depositions.**

The change in surface area can also affect the subsequent SERS signal. The greater the surface area, the greater amount of area for analyte molecules to be deposited. The greater number of analyte molecules should then result in a greater SERS signal.

#### 4.3.2.4 Increase in surface feature size

One other parameter that is particularly important to correlate to the SERS response is the size of the features of the underlying substrate [55, 120-122]. Here, the AFM software was used to obtain the span of surface features. The feature size was corrected for tip-sample convolution using Equation (20).

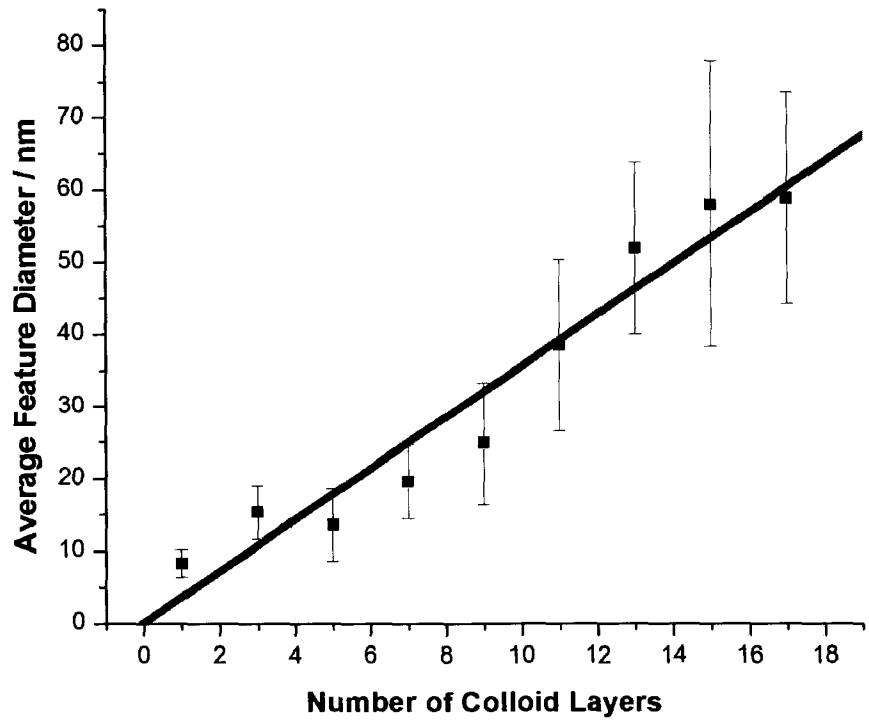


**Figure 4-20: Increase in average feature size with increasing number of colloid depositions. The error bars represent the standard deviation from multiple measurements.**

As can be seen from Figure 4-20, the diameter of the surface features increases linearly with increasing colloid depositions. As demonstrated in Figure 4-14, the height of the surface features remains relatively constant with increasing number of layers, but the span of the features increases dramatically. This suggests that the underlayers of the substrate undergo a reorganization to form these cone-shaped structures. Such reorganization has been observed before by Musick *et al.* [89].

# Chapter Five: Colloidal Nanostructures as a Substrate in Surface-enhanced Raman Scattering (SERS)

In this chapter, the multilayer nanoparticle substrates are examined for their suitability as substrates for surface-enhanced Raman scattering (SERS). The SERS signal is then correlated with the surface morphology information obtained in the previous chapter.

## 5.1 Oxazine-720: An Introduction

Oxazine 720 (alternatively called oxazine 170 or oxazine) is a laser dye that was selected as the Raman analyte for the work performed here. Oxazine was chosen because of its large scattering cross section and its previous use by the Brolo research group in other Raman-based studies [83, 123-125]. Oxazine (and its derivatives) present reversible electrochemical behaviour at metallic [126] and semiconducting [127] surfaces. This and other physical-chemical properties, including it's strong absorption band in the visible region, could potentially make it useful for applications in other fields, such as electrocatalysis [128] and energy conversion [129].

Oxazine belongs to a class of laser dyes that contains the phenoxazine moiety and its chemical structure is presented in Figure 5-1. Other laser dyes in this class include the popular cresyl violet and nile red [130, 131]. The extended conjugation network in the phenoxazine ring is responsible for the strong absorption band in the visible spectrum [130, 132].

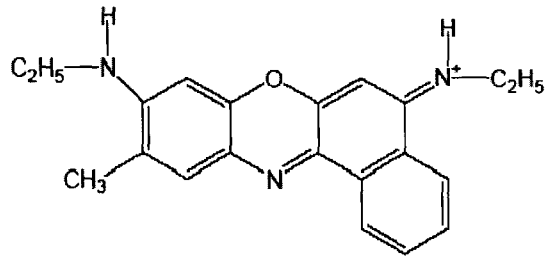


**Figure 5-1: Chemical structure of Oxazine.**

Shown in Figure 5-2 is the UV-Vis spectrum of oxazine in methanol. Note the pronounced absorption feature centered around 620 nm. As with most laser dyes, the molar absorptivity of oxazine is incredibly high – on the order of 83,000 $M^{-1}$ $cm^{-1}$ in methanol at its absorption maximum near 620 nm [133].

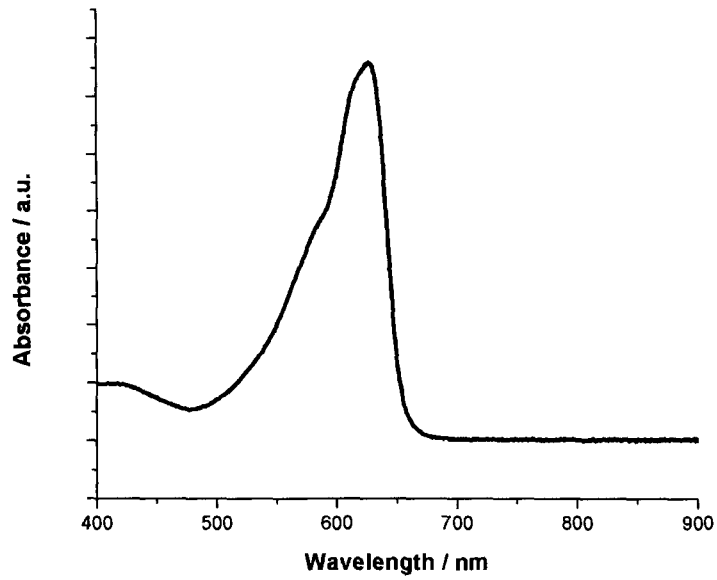


**Figure 5-2: UV-Vis spectrum of oxazine in methanol.**

Unless otherwise stated, the Raman excitation used in this work was 785 nm. As can be seen from Figure 5-2, there is no appreciable absorption by oxazine at this excitation wavelength. Therefore, this wavelength is sufficiently away from the visible-absorption maximum that any additional molecular resonant excitation which would lead to surface-enhanced resonant Raman scattering (SERRS), is avoided [53].

Shown in Figure 5-3 is the Raman spectrum of solid oxazine. This spectrum was obtained using green (514.5 nm) excitation, because the Raman spectrum of solid oxazine using 785 nm excitation did not yield any observable bands.

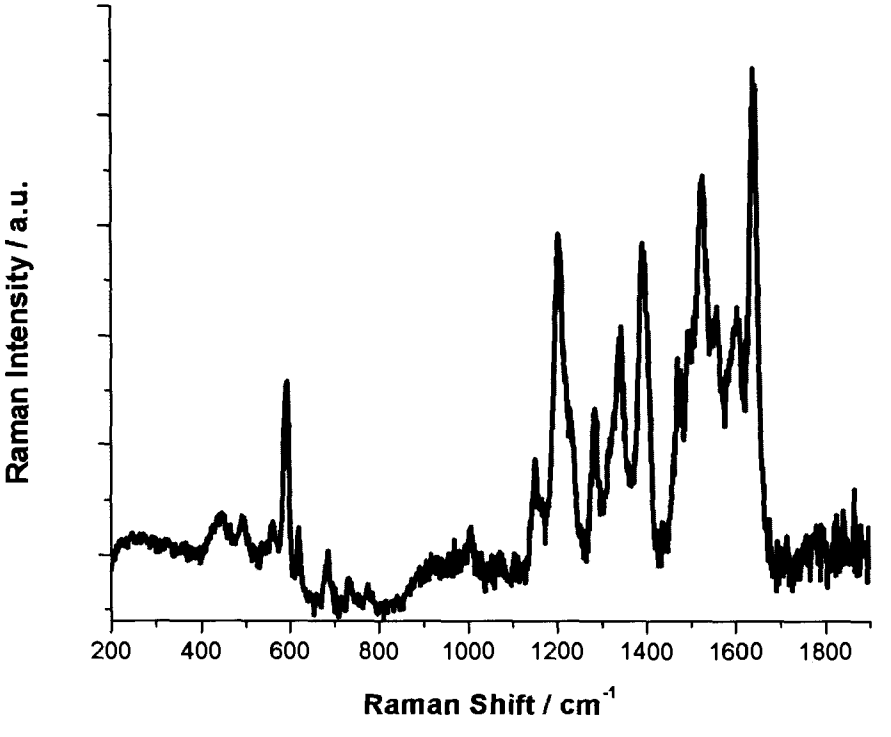


**Figure 5-3: Raman spectrum of powdered Oxazine-720. Spectrum obtained using 514.5 nm excitation. Acquisition parameters are as described in Section 2.9.3.**

There are two regions in Figure 5-3 which contain a significant amount of vibrational information: One region is between 400-700cm$^{-1}$, and another is between 1100-1700 cm$^{-1}$. The strongest observable transition in the lower energy region occurs at 591 cm$^{-1}$, and it is assigned to a ring deformation mode [123]. This is the result of the symmetric stretching of the nitrogen and oxygen atoms of the phenoxazine ring moiety.

Several drops of a methanolic solution of oxazine was deposited onto a smooth gold surface, rinsed with water, and the Raman spectrum at 785 nm was attempted. No obvious Raman transitions were observed. This is not surprising, given the fact that even the spectrum of solid oxazine could not be obtained using the same excitation wavelength (785 nm). Two extra factors would make it more difficult to obtain the Raman spectrum of a monolayer when compared to the solid. The first one is analyte concentration: The concentration of an oxazine monolayer on the gold surface is extremely small, and the Raman signal is dependent upon the concentration of the analyte species [53]. In addition, the smooth gold surface is only very weakly enhancing (by a factor of 10) [82]. The combination of the extremely small concentration and the weakly enhancing surface make observation of the signal onerous.

## 5.2 Change in SERS response with number of nanoparticle layers

To characterize the substrates for their suitability in SERS, a Raman-active analyte molecule must be deposited on to the surface of the substrate [52-54, 61]. This was accomplished by covering the surface of the nanoparticle substrates with a 10 μM

solution of oxazine in methanol. The methanol was allowed to evaporate, leaving a film of oxazine deposited on the surface. To remove the excess of unbound oxazine, the substrate was rinsed with copious amounts of water. The net result was a monolayer of oxazine deposited on to the colloid surface [123].

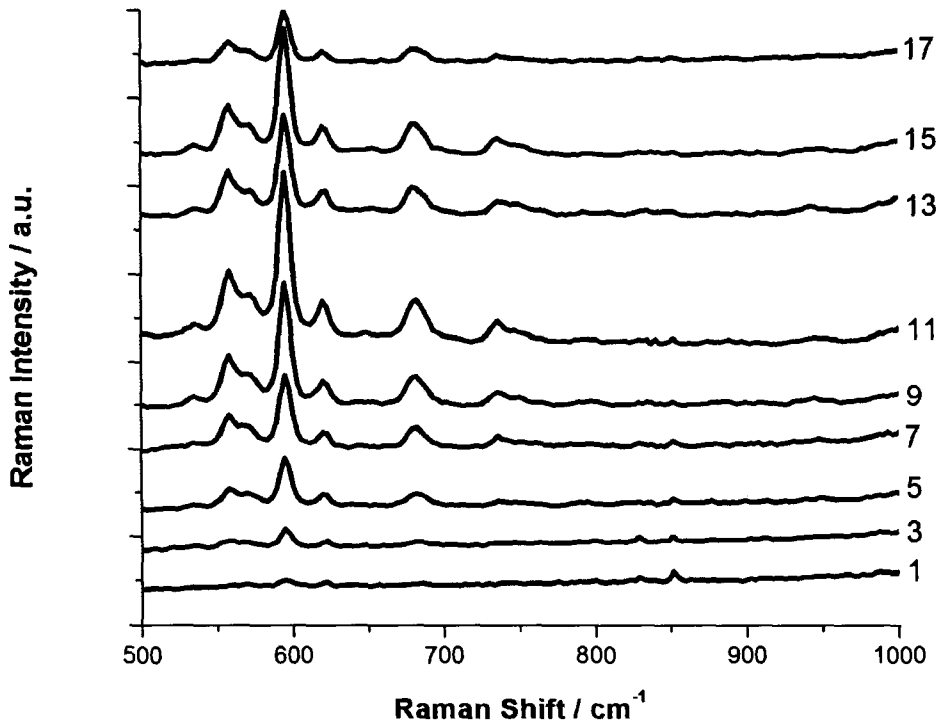


**Figure 5-4: SERS spectra of Oxazine-720 deposited on gold nanoparticle substrates. The number of deposited nanoparticle layers corresponding to each spectrum is noted to the right of each spectrum. The spectra have been offset to allow for easier comparison. Acquisition parameters are as described in Section 2.9.1.**

The SERS signal, obtained at 785 nm excitation, in the 500-1000 $cm^{-1}$ region for oxazine deposited onto the nanoparticle substrates is shown in Figure 5-4. Initially, the one-colloid layer substrate yields Raman-active stretches near 591 $cm^{-1}$, 625 $cm^{-1}$ and 850 $cm^{-1}$ that are just barely visible above the baseline noise. However, the fact that these signals are even visible indicates that this substrate is much more enhancing than a vapour-deposited smooth gold surface.

With increasing number of nanoparticle layers deposited, there is an increase in the overall intensity of the Raman stretches, and the appearance of additional Raman bands near 550, 675 and 740 $cm^{-1}$. A maximum is reached, and subsequent nanoparticle depositions results in a decrease in the Raman signal. It is important to note that no significant changes in the relative intensities between bands were observed for any of the substrates studied.

To quantify the change in Raman intensity, the area of the 591 $cm^{-1}$ band was obtained through integration, and was plotted as a function of number of colloid layers (Figure 5-5). Typically the error in the SERS intensities are estimated to be between 10 to 20 %.

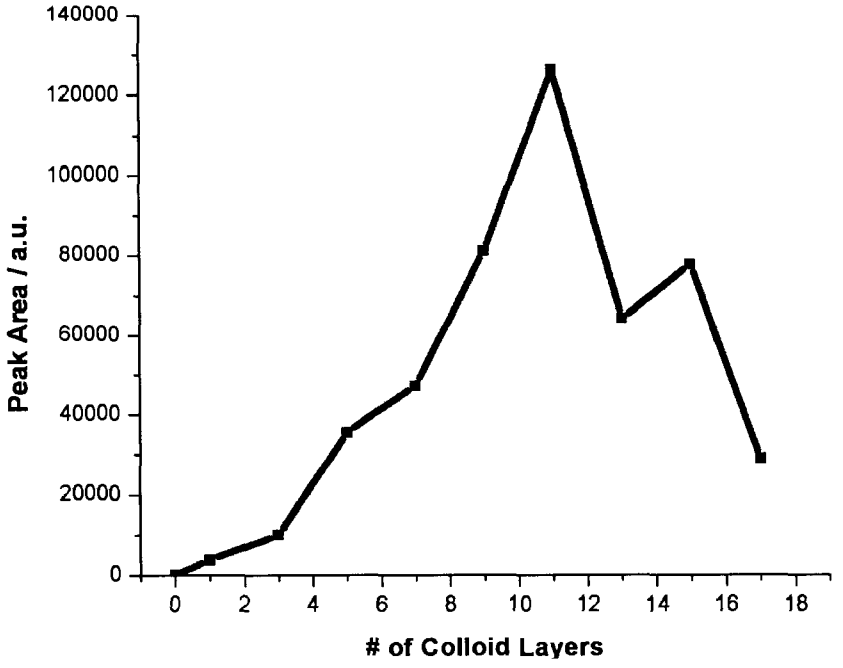


**Figure 5-5: Integrated peak area of the 591 cm-1 stretch of Oxazine with increasing number of nanoparticle layers.**

From Figure 5-5 it can be seen that there is initially a dramatic increase in the peak area of the 591 $cm^{-1}$ stretch from 1 to 11 colloid layers. The peak area reaches a maximum for the 11 nanoparticle layer substrate, and subsequently decreases between 13 and 17 layers. Therefore, the substrate containing 11 colloid layers is the most suitable SERS substrate for 785 nm excitation.

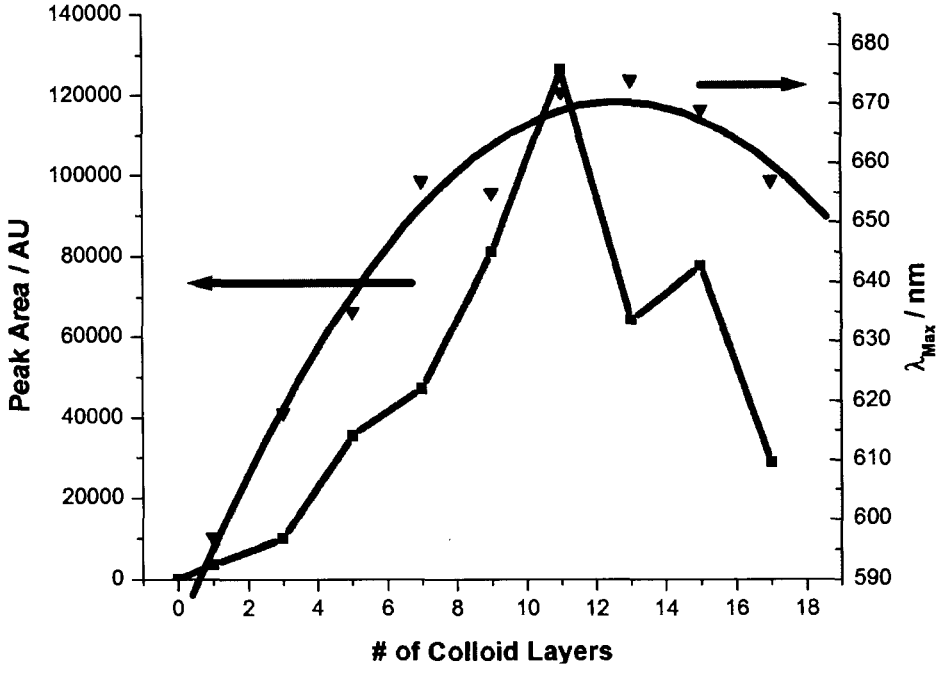


**Figure 5-6: Peak area of the 591 $cm^{-1}$ SERS stretch of oxazine (squares – left axis), and the wavelength of absorption maximum (triangles – right axis) for the nanoparticle multilayer substrates.**

Shown in Figure 5-6 is the dependence of the SERS signal for the 591 $cm^{-1}$ oxazine stretch with increasing number of colloid layers, and the absorption maximum of the underlying nanoparticle multilayer substrate. It is important to note that the absorption maximum of the nanoparticle multilayer substrates does not exceed the excitation wavelength used for the Raman experiments (785 nm). Previous studies by Olson et al [113] have shown that the SERS intensity decreases dramatically when the plasmon maximum is at longer wavelengths than the excitation source: because the SP cannot be excited, SERS enhancement will decrease.

Despite the fact that the plasmon maximum does not coincide with the excitation wavelength, a decrease in the Raman signal was observed for 13-17 colloid layers. This trend was also observed by Olson et al for 32 nm silane-derivatized colloids that were assembled into a multilayer substrate [113].

To further demonstrate this point, Figure 5-7 shows the increase in absorbance for the multilayer substrates at the excitation wavelength, along with the SERS peak area for the 591 $cm^{-1}$ stretch. Note that the absorbance continually increases – suggesting further SP excitation, yet for 13-17 layers the Raman signal decreases.

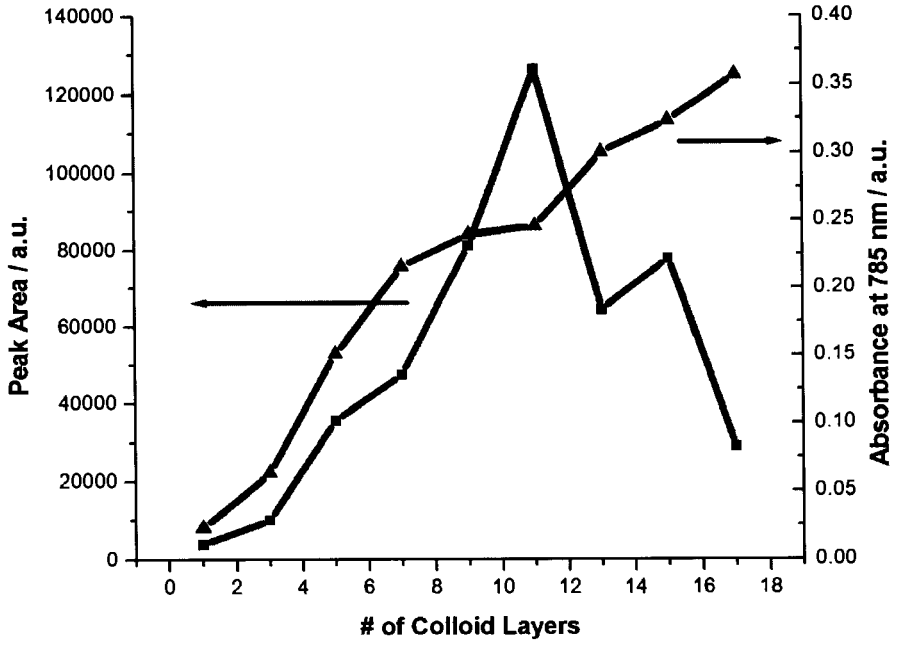


**Figure 5-7: SERS peak area of the 591 $cm^{-1}$ stretch (squares - left axis) and absorbance of the substrate at 785 nm (triangles - right axis) with increasing number of colloid layers.**

## 5.3 Correlation of SERS enhancement with surface morphology

The dramatic increase in the Raman signal must be due to a change in surface morphology of the underlying SERS substrates [80, 85, 121]. The correlation between the surface morphology and the Raman intensity is discussed here.

### 5.3.1 Surface area dependence

One possibility to account for an increase in the Raman intensity is due to a change in the surface area of the substrate [53, 134]. With increasing surface area, more analyte molecules would be deposited and thus an increase in Raman intensity would be expected.

Shown in Figure 5-8 is the comparison between the relative change in surface area calculated from the AFM pictures and the intensity of the oxazine 591 $cm^{-1}$ stretch. Note that the relative change in surface area is only on the order of 30%. In comparison, the SERS peak area sees an increase in intensity of 3200% for the 11 nanoparticle layer sample relative to the 1 nanoparticle layer sample. Furthermore, note that the SERS response reaches a maximum at 11 colloid layers and decreases after this point. On the other hand, the surface area continually increases with increasing number of colloid layers.

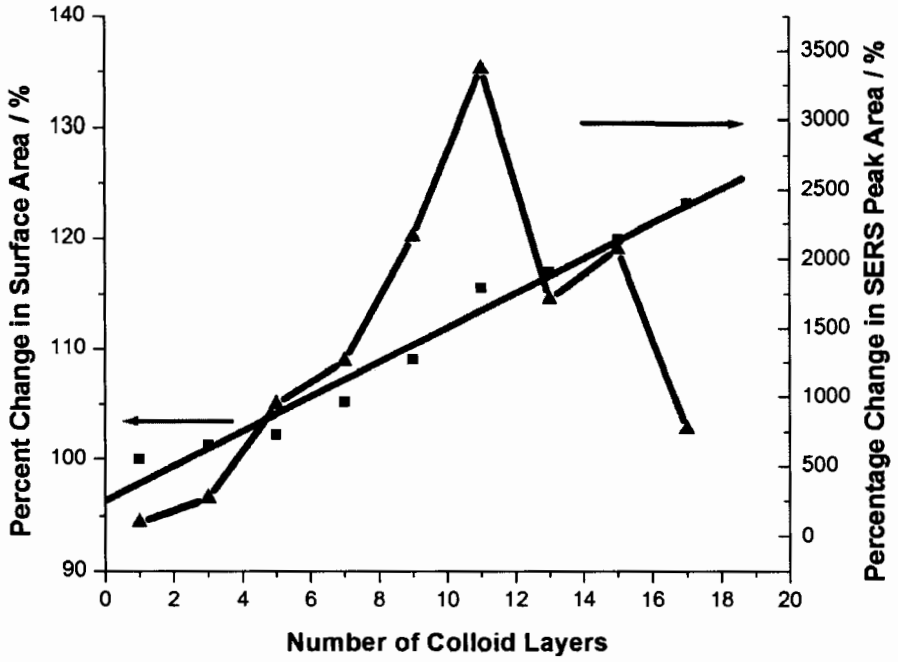


**Figure 5-8: Percentage change in SERS signal of the 591 $cm^{-1}$ oxazine stretch (triangles – right axis) and percentage change in surface area (squares – left axis) with increasing number of nanoparticle layers.**

Reports by Pignataro et al. have demonstrated that the observed SERS signal is a linear function of the micromorphology in terms of the surface roughness for silver substrates [118]. In particular, the surface roughness was represented by the effective surface area (ESA) parameter, which is defined as:

$$ESA = \frac{S_{3D} - S_{2D}}{S_{2D}} \times 100 \qquad (23)$$

Where $S_{3D}$ is the real three-dimension surface area, while $S_{2D}$ is the scanned twodimensional area. In this work, 1000x1000nm scans were used, leading to a bidimensional area of 1,000,000 $nm^2$.

The effective surface area and SERS intensity of the 591 $cm^{-1}$ band were correlated, and the results are presented in Figure 5-9. Note that there is indeed a linear relationship between ESA and SERS intensity for part of the data set, as predicted by Pignataro [118]. However, this relationship fails when the ESA is 25% or greater (which corresponds to 13 colloid layers).

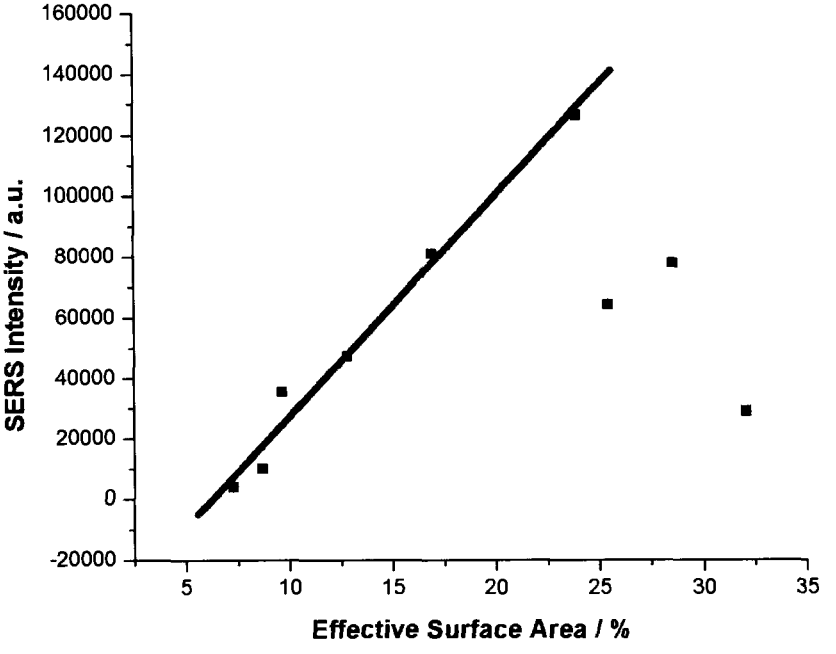


**Figure 5-9: SERS intensity with increasing effective surface area. The best-fit line demonstrates the region of linear correlation, as demonstrated by Pignataro [118].**

The work of Pignataro showed a linear relationship up to effective surface areas of 60% [118], yet here values greater than 25% result in the relationship failing. There are two possible reasons that could account for this discrepancy. First of all, the work published by Pignataro utilized silver surfaces which were obtained by plasma oxidation-reduction cycles onto originally flat silver surfaces [118]. Here, the work involved the deposition of colloidal gold, which is inherently spherical in shape. The second reason is a direct corollary of the first: Pignataro made no correlation with the underlying morphological shape of the surface features, but merely concerned himself with the surface area [118]. In fact, in the AFM images published by Pignataro the surface features are shaped more like oblate hemispheroids instead of the cone-like shapes obtained in this work.

### 5.3.2 Dependence on RMS roughness

Previous studies by Muniz-Miranda et al. suggested that the square of the RMS roughness is proportional to the electromagnetic enhancement, and hence proportional to the SERS signal [82]. Shown in Figure 5-10 is a comparison of the SERS signal with the $RMS^2$ roughness of the underlying substrate.

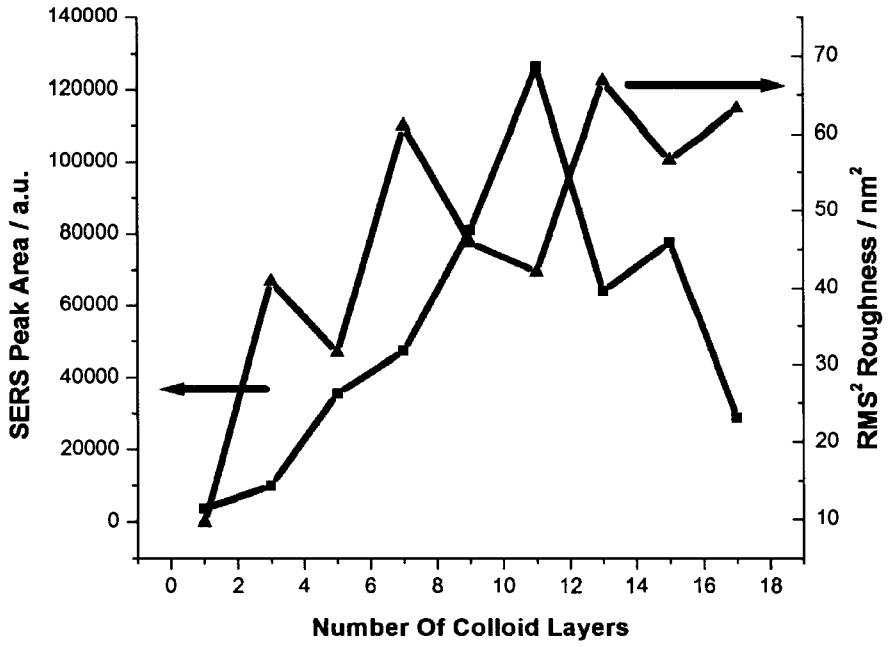


**Figure 5-10: Integrated peak area of 591 $cm^{-1}$ SERS stretch (squares – left axis) and substrate $RMS^2$ roughness (triangles – right axis) with increasing number of colloid layers.**

The fact that these two quantities show very little correlation is not surprising, given the fact that the RMS roughness remained relatively constant after approximately 7 nanoparticle layers, yet the SERS response varied by a large margin.

One possible reason for the discrepancy between the work of Muniz-Miranda and the work here could be due to the inherent difference of the experiments. Muniz-Miranda studied the deposition of silver on to filters, and the SERS response of an analyte molecule on the silver deposits was measured [82].

It is also important to note that Muniz-Miranda did not perform a rigorous correlation of their SERS data with the $RMS^2$ parameter, instead, only one paragraph was devoted to mentioning this potential relationship, but no evidence was provided to support the statement [82]. The results obtained here could tentatively indicate that further work may be required in order to prove that the relationship is valid.

### 5.3.3 Dependence on the fractal dimension of the substrates

A number of research groups have utilized the fractal dimension of cold-deposited silver substrates to correlate with the observed SERS enhancement [54, 76, 79-81, 119, 135, 136].

Here, the fractal dimension of representative line scans of the nanoparticle substrates was obtained, and this is compared with the SERS data in Figure 5-11. Note the fractal dimension continually decreases while the SERS response varies irrespective of the fractal dimension.

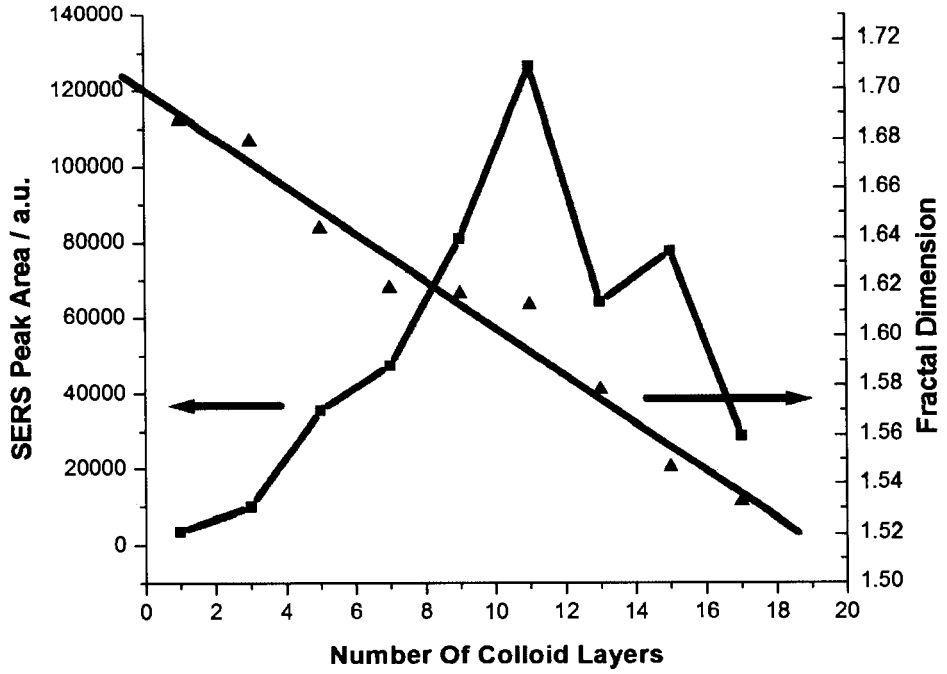


**Figure 5-11: Integrated peak area of 591 $cm^{-1}$ SERS stretch (squares – left axis) and substrate fractal dimension (triangles – right axis) with increasing number of colloid layers.**

Previous research results by Douketis et al. have shown that cold vapour deposited silver substrates exhibit fractal-like character [79, 80, 119]. In general, structures deposited at lower temperatures yielded higher SERS enhancement because of an increased surface roughness and hence fractal dimension. More importantly, the microstructure of the substrates collapse when the temperature is increased to those near room temperature due to surface diffusion, resulting in a decreased SERS enhancement.

Mountain-like structures, like those observed here, have been described as being fractal-like [54]. However, the results obtained here indicate a decreasing fractal dimension, yet

an increasing SERS enhancement. This suggests that the fractal dimension is not a parameter of sufficient quality to correlate or explain the SERS enhancement observed here.

### 5.3.4 Change in average feature sizes

As has been demonstrated above, none of the morphological parameters examined are suitable to describe the SERS enhancement obtained here. It was also shown that the increase in Raman signal cannot be attributed to an increase in surface area alone. Instead, the change in intensity must be due to a fundamental change in the surface morphology that leads to the SERS phenomenon. One possible parameter is to examine the average size of features on the Raman substrate with increasing number of nanoparticle layers.

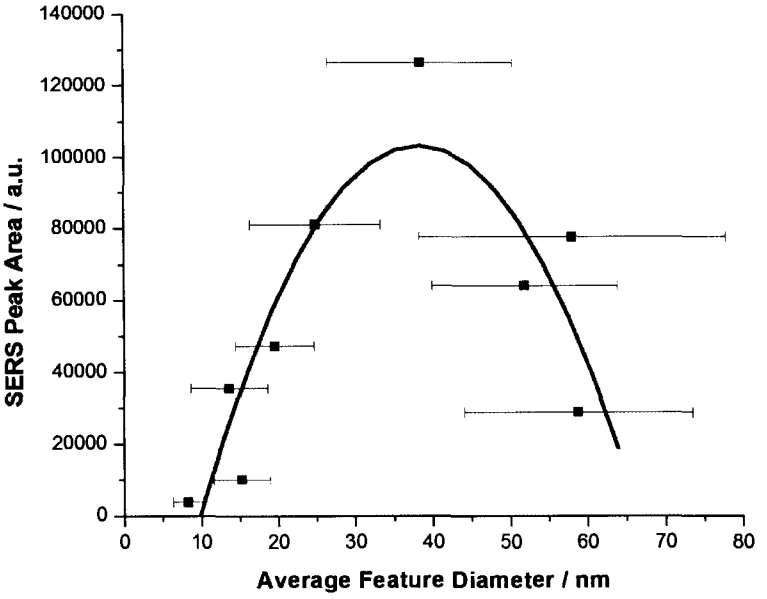


**Figure 5-12: Change in SERS signal as a function of average feature size. The line is intended solely as a guide for the eye to demonstrate the overall trend.**

Plotted in Figure 5-12 is the resultant SERS peak area for the oxazine 591 $cm^{-1}$ stretch as a function of the average feature size of the underlying multilayer substrate. From the data shown above, it can be seen that the maximum SERS intensity is obtained when the average feature size is on the order of 40 nm.

SERS enhancement is strongly dependent upon the metal used, excitation wavelength, and the underlying shape of the substrate [54]. Previous studies have shown that the largest SERS enhancement occurs for surfaces with a features in the 10-100 nm regime [8, 54]. In particular, Jana [137] has shown that gold features 20-50 nm in size result in the greatest SERS enhancement. The results obtained here agree well with these previous results.

# Chapter Six: Second Harmonic Generation Measurements of Colloidal Nanostructures

In this chapter, the NLO properties of the multilayer nanoparticle substrates are examined using SHG. The SHG signal is then correlated with a variety of morphological parameters.

## 6.1 Second Harmonic Generation from Colloidal Nanostructures

The measurement of the NLO properties of the colloidal nanostructures provides welcome complementary information to that obtained from the SERS study. SERS and surface SHG (SSHG) are in fact linked to some degree [70-72, 138, 139]. SERS is dependent upon electromagnetic and chemical enhancement mechanisms, but the major drawback to SERS and other spectroscopic techniques is that the magnitude of each of the two enhancements is not resolvable. SSHG, on the other hand, allows direct quantification of the electromagnetic nature of local field enhancements [71, 72, 140, 141].

To measure the second harmonic (SH) signal, the colloidal nanostructure was irradiated with short, high intensity pulses of 820 nm light as described in Section 2.8. When interacting with the metal-air interface, a very small number of those pulses undergo a frequency doubling to emit second-harmonic light at 410 nm.

The SH signal can be produced from two different sources: from the bulk material and from the surface (interface) [141]. The contribution to the overall susceptibility, $\chi^{(2)}$, can be represented by:

$$\chi^{(2)} = \chi_S^{(2)} + \chi_B^{(2)} \tag{24}$$

Where $\chi_S^{(2)}$ represents the surface contribution and $\chi_B^{(2)}$ the bulk SH contribution.

The bulk contribution describes the generation of SH signal from a material with a non-zero second-order susceptibility. Within the interior of a centrosymmetric medium, the electric-dipole contribution will vanish, leaving only contributions from the higher-order magnetic and electric terms [141]. Here, the bulk contribution can be considered to be the result of an interaction between the pulsed laser and the whole nanoparticle to yield a SH signal.

On the other hand, SH can also be generated at an interface because the local symmetry is broken [140]. Poliakov *et al.* have shown in the type of structures where confinement of electromagnetic fields occurs, the surface contribution to the local enhancement is predominant [142]. This effect comes from oblate hemispheroids lying in a sample plane, which interact strongly with each other [143].

The substrates (colloidal nanostructures) were placed in the SH apparatus, and the intensity of the resultant SH signal was measured. The SH signal was then correlated to

the number of colloidal layers deposited on to the nanostructure substrate (Section 2.8). An increase in the SH signal will be due in part to the resonant excitation of the surface plasmons of the gold nanoparticles by the incoming electromagnetic field [70, 71]. As in the SERS mechanism, the excitation of the surface plasmons will increase the local electric field, which will result in a greater SH signal [71, 140, 141].

As can be seen from Figure 6-1, a one-layer substrate generates very little SH signal – on the order of 350 counts per second. A 3 layer substrate exhibits a much greater SH signal (near 10000 cps), but the addition of 5 to 11 colloid layers decreases the SH signal to the 1500-3000 cps range. Subsequently, the maximum SH signal is obtained for 13 colloid layers, with a SH signal of 19000 cps. Substrates consisting of 15 and 17 colloid layers obtain a SH signal of 6500 and 3500 cps, respectively. Based on multiple acquisitions from multiple samples and differing sample areas, the uncertainty in the SH measurements is estimated at approximately ±20% of the measured signal.

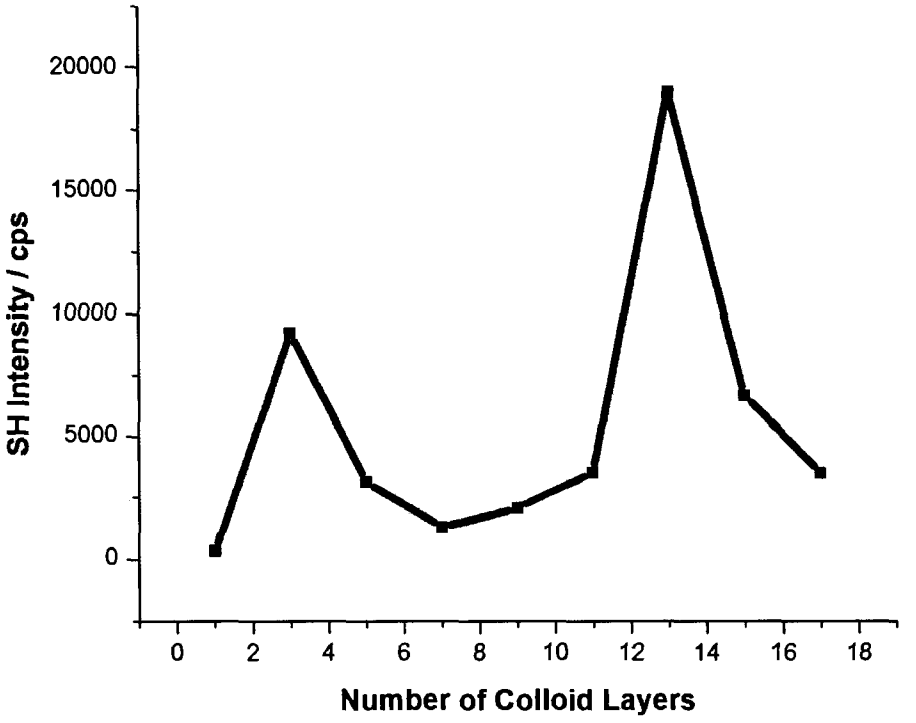


**Figure 6-1: Second Harmonic intensity with increasing number of nanoparticle layers.**

Examining the overall structure of Figure 6-1, there appears to be two resonances (occurring at 3 and 13 colloid layers) overlaid on top of an (approximately) linearly increasing baseline. Previously it has been shown that there is a metal-thickness dependence on the SH signal [72], and the linear increase in the background signal here is attributed to be from the same source. To verify this fact, various thicknesses of gold were deposited onto glass slides and the SH signal was obtained (Figure 6-2).

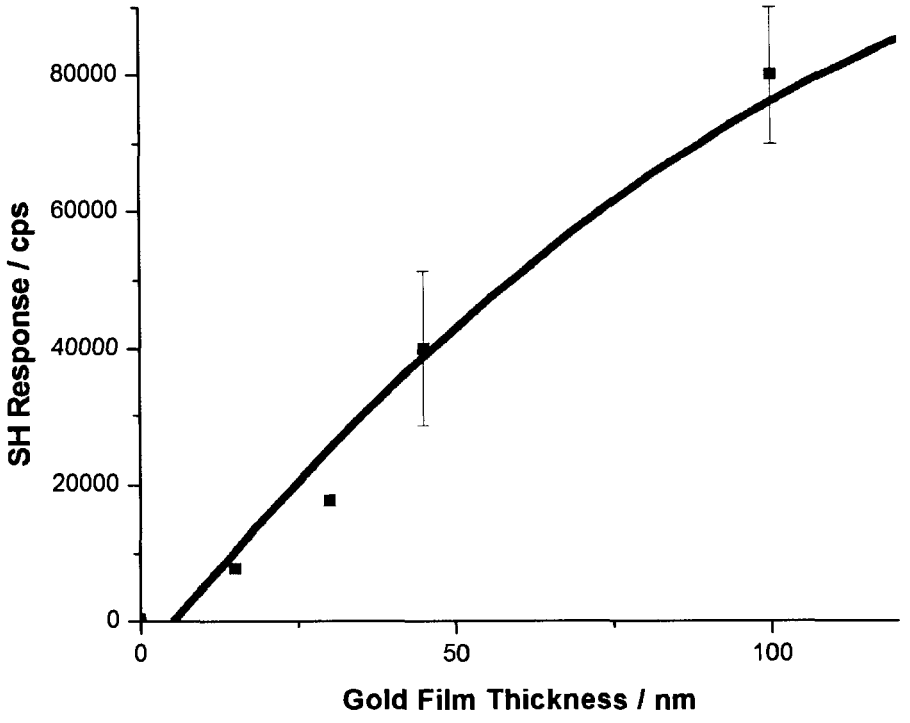


**Figure 6-2: Variation in SH intensity with increasing gold film thickness.**

The gold film thickness was chosen to coincide with the approximate thickness due to one (or more) gold nanoparticle layers. For example, 15 nm of gold is approximately equal to one nanoparticle layer, 30 nm would be 2, and so on. While a linear trend is observed, it seems logical to expect that the SH signal will reach a maximum and plateau at higher thicknesses. Therefore a non-linear ($2^{nd}$ order polynomial) equation was used to fit the data in Figure 6-2. Brasselet also noted an increase in the "background" SH signal with increasing gold deposition thickness [143], which is in agreement with the results presented here.

The increasing baseline for the NP samples can also be partially attributed to an increase in surface area [140]. Chen *et al.* [140] showed that SH signal from reflection is integrated over the area of the surface irradiated by the laser beam:

$$I_{SHG} \propto \int \left|\tilde{P}\right|^2 dA \tag{25}$$

Where P is the material polarization and dA is the area of irradiation. As was shown in Section 4.3.2.3, the surface area for the NP substrates increases linearly with increasing NP depositions. Therefore, in accordance with Equation (25), the SH intensity observed here for the NP substrates should also increase linearly.

The SH signal from gold nanoparticles can be enhanced through the same mechanism which results in field enhancement in SERS [141]. That is to say, a confinement of the electron plasma in features at roughened surfaces can result in plasmon excitation in the visible region. Plasmon excitation yields a highly enhanced electrical field at certain locations. In NLO, this enhancement can be active upon the incident fundamental beam and the harmonic field, and may be the origin of enhanced SH signals observed [67]. Therefore, similarly to the SERS data, we will attempt to correlate the SH intensity with the morphological characteristics of the surface aiming to find the source for the resonances showed in Figure 6-1.

## 6.2 Correlation of Second Harmonic signal with surface morphology parameters

As was performed in Section 5.3 with the SERS data, the SH response of the colloidal nanostructures will be correlated with three relevant morphology parameters: the surface roughness (RMS roughness), fractal dimension, and average feature diameter.

### 6.2.1 Surface roughness (RMS roughness)

As can be seen from Figure 6-3, the correlation between SH signal and RMS roughness of the surface is relatively poor. This should not be surprising, given the fact that the RMS roughness appears to plateau after 7 nanoparticle depositions, yet the SH intensity changed dramatically past this point.

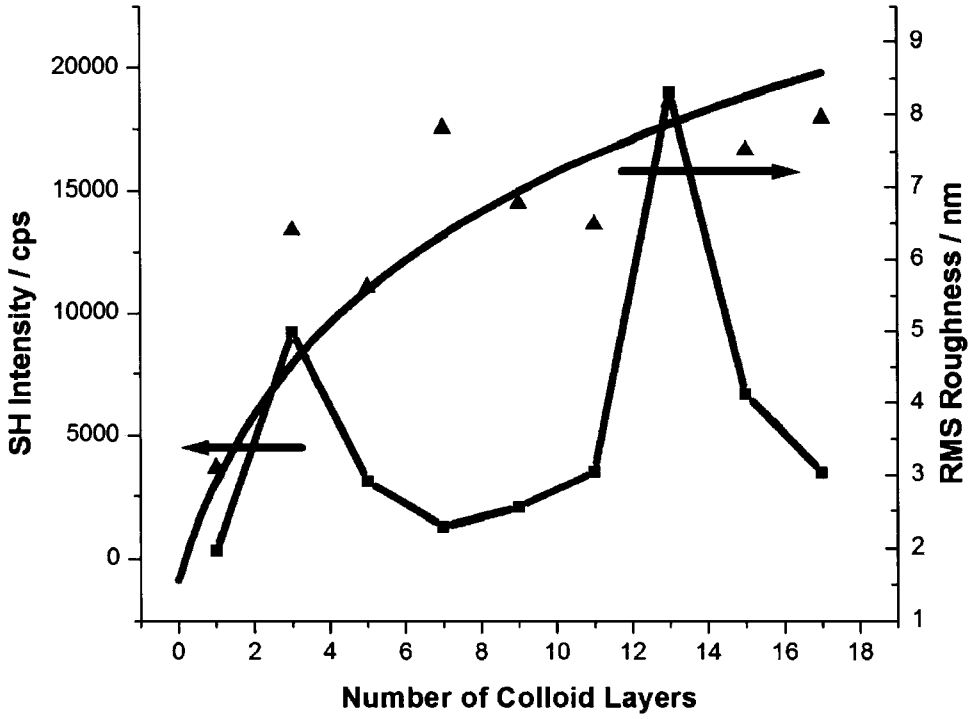


**Figure 6-3: Comparison between second harmonic signal (squares – left axis) with RMS roughness (triangles – right axis) of the nanoparticle substrates with increasing nanoparticle depositions.**

While surface roughness (or the distribution of features that make of the surface roughness) is an important consideration in the intensity of the SH signal observed, it appears that the RMS roughness parameter is not sufficient to describe the effect.

### 6.2.2 Fractal dimension

Another morphological parameter that can be tested for correlation to the second harmonic signal is the fractal dimension of the substrate. It was shown in Section 4.3.2.1

that the fractal dimension of the substrate decreases with increasing number of nanoparticle depositions.

In Section 5.3.3 the relationship between SERS intensity and fractal dimension was discussed. While it has been shown in the literature that there is a direct relationship between SERS intensity and fractal dimension for fractal-like surfaces [54, 76, 79, 80, 119, 135], the sharp transition from self-affine to bulk surfaces was not observed here. This transition has a dramatic effect on the SERS response. The relationship between SH intensity and fractal dimension, however, is not as well known [136, 142, 144]. Shown in Figure 6-4 is a comparison of the two parameters.

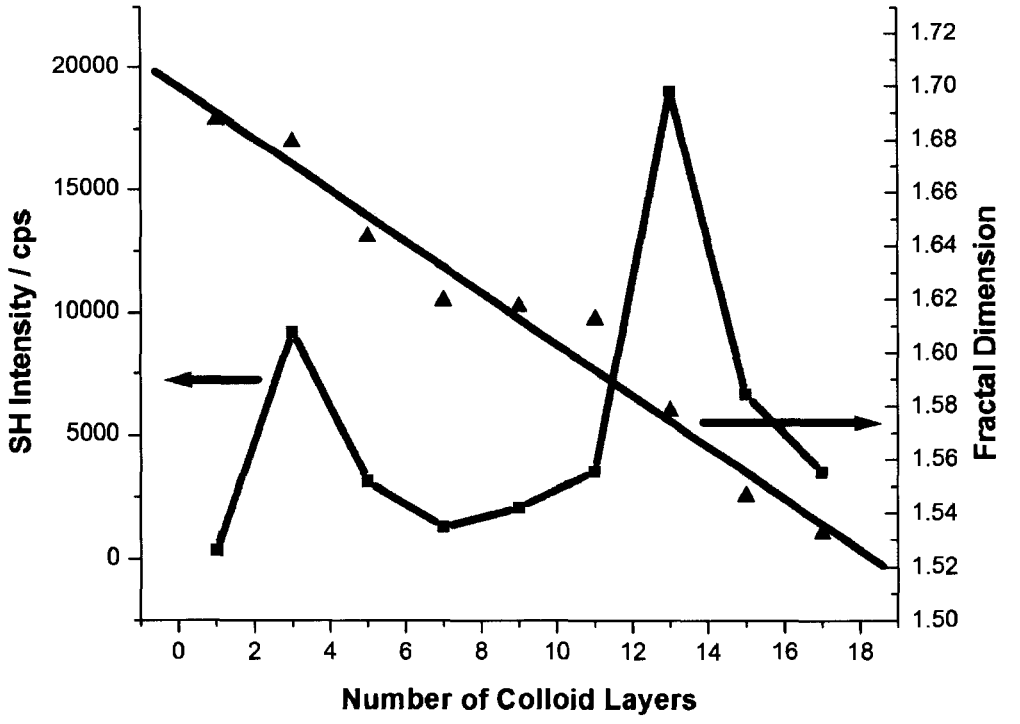


**Figure 6-4: Comparison between the Second Harmonic signal (squares – left axis) with the fractal dimension (triangles – right axis) of the nanoparticle substrate with increasing nanoparticle depositions.**

As can be seen from Figure 6-4, the correlation between the two parameters is not clear. Srinivasan has noted, however, that the relationship between second harmonic signal and particle size and shape is extremely complex [70], and presumably the fractal dimension is not a suitable parameter for analysis. In addition, the lack of transition from self-affine or fractal structures to that of bulk-like gold provides further support that the fractal dimension parameter is not suitable for further discussion here.

### 6.2.3 Average feature size

As demonstrated by Srinivasan and others, the SH signal from a gold surface is strongly dependent on the morphology of the underlying substrate [70-72, 138, 139]. Srinivasan noted that oblate hemispheroids approximately 90 – 100 nm in diameter yield the greatest SH signal in their experiments [70]. The second harmonic signal was compared to the average feature sizes to yield Figure 6-5.

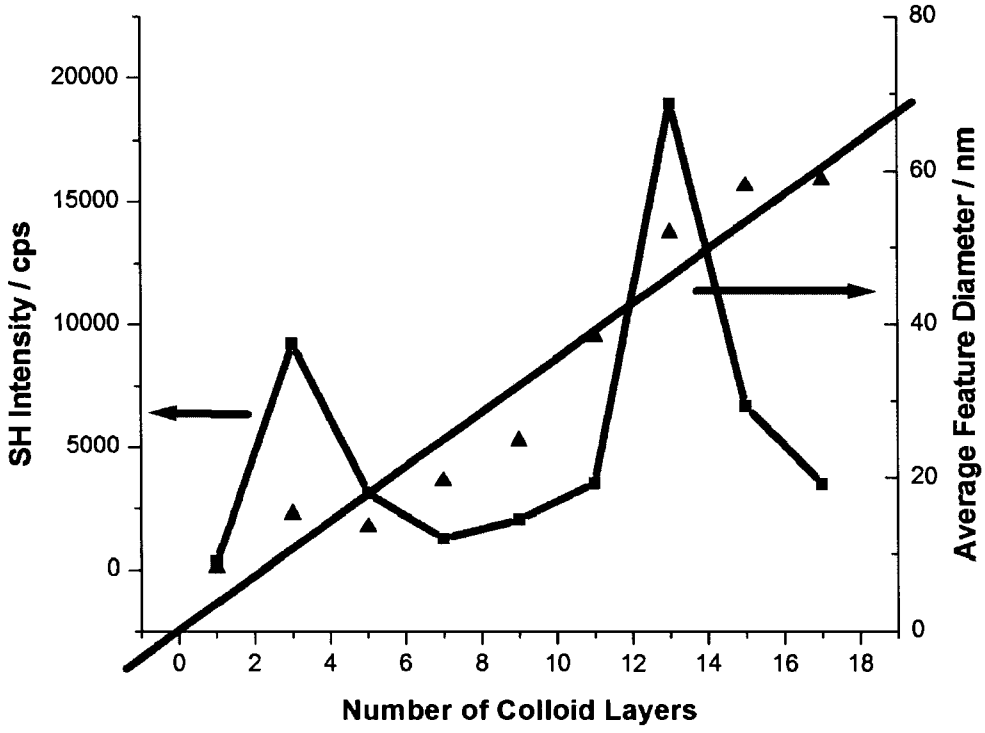


**Figure 6-5: Comparison between second harmonic signal (squares – left axis) with the average feature size (triangles – right axis) of the nanoparticle substrates with increasing nanoparticle depositions.**

As indicated in Figure 6-5, the SH intensity reaches a maximum for features approximately 52 nm in diameter.

Interesting behaviour was noted by Srinivasan *et al.* when they studied the deposition of gold onto a H-Si(111) surface [70]. This work was performed through the galvanic displacement of Si by Au under acidic conditions. In essence, the surface layer of Si is oxidized, and $Au(CN)_2^-$ is reduced to form elemental gold on the Si surface. The two relevant half-reactions are:

$$4Au(CN)_2^- + 4e^- \rightarrow 4Au + 8CN^- \quad (26)$$

$$Si + 6HF \rightarrow SiF_6^{2-} + 6H^+ + 4e^- \quad (27)$$

An initial dramatic increase in the second harmonic signal is noted due to the deposition of gold on the Si surface. The signal reaches a maximum, and then decreased with further deposition time to reach a plateau value. The change in second harmonic signal was attributed to the formation and growth of gold clusters that are shaped like oblate hemispheroids. Their results showed that lateral particle dimensions of 90 – 100 nm yielded the greatest SH signal [70, 138, 139].

The value obtained here is slightly smaller than the 90 – 100nm obtained by Srinivasan. This discrepancy could occur for a number of reasons, which are discussed below.

A correction was made for the AFM images obtained in order to account for tip-sample convolution, which results in the measured dimensions of species being substantially larger than their true dimension. This was corrected using the method published by Doron *et al.* [111] and was discussed in Section 4.2.2. One key factor that determined the magnitude of the tip-sample convolution error was the diameter of the AFM tip employed. The AFM tip diameter was estimated to be 20 nm, which is a nominal value quoted by the manufacturer. If the tip diameter is smaller than this quoted value, then the actual feature size would be closer to the measured value. This would essentially result in an "over correction" and the surface feature values obtained here would be smaller than the true value. Thus, the values obtained here could in fact be closer to the work of Srinivasan [70] than initially appears.

In addition, the actual method used to account for tip-sample convolution can dramatically affect the resultant feature size. While Srinivasan *et al.* corrected for tip-sample convolution, they did not provide any significant details about the method [70]. One can assume that the method used is that published in a previous paper by a different member of the research group [145]. In that paper, tip-sample convolution was removed by subtracting twice the tip radius from the measured diameter. For example, a 130 nm feature measured using a 20 nm tip, would end up being 90 nm as the actual feature size. In fact, the sample here yielding maximum second harmonic enhancement (13 nanoparticle layers) had a measured feature size of 130 nm, so in fact using the method of Srinivasan the values obtained here could agree remarkably well.

Srinivasan also noted that the shape, as well as the size, of the underlying surface features affects the SH signal [70]. In that work, the features were described as oblate hemispheroids. In the work performed here, the features were more of a cone-like shape (Section 4.3.2). The shape of the features are predicted to have dramatic effects on the extinction spectra [98, 146-148]. The cone-like features could result in a pronounced blue-shift, which would cause resonant excitation to occur at smaller feature sizes than for oblate hemispheroids.

As well, the work by Srinivasan was performed using *in-situ* SHG of the gold nanoparticle surface, while the work here was performed *ex-situ*. As discussed in Section 4.3.1, the wavelength of SP excitation is dependent upon the local dielectric environment. In solution (*in-situ*), gold nanoparticle assemblies exhibit a SP band near 525 nm. When obtained in air (*ex-situ*), the SP band shifts to longer wavelengths (ca. 600 nm). Therefore, for equivalent systems obtained using 820 nm excitation, the scan obtained *ex-situ* would exhibit greater SH signal than the system obtained *in-situ*.

The discussion above indicates that the second resonance peak in Figure 6-1 (for 13 NP depositions) agrees well with the literature, and may be attributed to the SP resonance of the nanostructure. This will result in an enhanced local electric field, which will give rise to an increased SH signal. In fact, this suggestion is consistent with the SERS results discussed previously (Section 5.2) – the maximum enhancement was obtained for 11 nanoparticle layers, while the maximum enhancement observed here was for 13

nanoparticle layers. This difference may be attributed to the slight red-shift in the excitation wavelength used (785 vs. 820 nm).

A sharp decrease in SH signal is noted after the resonance peak, despite an overall increase in the absorbance at the excitation wavelength (see Figure 1-3). Similar behaviour was also observed for the SERS data (Section 5.2) and by Olson *et al.* [113]. No reason has been proposed by Olson *et al.*, but this may be due to a decrease in the number of aggregates of sufficient size to allow for SP excitation.

The UV-Vis absorbance of the nanoparticle substrates at the incident fundamental frequency (820 nm) was correlated with the SH intensity (Figure 6-6). As expected, there is an overall increase in the absorbance at 820 nm with increasing number of nanoparticle depositions [10, 89]. An increase in the absorbance at the second harmonic wavelength (410 nm) was also observed.

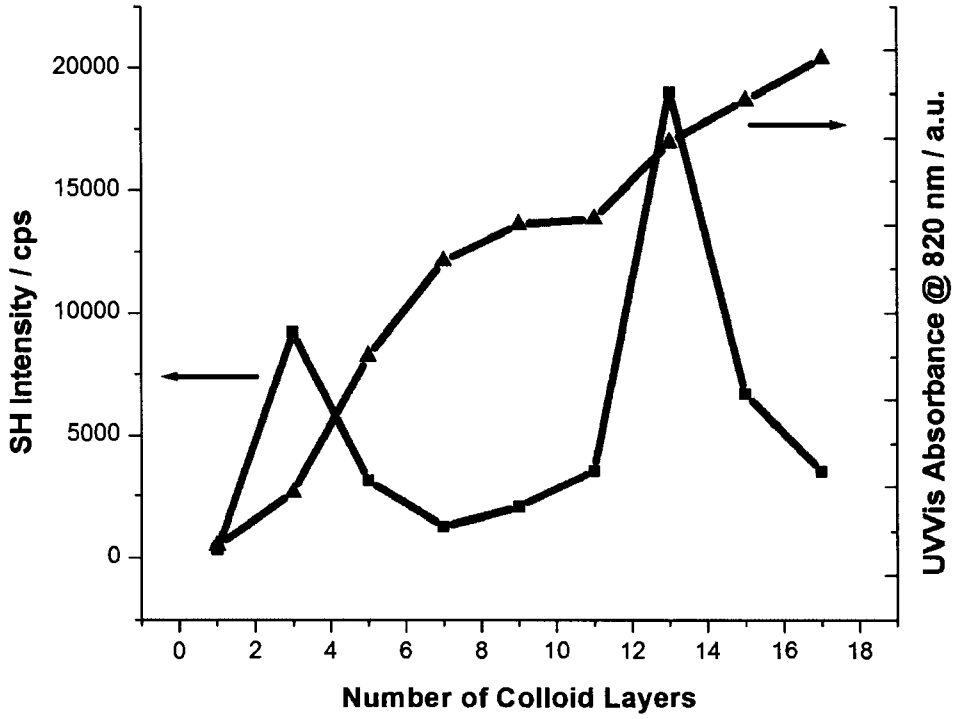


**Figure 6-6: Relationship between UV-Vis absorbance at the excitation wavelength (triangles - right axis) and SH signal (squares - left axis) with increasing number of nanoparticle layers.**

The reason for the SH resonance peak at 3 layers of NP is less clear. Initially, with one colloid layer deposited very little second harmonic signal is observed. Recall from section 4.2.2 that for one colloid layer, individual NPs were imaged using AFM. These individual NPs would exhibit a high degree of centrosymmetry, which would suppress the SSHG contribution and hence lower the observed SH signal [143, 149]. Furthermore, SESHG will not be observed because the sample shows very little absorbance at the excitation wavelength, which means SP excitation (and hence SESHG) will not occur to any appreciable extent [72, 140, 141].

The resonance at 3 NP layers may be attributed to a decrease in the overall symmetry of the nanoparticle aggregates. Examining Figure 4-14, features that are more squared-off appear in the AFM line scan. These features exhibit a lower degree of symmetry than the spherical NPs. This relative decrease in symmetry would induce an increase in the bulk SHG contribution, which would increase the observed SH signal. Alternatively, the enhanced signal for 3 NP layers may be due to the formation of extremely small nanostructures which have a resonance at the second harmonic frequency (410 nm).

The SH signal between 5 and 11 colloid layers is dramatically lower than with 3 colloid layers. The particle size, on the other hand, increases due to a higher degree of aggregation. The larger particles may provide more pathways for energy damping, therefore decreasing the efficiency of the bulk contribution. The surface contributions should dominate at these conditions until the SP resonance is achieved at 13 NP depositions.

The problem is that techniques such as UV-VIS and AFM, and the quantities derived from them, yield an average (overall) snapshot of the surface morphology. Instead, a technique such as near-field scanning optical microscopy is required to obtain a localized snapshot of the surface structure and the optical frequencies required in order to undergo SP excitation [55]. This information could then be correlated with the SH data in order to obtain a more informative understanding of the processes occurring.

# Chapter Seven: Gold Nanorods as a Substrate in Surface-enhanced Raman Scattering

In this chapter, anisotropic gold particles, referred to as nanorods (NRs), are discussed. The prepared NRs are examined using UV-Vis spectroscopy and imaged using TEM. The gold NRs are aggregated in the presence of the Raman-active molecule oxazine 720, and the SERS response of the system is monitored. Utilizing a recently published method for depositing gold NRs on a glass surface [93], the construction of multilayer substrates using gold NRs was attempted.

## 7.1 Synthesis and characterization of gold nanorods

Gold NRs can be synthesized from rigid templates, or in the presence of surfactants. In the first case, metal ions are reduced inside cylindrical pores of oxide [150] or polymeric membranes [13]. The rigid structure of the template influences the overall shape and size of the resultant cylindrical gold rods.

In the latter method, charged surfactants (such as CTAB) are used to assist in the growth of the gold nanorods [151]. The surfactants have a charged head group and a long hydrocarbon tail. For CTAB, a common surfactant used in the synthesis of NRs, the hydrocarbon tail is 16 carbons long while the polar head group is a positively-charged trimethylamino moiety.

The surfactant-assisted synthesis of gold NRs can occur through two distinct methods: Electrochemical preparation [152] and seed-mediated growth [91, 151]. Both of these surfactant-mediated methods have differing drawbacks and disadvantages, such as low yields [152], high amount of spherical by-products [151] or limited synthetic range of gold NR dimensions [152].

Many of these shortcomings were addressed in a modification of the seed-mediated growth synthesis published by Nikoobakht *et al.* [91]. In this method, a seed solution of small spherical gold nanoparticles is prepared in the presence of the CTAB surfactant. This seed solution is then used to generate the rod-shaped nanoparticles in the second step of the synthesis when it is added to a solution containing CTAB, along with gold and silver precursors ($HAuCl_4$ and $AgNO_3$, respectively). Interestingly, the amount of silver precursor present dictates the resultant aspect ratio of the gold NRs [91]. This method allowed for the synthesis of NRs with very high aspect ratios and relatively few undesirable products.

Gold nanorods are often described based on their aspect ratio (AR). The AR is the ratio of the longitude axis to its transverse axis, as shown in Figure 7-1.

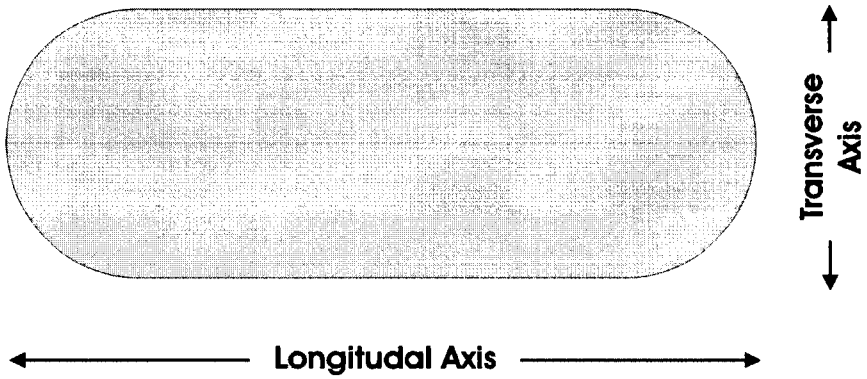


**Figure 7-1: Demonstration of the two axes in a gold nanorod. The ratio of the longitudal axis to the transverse axis yields the aspect ratio of the gold nanorod.**

The mechanism surrounding the formation of gold NRs still remains a point of discussion within the literature. It is thought that the surfactants form micelles in solution and act as soft templates (providing a constrained environment). It is also believed that gold ions and surfactant molecules form ion pairs, which are solubilized by a surfactant micelle [153]. These micelles continue to develop and by adding the seed solution, the initial spheres will also grow in size. The anisotropic growth of the spheres to form NRs is likely due to the surfactant binding preferentially to particular crystal faces. Faces on which the surfactant adsorbs strongly would be better stabilized than faces which do not have surfactant adsorbed [153]. The NR formation would occur through the joining of particles along the faces which are not properly stabilized. In the case of gold NR formation, stabilization would occur on all but two opposing faces, to allow for one-dimensional growth, as demonstrated in Figure 7-2.

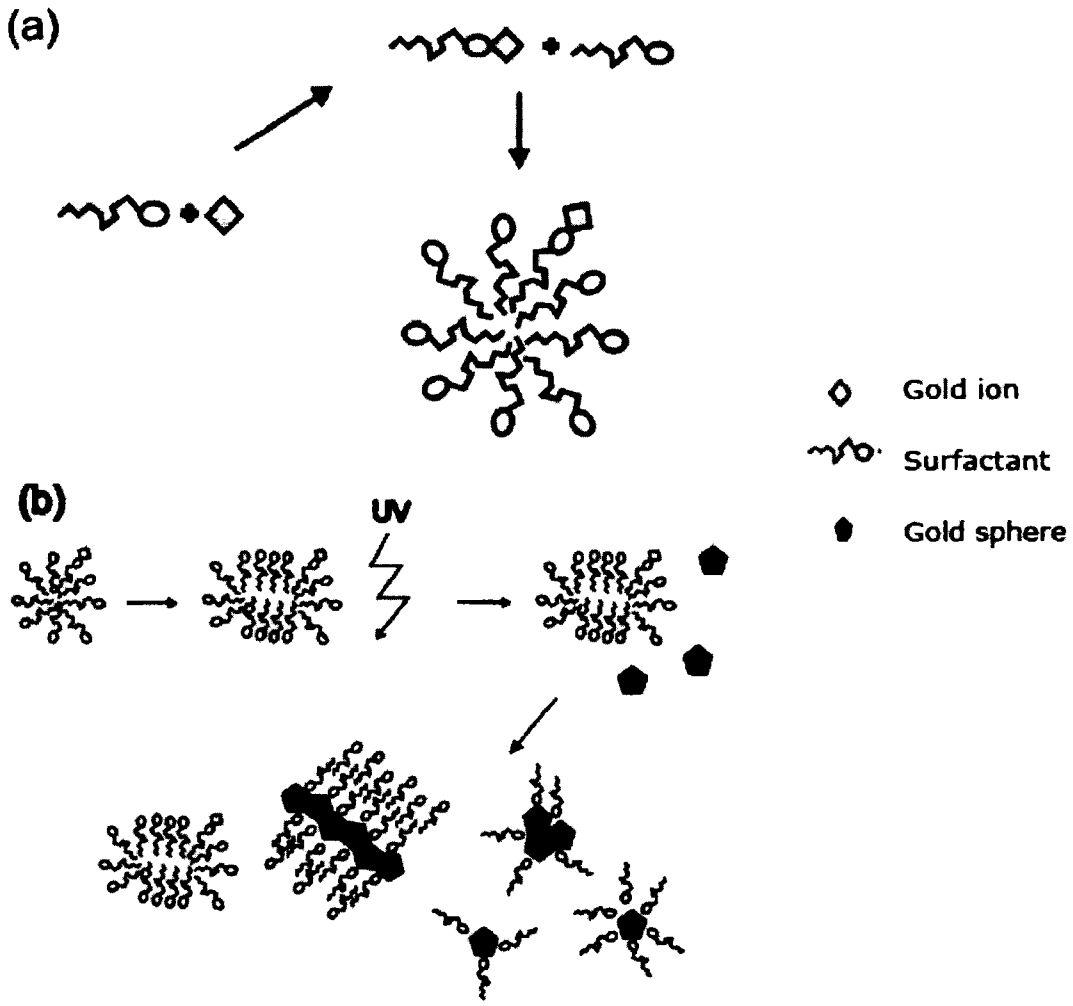


**Figure 7-2: Demonstration of the role of surfactants in the synthesis of gold nanorods. (a) Ion-pair formation and solubilization in a micelle (b) Formation of gold particles, stabilization by surfactant bilayers and one-dimensional growth by aggregation of gold particles. Note in this figure that gold spheres and rods were formed photochemically by exposure to UV light. Reprinted with permission from [153]. Copyright 2002 American Chemical Society.**

When gold nanorods are synthesized, they are protected by a bilayer assembly of surfactant around the exterior of the nanorod [154] (Figure 7-3). In the surfactant layer closest so the surface, the surfactant aligns such that the positively charged head group is interacting with the gold surface. The second layer of surfactant then interacts with the first through hydrophobic interactions of the hydrocarbon chain, while the headgroups of the outer layer are in the aqueous medium [154]. This is analogous in concept to phospholipids bilayers encountered in biological systems: the phospholipids form a bilayer to hide their hydrophobic tail regions and expose the hydrophilic head groups to water. The concept of a protecting group is somewhat analogous to spherical gold particles, in which a protective capping layer of citrate anions is present [23].

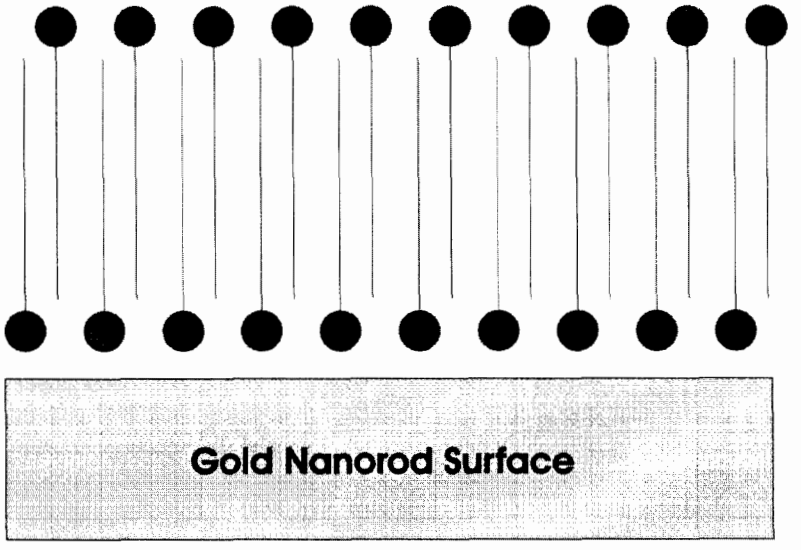


**Figure 7-3: Demonstration of the surfactant bilayer formed on the exterior of gold nanorods. This is analogous to the phospholipid bilayer that is commonly encountered in biological systems.**

The UV-Vis spectrum of gold NRs (Figure 7-4) is dramatically different that the spectrum for spherical gold nanoparticles (Figure 3-1). Because of their anisotropic nature, the plasmon resonance is split into two distinct modes for gold NRs.

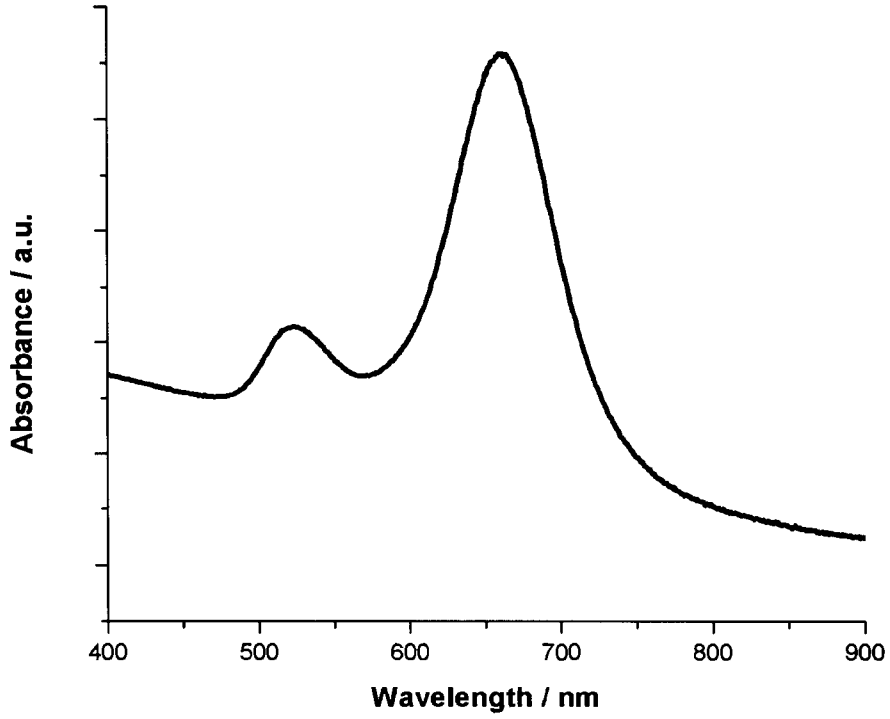


**Figure 7-4: UV-Vis spectrum of gold nanorod solution.**

The longitudal plasmon resonance occurs along the long axis of the NR, while the transverse mode occurs perpendicular to the first [146]. In Figure 7-4, the longitudal band occurs near 660 nm, while the transverse band occurs near 525 nm. The optical absorption spectra of NRs are extremely sensitive to their aspect ratio [147]. With increasing aspect ratio the longitudal band undergoes a red shift to longer wavelengths

[147]. In fact, NRs can be synthesized with a longitudal plasmon absorbance occurring anywhere between 600 and 1200 nm [91]. This wavelength-tunability makes these NRs particularly attractive when it comes to the construction of spectroscopic substrates: the NRs can have their SP band tuned to coincide with the excitation laser in SERS to obtain large enhancements under the electromagnetic enhancement mechanism. Alternatively, the SP band can be moved away from the excitation source to study the contributions of other possible enhancement mechanisms [155]. While the longitudal plasmon mode is extremely sensitive to the aspect ratio of the NRs, the transverse mode is not [156].

As with any characterization of a synthesized nanoparticle solution, it is important to obtain visual information to accurately determine the size and shape of the products. Shown in Figure 7-5 is a TEM image of the prepared gold nanorods.

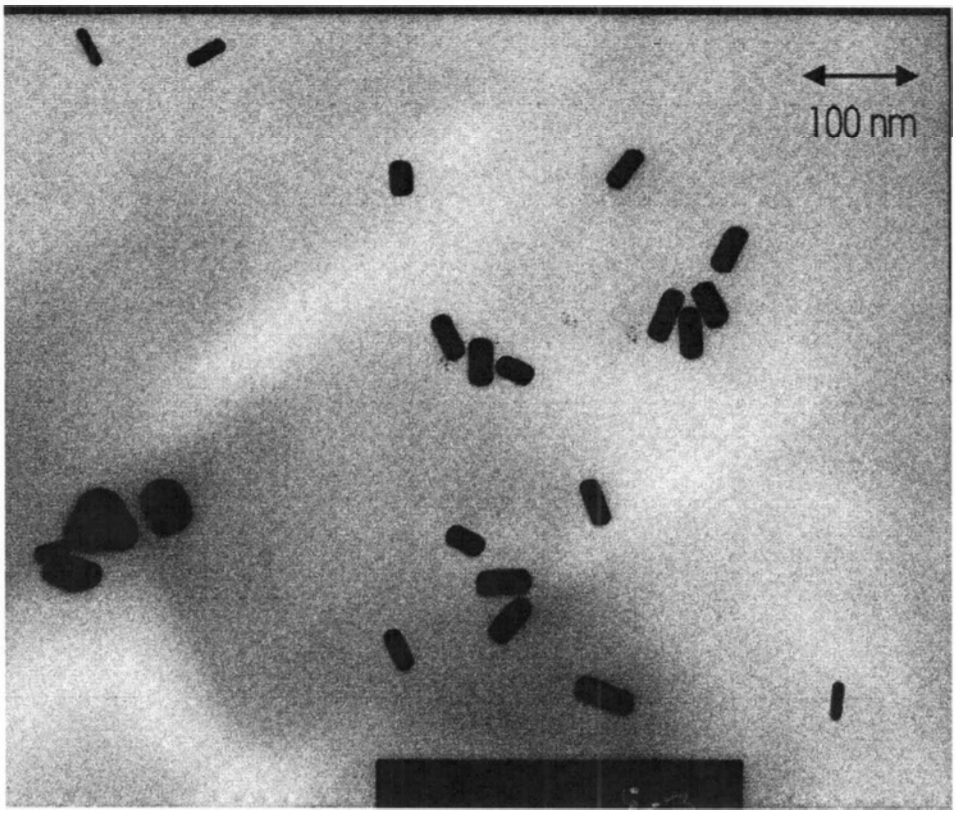


**Figure 7-5: TEM Image of gold nanorods. Note the appearance of an impurity on the far left of the image.**

Based on the TEM images obtained, the nanorods had average lengths of (23 ± 3) and (49 ± 4) nm for the transverse and longitudal axes, respectively. The ratio of these quantities yields (2.1 ± 0.5) as the AR for the gold NRs.

Similarly, the location of the longitudal plasmon resonance ($\lambda_{max}$) is related to the aspect ratio ($AR$) of the NR based on the equation [91, 147, 157]:

$$\lambda_{max} = 570 + 51 \cdot AR \qquad (28)$$

Solving for *AR* in the above equation and using the appropriate longitudal plasmon resonance value (660 nm) yields an aspect ratio of 1.8. Nonetheless, the value obtained from the UV-Vis calculation (1.8) does agree with the aspect ratio obtained from TEM imaging, within the stated experimental error.

## 7.2 SERS Response of aggregate gold nanorods

In general, the use of NRs as an enhancing substrate for SERS has been limited to the study of an analyte in the presence of NR aggregates [155, 158]. In [158], Nikoobakht *et al.* aggregated NRs through the addition of ethanol to a solution of NRs and the Raman analyte 2-aminothiophenol (2-ATP). The aggregate NRs were then deposited onto a silica surface, and their Raman spectrum measured. Highly enhanced SERS signals were obtained, and the increase was attributed to the enhancement of the electric field between the particles in the aggregates. In addition, it was noted that the aggregate NRs yielded much stronger Raman enhancement than nanospheres for similar experimental conditions.

In [155], the Raman response of molecules adsorbed on NRs in solution was studied by Nikoobakht and coworkers. Experimental enhancement factors of $10^4$-$10^5$ were observed, which was much higher than the calculated value using the Wang and Kerker [159] electromagnetic model. The difference was attributed to a contribution from the chemical enhancement mechanism. The fact that enhancement was observed is particularly interesting in this case, because excitation was performed using a near-IR

(1064 nm) laser, which is far removed from the plasmon resonance for the NRs used in the experiment. Instead, the observation of the chemical enhancement must be due to stronger-than-usual adsorption of the analyte molecule on the NR surface. A NR has four {110} crystal faces along the longitudal direction in addition to the {100} and {111} facets and four {110} facets at the end of each NR [160]. The surface energy of the {110} facet is much higher than the {100} or {111} facets [161], and will therefore lead to stronger adsorption of the molecule and hence increased chemical enhancement. Gold nanospheres do not have this {110} facet, and will therefore show much smaller chemical enhancement under the same experimental conditions [162].

Recently, Suzuki *et al.* have developed a method for obtaining the Raman spectrum of Rhodamine 6G on gold NRs, by forming a gold NR monolayer at the liquid-liquid interface of water and hexane [163]. Based on their results, it was suggested that NRs with longer aspect ratios are better SERS-enhancing substrates [163].

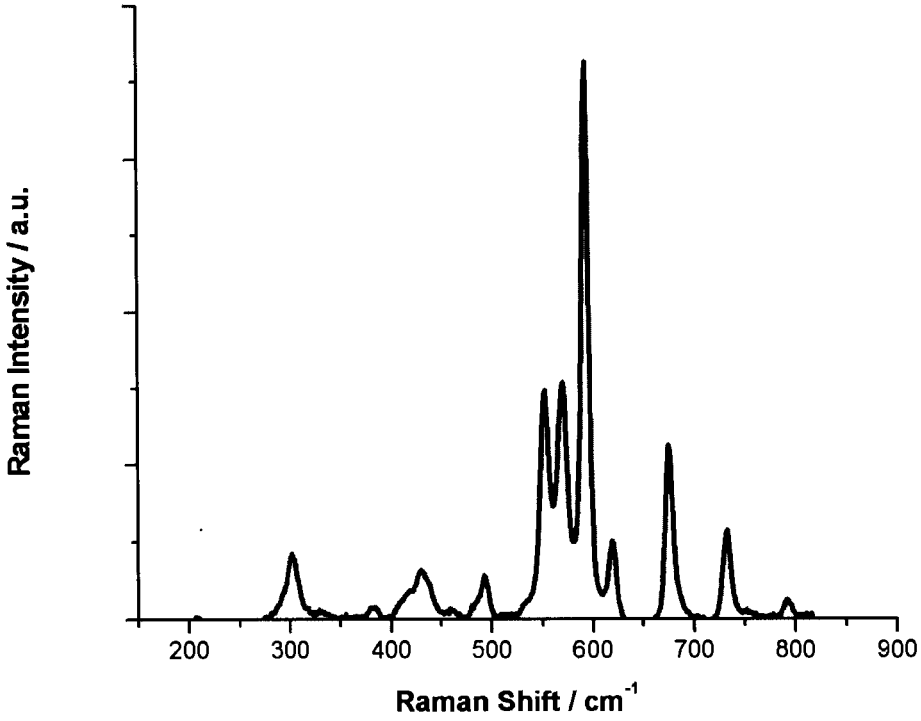


**Figure 7-6: SERS spectrum of gold nanorods aggregated in the presence of oxazine.**

To obtain the SERS spectrum of oxazine 720 presented in Figure 7-6, a small amount of oxazine was added to the gold NR solution, and this mixture was aggregated using a few drops of concentrated NaCl. Oxazine interacts with the NR aggregates, and the SERS spectrum of oxazine was obtained. It was observed that the Raman spectrum of oxazine is much stronger compared to the previous Raman spectra obtained from depositing oxazine on gold nanoparticle substrates (Figure 5-4). In particular, the Raman spectrum exhibits sharp, well-defined and strong bands, including the resolution of the bands just below 600 $cm^{-1}$, which was not observed for oxazine on gold nanoparticles. This fact suggests that gold NR substrates may be much more suitable as SERS substrates than the equivalent systems of gold nanospheres.

## 7.3 Construction of nanorod multilayer substrates

As a corollary to the work performed on the construction of multilayer substrates consisting of spherical gold nanoparticles, an attempt was made to construct multilayer substrates utilizing gold NRs. Because gold NRs yield a highly enhanced SERS signal, the potential to "tune" the roughness of the gold NR substrates to further maximize the SERS signal is an interesting avenue of research to pursue.

Prior to the publication of Niidome [93], the only known method available to deposit NRs on a substrate was limited to the aggregation procedure as demonstrated in Section 7.2 [158]. The method provided by Niidome involves the electrostatic deposition of gold NRs on to a charged glass surface through the use of charged polymers [93].

In the first step of the synthesis, glass slides are immersed in a solution of PAH, which results in the deposition of the positively charged polymer on to the glass surface. A layer of the negatively-charged polymer PSS is then deposited on top of the PAH layer, so that the outer-most layer on the slide is negatively charged. The positively-charged gold NRs (due to the CTAB-protective bilayer) are then deposited on to this negatively charged surface. To prevent aggregation of the gold NRs once assembled on the surface, the slide and NR assembly is immersed in a solution of PDDA. This positively charged polymer prevents aggregation of the NRs from occurring by "filling the gaps" between adjacent NRs [93].

After this process was completed, no obvious colour change occurred on the glass slide (to the naked eye). This is in stark contrast to the glass slides where gold nanoparticles were deposited: The slides appeared distinctly red after the nanoparticle deposition procedure. The lack of colour here suggests that no deposition occurred.

To verify this hypothesis, the UV-Vis spectrum of the glass slide was obtained before and after the NR deposition procedure (Figure 7-7). It can be seen that there is no change in the UV-Vis response of the glass slide. This provides solid, concrete evidence that NR deposition was not successful.

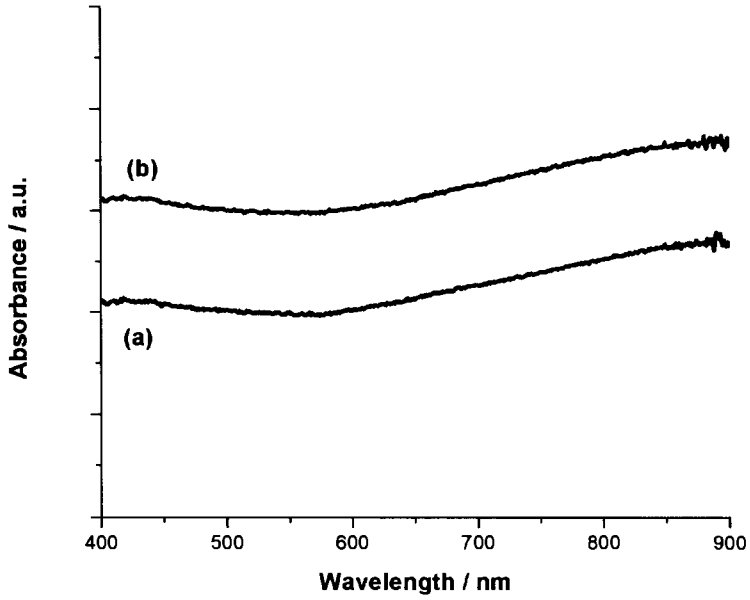


**Figure 7-7: UV-Vis spectrum of a glass slide (a) before and (b) after one nanorod deposition procedure. The spectra have been offset to allow for easier comparison. No obvious change in the visible spectrum occurs, indicating deposition of gold nanorods has not occurred.**

One possible reason for the lack of nanorod self-assembly could be due to excess CTAB remaining in solution. Here, excess CTAB refers to CTAB molecules that do not directly participate in the protecting bilayer around the nanorods but are dissolved and floating freely in solution. If excess CTAB of sufficient concentration is present, this CTAB may preferentially attach to the negatively charged PSS layer through electrostatic means. This CTAB would then block all active, available PSS sites, and would thus inhibit the CTAB-clad NRs from depositing on the modified glass slide.

Removing the excess CTAB can be performed by centrifuging the NR solution. Centrifugation causes all of the NRs to collect at the bottom of the centrifuge tube. Removal of the supernatant and redispersing in deionized water will have the effect of removing excess CTAB from the NR solution. However, there is also a fine balance when trying to remove the excess surfactant in order to allow for NR assembly: Centrifuging the nanorod solution in excess will result in irreversible aggregation of the nanorods [92]. This suggests that there is a very small window of acceptable excess CTAB, and this value has not been achieved at present.

Other work has also recently been published by Gole *et al.*, in which nanorods were deposited onto an acid-terminated monolayer [92]. While this represents a very useful potential method for creating nanorod-derived superstructures, the fact that an underlying gold surface is required for self-assembly of the acid-terminated monolayer presents a major drawback. Namely, a thick gold layer will prevent the use of UV-Vis methods to

characterize the nanorod superstructures. Alternatives to this method could be attempted, however, using silane derivatives on glass slides to yield pendant acid-terminated groups to allow for nanorod deposition.

In addition, work recently published by Caswell *et al.* demonstrated the assembly of nanorods using biotin-streptavidin connectors [164]. The use of DNA strands for NR assembly was published by Dujardin *et al.* [165]. Two NR solutions are prepared, and derivatized with single-stranded DNA with a pendant thiol group. It is important to note that the two DNA strands used are complementary in nature, so that when they come in contact, the two DNA strands will duplex and result in the formation of a NR superstructure. This method is complementary to that published by Mirkin, in which spherical gold nanoparticles were derivatized with single-stranded DNA and allowed to duplex with the complementary strand [166]. Both of the methods described above may be potential avenues of research for the construction of NR superstructures.

# Chapter Eight: Conclusions

## 8.1 Conclusions

In this work, it has been demonstrated that three-dimensional colloid containing nanostructures are suitable as a substrate in SERS and SHG.

It has been shown that gold nanoparticles are a versatile building block in the synthesis of nanostructured materials because of their well-defined physical and chemical properties. Gold nanoparticles also posses an intense plasmon absorption feature, which results in colloidal gold being strongly coloured. Gold nanoparticles can be varied in size to yield a material of suitable dimension: Change in dimension of the gold nanoparticles has a dramatic effect upon the optical absorption spectrum. The gold nanoparticles were characterized using UV-Vis spectroscopy and the TEM technique. It was shown that the gold nanoparticles synthesized here were (14 ± 2) nm in diameter.

To facilitate construction of the nanoparticle multilayer assemblies, a glass surface was derivatized using MPTMS. This resulted in a pendant thiol group emanating from the glass surface. Using well-known gold-thiol chemistry, gold nanoparticles were then deposited onto the derivatized glass surface. The 2D nanostructures were intensely-red coloured due to the adsorbed gold nanoparticles. Indeed, the optical absorption spectrum showed a pronounced absorption feature near 520 nm. When the 2D nanostructure was exposed to air, aggregation of the particles occurred, resulting in the absorption feature

shifting to longer wavelengths. The surface morphology was examined using the AFM technique. Individual gold nanoparticles were imaged, with height features of approximately 11 nm. This is on the order of the nanoparticle dimension obtained using the TEM technique.

Three-dimensional nanostructures were synthesized through alternate immersions in propanedithiol and gold nanoparticles. This process was repeated until the desired number of gold nanoparticle layers was obtained. The resultant structures were then characterized using UV-Vis spectroscopy and AFM. The optical absorbance increased with increasing number of layers and the plasmon maximum shifted to longer wavelengths, suggesting increasing aggregation of the gold nanoparticles. Imaging using AFM showed that the surface morphology undergoes a dramatic change with increasing nanoparticle depositions: There is a change from independent nanoparticles to mountainous-like structures as the nanoparticles aggregate. The average feature size and the surface area were shown to linearly increase with increasing nanoparticle depositions.

These multilayer nanoparticle substrates were examined for their suitability as a substrate in surface-enhanced Raman scattering (SERS). Oxazine-720 was chosen as the analyte molecule of which the Raman spectrum would be obtained, and it was deposited onto the top-most layer of gold nanoparticles. Measurement of the SERS spectra showed that the one nanoparticle layer substrates yield very little signal (and are hence very poorly enhancing). The SERS spectra gradually increase in intensity, and reach a maximum for 11 nanoparticle layers. After this point, there is a subsequent decrease in the SERS

spectra intensity. Therefore, under these particular experimental conditions, substrates with 11 nanoparticle layers are the greatest SERS-enhancing substrates.

While the surface area increased by approximately 30%, the SERS signal underwent a 3200% increase. Furthermore, while the surface area continually increases with increasing depositions, the SERS signal is reduced between 13 and 17 nanoparticle layers. Therefore, the increase in SERS signal cannot be attributed to the increasing surface area. Instead, the change was shown to be due to the underlying surface morphology. It is well-known that features in the 3 – 100 nm size regime yield the greatest SERS enhancement [8, 54, 137]. In this work, the correlation between feature size and SERS signal indicated that features that are 40 nm in size result in the largest SERS enhancement.

It can be seen that the surface morphology of the nanoparticle substrates can be "tuned" to yield the maximum SERS signal by increasing/decreasing the desired number of nanoparticle depositions. These substrates are therefore a modular, highly-enhancing and cost-efficient method for the production of SERS substrates.

The NLO properties of the colloidal substrates was also examined using SHG. Two resonances were observed over a roughly linearly-increasing baseline. The nature of the first resonance cannot be fully explained, but may be due to a reduction in the overall symmetry of the aggregates which would increase the observed SH signal. The second

resonance is much stronger, and is attributed to the surface plasmon excitation which enhanced the local electric field, resulting in an enhanced SH signal.

## 8.2 Future work

The use of anistotropic gold particles – gold NRs – is a potential avenue for future research as a SERS substrate. It has been demonstrated by others that the anisotropic nature of gold NRs make them highly enhancing as a SERS substrate [155, 158, 163]. Gold NRs offer the ability to "tune" the longitudal plasmon resonance by varying the aspect ratio of the gold NRs. Therefore, one can vary the longitudal plasmon resonance to be coincident with the excitation source in a SERS experiment, to provide further enhancement through the EM mechanism. Alternatively, one can "de-tune" the plasmon resonance away from the excitation source in order to study other contributions to the SERS enhancement [155].

Methods have recently been published for the synthesis and self-assembly of gold NRs [91-93, 163]. In combination with the preliminary work performed in this thesis, nanostructures containing gold NRs would be a suitable extension of this work.

## Chapter Nine: References


1. Goss, C.A., D.H. Charych, and M. Majda, *Application of (3-mercaptopropyl)trimethoxysilane as a molecular adhesive in the fabrication of vapor-deposited gold electrodes on glass substrates.* Analytical Chemistry, 1991. **63**(1): p. 85-8.
2. Keating, C.D., et al., *Kinetics and thermodynamics of Au colloid monolayer self-assembly.* Journal of Chemical Education, 1999. **76**(7): p. 949-955.
3. Grabar, K.C., et al., *Nanoscale Characterization of Gold Colloid Monolayers: A Comparison of Four Techniques.* Analytical Chemistry, 1997. **69**(3): p. 471-477.
4. Grabar, K.C., et al., *Kinetic Control of Interparticle Spacing in Au Colloid-Based Surfaces: Rational Nanometer-Scale Architecture.* Journal of the American Chemical Society, 1996. **118**(5): p. 1148-53.
5. Bright, R.M., et al., *Chemical and Electrochemical Ag Deposition onto Preformed Au Colloid Monolayers: Approaches to Uniformly-Sized Surface Features with Ag-Like Optical Properties.* Langmuir, 1996. **12**(3): p. 810-17.
6. Grabar, K.C., et al., *Preparation and Characterization of Au Colloid Monolayers.* Analytical Chemistry, 1995. **67**(4): p. 735-43.
7. Rubin, S., et al., *Novel approach for the preparation of metal colloid monolayers on modified surfaces.* Journal of Vacuum Science & Technology, A: Vacuum, Surfaces, and Films, 1996. **14**(3, Pt. 2): p. 1870-1877.
8. Freeman, R.G., et al., *Self-assembled metal colloid monolayers: an approach to SERS substrates.* Science (Washington, D. C.), 1995. **267**(5204): p. 1629-31.
9. Mayya, K.S., V. Patil, and M. Sastry, *An Optical Absorption Investigation of Cross-Linking of Gold Colloidal Particles with a Small Dithiol Molecule.* Bulletin of the Chemical Society of Japan, 2000. **73**(8): p. 1757-1761.
10. Li, W., et al., *Self-assembled multilayers of alternating gold nanoparticles and dithiols: approaching to superlattice.* Colloids and Surfaces, A: Physicochemical and Engineering Aspects, 2000. **175**(1-2): p. 217-223.
11. Joo, S.W., S.W. Han, and K. Kim, *Adsorption characteristics of 1,3-propanedithiol on gold. Surface-enhanced Raman scattering and ellipsometry study.* Journal of Physical Chemistry B, 2000. **104**(26): p. 6218-6224.
12. Joo, S.W., S.W. Han, and K. Kim, *Multilayer Formation of 1,2-Ethanedithiol on Gold: Surface-Enhanced Raman Scattering and Ellipsometry Study.* Langmuir, 2000. **16**(12): p. 5391-5396.
13. Link, S. and M.A. El-Sayed, *Shape and size dependence of radiative, non-radiative and photothermal properties of gold nanocrystals.* International Reviews in Physical Chemistry, 2000. **19**(3): p. 409-453.
14. Handley, D.A., *The Development and Application of Colloidal Gold as a Microscopic Probe*, in *Colloidal Gold: Principles, Methods and Applications*, M.A. Hayat, Editor. 1989, Academic Press, Inc.: Toronto.
15. Weiser, H.B., *The Colloidal Elements.* Inorganic Colloid Chemistry. Vol. 1. 1933, New York: John Wiley & Sons, Inc.
16. Faraday, M., *Experimental relations of gold (and other metals) to light.* Philos. Trans. R. Soc. London, 1857. **147**: p. 145.

17. Ostwald, W., *Practical Colloid Chemistry*. 4th ed. 1924, New York: Dutton.
18. Mie, G., *The Optical Properties of Colloidal Gold Solutions*. Physik. Z., 1908. **8**: p. 769.
19. Zsigmondy, R., *Zur Erkenntniss des Kolloide Gold*. Z. Electrochem., 1889. **4**: p. 546.
20. Wernicke, R. and R.B. Losson, *Preparation of colloidal gold by the Zsigmondy method. I. Factors that affect the quality of distilled water. Action of traces of hydrogen sulfide*. Anales de la Asociacion Quimica Argentina (1921-2001), 1930. **18**: p. 74-97.
21. Link, S. and M.A. El-Sayed, *Optical properties and ultrafast dynamics of metallic nanocrystals*. Annual Review of Physical Chemistry, 2003. **54**: p. 331-366.
22. Frens, G., *Controlled nucleation for the regulation of the particle size in monodisperse gold solutions*. Nature (London, United Kingdom) Physical Sciences, 1973. **241**: p. 20.
23. Handley, D.A., *Methods for Synthesis of Colloidal Gold*, in *Colloidal Gold: Principles, Methods and Applications*, M.A. Hayat, Editor. 1989, Academic Press, Inc.: Toronto.
24. Naumov, V.V., *The reaction for the preparation of colloidal gold solutions by the formaldehyde method and the influence of carbon dioxide upon the formation of these solutione*. Z. anorg. Chem., 1914. **88**: p. 38-48.
25. Doerinckel, F., *Preparation of Colloidal Gold Solutions by means of Hydrogen Peroxide*. Z. anorg. Chem., 1910. **63**: p. 344-8.
26. Muller, A., F. Urbach, and F. Blank, *Formation of colloidal gold sad platinum in phosphoric acid*. Kolloid-Zeitschrift, 1928. **44**: p. 185-6.
27. Donau, J., *The formation of colloidal solutions by flames or electrical spark discharge*. Kolloid-Zeitschrift, 1915. **16**: p. 81.
28. Schmid, G., *Large clusters and colloids. Metals in the embryonic state*. Chemical Reviews (Washington, D. C.), 1992. **92**(8): p. 1709-27.
29. Brust, M., et al., *Synthesis of thiol-derivatized gold nanoparticles in a two-phase liquid-liquid system*. Journal of the Chemical Society, Chemical Communications, 1994(7): p. 801-2.
30. Link, S. and M.A. El-Sayed, *Spectral Properties and Relaxation Dynamics of Surface Plasmon Electronic Oscillations in Gold and Silver Nano-dots and Nano-rods*. Journal of Physical Chemistry B, 1999. **103**(40): p. 8410-8426.
31. Faulk, W.P. and G.M. Taylor, *Immunocolloid method for the electron microscope*. Immunochemistry, 1971. **8**(11): p. 1081-3.
32. Horisberger, M., J. Rosset, and H. Bauer, *Colloidal gold granules as markers for cell surface receptors in the scanning electron microscope*. Experientia, 1975. **31**(10): p. 1147-9.
33. Geoghegan, W.D., J.J. Scillian, and G.A. Ackerman, *The detection of human B lymphocytes by both light and electron microscopy utilizing colloidal gold labeled anti-immunoglobulin*. Immunological Communications, 1978. **7**(1): p. 1-12.
34. De Waele, M., et al., *Immunogold staining method for the light microscopic detection of leukocyte cell surface antigens with monoclonal antibodies: its application to the enumeration of lymphocyte subpopulations*. Journal of Histochemistry and Cytochemistry, 1983. **31**(3): p. 376-81.

35. Horisberger, M. and M. Vonlanthen, *Fluorescent colloidal gold: a cytochemical marker for fluorescent and electron microscopy.* Histochemistry, 1979. **64**(1): p. 115-18.
36. Graetzel, M., *Electrochemistry in Colloids and Dispersions*, R.A. Mackay and J. Texter, Editors. 1992, VCH: Weinheim.
37. Kamat, P.V. and D. Meisel, *Semiconductor Nanoclusters-Physical, Chemical, and Catalytic Aspects.* Studies in Surface Science and Catalysis. Vol. 103. 1997, Amsterdam: Elsevier.
38. Edelstein, A.S. and R.C. Cammarata, *Nanoparticles: Synthesis, Properties and Applications.* 1996, Bristol: Inst. Phys.
39. Aiken, J.D., III and R.G. Finke, *A review of modern transition-metal nanoclusters: their synthesis, characterization, and applications in catalysis.* Journal of Molecular Catalysis A: Chemical, 1999. **145**(1-2): p. 1-44.
40. Reetz, M.T. and S.A. Quaiser, *A new method for the preparation of nanostructured metal clusters.* Angewandte Chemie, International Edition in English, 1995. **34**(20): p. 2240-1.
41. Boennemann, H., et al., *Nanoscale colloidal metals and alloys stabilized by solvents and surfactants. Preparation and use as catalyst precursors.* Journal of Organometallic Chemistry, 1996. **520**(1-2): p. 143-162.
42. Okumura, M., *Preparation of gold catalysts.* Osaka Kogyo Gijutsu Kenkyusho Hokoku, 1999. **393**: p. 6-10.
43. Rossi, M., S. Biella, and M. Comotti, *Process and colloidal bimetallic catalysts based on gold and platinum for the preparation of aldonic acids from aldoses*, in *PCT Int. Appl.* 2005, (Universita' Degli Studi di Milano, Italy). Wo. p. 24 pp.
44. Raman, C.V. and K.S. Krishnan, *A new type of secondary radiation.* Nature (London, United Kingdom), 1928. **121**: p. 501-2.
45. Long, D.A., *Raman Spectroscopy.* 1977, Toronto: McGraw-Hill International Book Company.
46. Long, D.A., *The Raman Effect.* 2002, Toronto: John Wiley & Sons.
47. Franken, P.A., et al., *Generation of Optical Harmonics.* Physical Review Letters, 1961. **7**: p. 118.
48. Maiman, T.H., *Solid-state laser and iraser studies.* Solid-State Electronics, 1962. **4**: p. 236-49.
49. Boyd, R.W., *Nonlinear Optics.* 1992, Toronto: Academic Press, Inc.
50. Zernike, F. and J.E. Midwinter, *Applied Nonlinear Optics.* Wiley Series in Pure and Applied Optics, ed. S.S. Ballard. 1973, Toronto: John Wiley & Sons.
51. Shen, Y.R., *The Principles of Nonlinear Optics.* 1984, Toronto: John Wiley & Sons.
52. Otto, A., et al., *Surface-enhanced Raman scattering.* Journal of Physics: Condensed Matter, 1992. **4**(5): p. 1143-212.
53. Lyon, L.A., et al., *Raman Spectroscopy.* Analytical Chemistry, 1998. **70**(12): p. 341R-361R.
54. Campion, A. and P. Kambhampati, *Surface-enhanced Raman scattering.* Chemical Society Reviews, 1998. **27**(4): p. 241-250.
55. Kneipp, K., et al., *Ultrasensitive chemical analysis by Raman spectroscopy.* Chemical Reviews (Washington, D. C.), 1999. **99**(10): p. 2957-2975.

56. Fleischmann, M., P.J. Hendra, and A.J. McQuillan, *Raman spectra of pyridine adsorbed at a silver electrode.* Chemical Physics Letters, 1974. **26**(2): p. 163-6.
57. Jeanmaire, D.L. and R.P. Van Duyne, *Surface Raman spectroelectrochemistry. Part I. Heterocyclic, aromatic, and aliphatic amines adsorbed on the anodized silver electrode.* Journal of Electroanalytical Chemistry and Interfacial Electrochemistry, 1977. **84**(1): p. 1-20.
58. Albrecht, M.G. and J.A. Creighton, *Anomalously intense Raman spectra of pyridine at a silver electrode.* Journal of the American Chemical Society, 1977. **99**(15): p. 5215-17.
59. Lombardi, J.R., et al., *Charge-transfer theory of surface enhanced Raman spectroscopy: Herzberg-Teller contributions.* Journal of Chemical Physics, 1986. **84**(8): p. 4174-80.
60. Otto, A., *The electronic contribution to SERS. The present experimental status.* Colloids and Surfaces, 1989. **38**(1-3): p. 27-36.
61. Moskovits, M., *Surface-enhanced spectroscopy.* Reviews of Modern Physics, 1985. **57**(3, Pt. 1): p. 783-826.
62. Schatz, G.C. and R.P. Van Duyne, *Electromagnetic Mechanism of Surface-enhanced Spectroscopy*, in *Handbook of Vibrational Spectroscopy*, J.M. Chalmers and P.R. Griffiths, Editors. 2002, Johny Wiley & Sons Ltd.: Chichester.
63. Pettinger, B., *In situ Raman spectroscopy at metal electrodes.* Adsorpt. Mol. Met. Electrodes, 1992: p. 285-345.
64. Zeman, E.J. and G.C. Schatz, *An accurate electromagnetic theory study of surface enhancement factors for silver, gold, copper, lithium, sodium, aluminum, gallium, indium, zinc, and cadmium.* Journal of Physical Chemistry, 1987. **91**(3): p. 634-43.
65. Mohamed, M.B., et al., *The 'lightning' gold nanorods: fluorescence enhancement of over a million compared to the gold metal.* Chemical Physics Letters, 2000. **317**(6): p. 517-523.
66. Antoine, R., et al., *Surface plasmon enhanced second harmonic response from gold clusters embedded in an alumina matrix.* Journal of Applied Physics, 1998. **84**(8): p. 4532-4536.
67. Galletto, P., et al., *Enhancement of the second harmonic response by adsorbates on gold colloids. The effect of aggregation.* Journal of Physical Chemistry B, 1999. **103**(41): p. 8706-8710.
68. Galletto, P., et al., *Size dependence of the surface plasmon enhanced second harmonic response of gold colloids: towards a new calibration method.* Chemical Communications (Cambridge), 1999(7): p. 581-582.
69. Clark, H.A., et al., *Second harmonic generation properties of fluorescent polymer-encapsulated gold nanoparticles.* Journal of the American Chemical Society, 2000. **122**(41): p. 10234-10235.
70. Srinivasan, R., Y. Tian, and I.I. Suni, *Surface plasmon effects on surface second harmonic generation during Au nanoparticle deposition onto H-Si(1 1 1).* Surface Science, 2001. **490**(3): p. 308-314.
71. Agarwal, G.S. and S.S. Jha, *Theory of second harmonic generation at a metal surface with surface plasmon excitation.* Solid State Communications, 1982. **41**(6): p. 499-501.

72. Wokaun, A., et al., *Surface second-harmonic generation from metal island films and microlithographic structures.* Physical Review B: Condensed Matter and Materials Physics, 1981. **24**(2): p. 849-56.
73. Tuovinen, H., et al., *Linear and second-order nonlinear optical properties of arrays of noncentrosymmetric gold nanoparticles.* Journal of Nonlinear Optical Physics & Materials, 2002. **11**(4): p. 421-432.
74. Lee, P.C. and D. Meisel, *Adsorption and surface-enhanced Raman of dyes on silver and gold sols.* Journal of Physical Chemistry, 1982. **86**(17): p. 3391-5.
75. Schneider, S., et al., *Stabilization of silver colloids by various types of anions and their effect on the surface-enhanced Raman spectra of organic dyes.* Journal of Raman Spectroscopy, 1996. **27**(1): p. 57-68.
76. Vlckova, B., et al., *SERS spectroscopy with Ag colloids.* Journal of Molecular Structure, 1997. **408-409**: p. 149-154.
77. Halteen, J.C. and R.P. Van Duyne, *Nanosphere lithography: A materials general fabrication process for periodic particle array surfaces.* Journal of Vacuum Science & Technology, A: Vacuum, Surfaces, and Films, 1995. **13**(3, Pt. 2): p. 1553-8.
78. Zhang, W.-W., et al., *Surface-enhanced Raman scattering (SERS) from different azobenzene self-assembled monolayers and sandwiches.* Journal of Colloid and Interface Science, 2003. **268**(1): p. 173-180.
79. Douketis, C., et al., *Fractal character of cold-deposited silver films determined by low-temperature scanning tunneling microscopy.* Physical Review B: Condensed Matter, 1995. **51**(16): p. 11022-31.
80. Douketis, C., et al., *Self-affine silver films and surface-enhanced Raman scattering: Linking spectroscopy to morphology.* Journal of Chemical Physics, 2000. **113**(24): p. 11315-11323.
81. Solecka-Cermakova, K., B. Vlckova, and F. Lednicky, *Structural Characteristics of Ag Colloid-Adsorbate Films Determined from Transmission Electron Microscopic Images: Fractal Dimensions, Particle Size, and Spacing Distributions and Their Relationship to Formation and Optical Responses of the Films.* Journal of Physical Chemistry, 1996. **100**(12): p. 4954-60.
82. Muniz-Miranda, M. and M. Innocenti, *AFM and micro-Raman investigation on filters coated with silver colloidal nanoparticles.* Applied Surface Science, 2004. **226**(1-3): p. 125-130.
83. Brolo, A.G., et al., *Nanohole-Enhanced Raman Scattering.* Nano Letters, 2004. **4**(10): p. 2015-2018.
84. Musick, M.D., et al., *Stepwise Construction of Conductive Au Colloid Multilayers from Solution.* Chemistry of Materials, 1997. **9**(7): p. 1499-1501.
85. Suzuki, M., et al., *Surface-Enhanced Nonresonance Raman Scattering from Size- and Morphology-Controlled Gold Nanoparticle Films.* Journal of Physical Chemistry B, 2004. **108**(31): p. 11660-11665.
86. Li, X., et al., *Self-Assembled Metal Colloid Films: Two Approaches for Preparing New SERS Active Substrates.* Langmuir, 2004. **20**(4): p. 1298-1304.
87. Chumanov, G., et al., *Colloidal metal films as a substrate for surface-enhanced spectroscopy.* Journal of Physical Chemistry, 1995. **99**(23): p. 9466-71.

88. Bright, R.M., M.D. Musick, and M.J. Natan, *Preparation and Characterization of Ag Colloid Monolayers.* Langmuir, 1998. **14**(20): p. 5695-5701.
89. Musick, M.D., et al., *Metal Films Prepared by Stepwise Assembly. 2. Construction and Characterization of Colloidal Au and Ag Multilayers.* Chemistry of Materials, 2000. **12**(10): p. 2869-2881.
90. Mulvaney, S.P., et al., *Three-layer substrates for surface-enhanced Raman scattering: preparation and preliminary evaluation.* Journal of Raman Spectroscopy, 2003. **34**(2): p. 163-171.
91. Nikoobakht, B. and M.A. El-Sayed, *Preparation and growth mechanism of gold nanorods (NRs) using seed-mediated growth method.* Chemistry of Materials, 2003. **15**(10): p. 1957-1962.
92. Gole, A., C.J. Orendorff, and C.J. Murphy, *Immobilization of Gold Nanorods onto Acid-Terminated Self-Assembled Monolayers via Electrostatic Interactions.* Langmuir, 2004. **20**(17): p. 7117-7122.
93. Niidome, Y., et al., *Immobilization of gold nanorods on the glass substrate by the electrostatic interactions for localized plasmon sensing.* Chemistry Letters, 2004. **33**(4): p. 454-455.
94. Brolo, A.G., P. Germain, and G. Hager, *Investigation of the Adsorption of L-Cysteine on a Polycrystalline Silver Electrode by Surface-Enhanced Raman Scattering (SERS) and Surface-Enhanced Second Harmonic Generation (SESHG).* Journal of Physical Chemistry B, 2002. **106**(23): p. 5982-5987.
95. Schmitt, J., et al., *Preparation and optical properties of colloidal gold monolayers.* Langmuir, 1999. **15**(9): p. 3256-3266.
96. Schelm, S., et al., *Double Effective Medium Model for the Optical Properties of Self-Assembled Gold Nanoparticle Films Cross-Linked with Alkane Dithiols.* Nano Letters, 2004. **4**(2): p. 335-339.
97. Antoine, R., et al., *Surface plasmon enhanced nonlinear optical response of gold nanoparticles at the air/toluene interface.* Chemical Communications (Cambridge), 1997(19): p. 1901-1902.
98. Okamoto, T. and I. Yamaguchi, *Optical Absorption Study of the Surface Plasmon Resonance in Gold Nanoparticles Immobilized onto a Gold Substrate by Self-Assembly Technique.* Journal of Physical Chemistry B, 2003. **107**(38): p. 10321-10324.
99. Hall, C.E., *Introduction to Electron Microscopy.* 2nd ed. 1983, Malabar: Robert E. Krieger Publishing Company.
100. Chapman, S.K., *Transmission Microscopy.* 2nd ed. Understanding & Optimising Electron Microscopy Performance. Vol. 1. 1980, London: Science Reviews Ltd.
101. Von Heimendahl, M., *Electron Microscopy of Materials: An Introduction.* Materials Science and Technology, ed. A.S. Nowick. 1980, Toronto: Academic Press.
102. Causey, G., *Electron Microscopy: A Textbook for Students of Medicine and Biology.* 1962, London: E. & S. Livingstone Ltd.
103. Mercer, E.H. and M.S.C. Birbeck, *Electron Microscopy: A Handbook for Biologists.* 3rd ed. 1972, London: Blackwell Scientific Publications.

104. Liu, Y., Y. Wang, and R.O. Claus, *Layer-by-layer ionic self-assembly of Au colloids into multilayer thin-films with bulk metal conductivity.* Chemical Physics Letters, 1998. **298**(4-6): p. 315-319.
105. Ulman, A., *Formation and Structure of Self-Assembled Monolayers.* Chemical Reviews (Washington, D. C.), 1996. **96**(4): p. 1533-1554.
106. Kumar, A., A.B. Mandale, and M. Sastry, *Sequential Electrostatic Assembly of Amine-Derivatized Gold and Carboxylic Acid-Derivatized Silver Colloidal Particles on Glass Substrates.* Langmuir, 2000. **16**(17): p. 6921-6926.
107. Hicks, J.F., S.-S. Young, and R.W. Murray, *Layer-by-layer growth of polymer/nanoparticle films containing monolayer-protected gold clusters.* Langmuir, 2002. **18**(6): p. 2288-2294.
108. Fu, Y., et al., *Fabrication of a stable polyelectrolyte/Au nanoparticles multilayer film.* Macromolecular Rapid Communications, 2002. **23**(4): p. 256-259.
109. Hao, E. and T. Lian, *Buildup of Polymer/Au Nanoparticle Multilayer Thin Films Based on Hydrogen Bonding.* Chemistry of Materials, 2000. **12**(11): p. 3392-3396.
110. Wanunu, M., A. Vaskevich, and I. Rubinstein, *Widely-Applicable Gold Substrate for the Study of Ultrathin Overlayers.* Journal of the American Chemical Society, 2004. **126**(17): p. 5569-5576.
111. Doron, A., et al., *AFM characterization of the structure of Au-colloid monolayers and their chemical etching.* Thin Solid Films, 1999. **340**(1,2): p. 183-188.
112. Tseng, J.Y., M.H. Lin, and L.K. Chau, *Preparation of colloidal gold multilayers with 3-(mercaptopropyl)-trimethoxysilane as a linker molecule.* Colloids and Surfaces, A: Physicochemical and Engineering Aspects, 2001. **182**(1-3): p. 239-245.
113. Olson, L.G., et al., *Characterization of Silane-Modified Immobilized Gold Colloids as a Substrate for Surface-Enhanced Raman Spectroscopy.* Analytical Chemistry, 2001. **73**(17): p. 4268-4276.
114. Seitz, O., et al., *Preparation and characterization of gold nanoparticle assemblies on silanized glass plates.* Colloids and Surfaces, A: Physicochemical and Engineering Aspects, 2003. **218**(1-3): p. 225-239.
115. Mougin, K., H. Haidara, and G. Castelein, *Controlling the two-dimensional adhesion and organization of colloidal gold nanoparticles.* Colloids and Surfaces, A: Physicochemical and Engineering Aspects, 2001. **193**(1-3): p. 231-237.
116. Gittins, D.I., et al., *Redox-connected multilayers of discrete gold particles. A novel electroactive nanomaterial.* Advanced Materials (Weinheim, Germany), 1999. **11**(9): p. 737-740.
117. Morita, S., R. Wiesendanger, and E. Meyer, eds. *Noncontact Atomic Force Microscopy*. ed. P. Avouris, et al. 2002, Springer.
118. Pignataro, B., et al., *The role of micro- and nanomorphology of rough silver surfaces of different nature in surface enhanced Raman scattering effect: A combined study of scanning force microscopy and low-frequency Raman modes.* Journal of Chemical Physics, 2000. **113**(14): p. 5947-5953.
119. Douketis, C., et al., *Rough silver films studied by surface enhanced Raman spectroscopy and low temperature scanning tunneling microscopy.* Progress in Surface Science, 1995. **50**(1-4): p. 187-95.

120. Brolo, A.G., et al., *Relationship between SERS Intensity and Both Surface Coverage and Morphology for Pyrazine Adsorbed on a Polycrystalline Gold Electrode.* Langmuir, 1998. **14**(2): p. 517-527.
121. Felidj, N., J. Aubard, and G. Levi, *Morphology of silver and gold "SERS active" substrates from optical spectroscopy experiments and numerical simulations.* Physica Status Solidi A: Applied Research, 1999. **175**(1): p. 367-372.
122. Wood, T.H., *Role of atomic-scale roughness in surface-enhanced Raman scattering.* Physical Review B: Condensed Matter and Materials Physics, 1981. **24**(4): p. 2289-91.
123. Brolo, A.G. and A.C. Sanderson, *Surface-enhanced raman scattering (SERS) from a silver electrode modified with oxazine 720.* Canadian Journal of Chemistry, 2004. **82**(10): p. 1474-1480.
124. Brolo, A.G., A.C. Sanderson, and A.P. Smith, *Ratio of the surface-enhanced anti-Stokes scattering to the surface-enhanced Stokes-Raman scattering for molecules adsorbed on a silver electrode.* Physical Review B: Condensed Matter and Materials Physics, 2004. **69**(4): p. 045424/1-045424/9.
125. Brolo, A.G., E. Arctander, and C.J. Addison, *Strong Polarized Enhanced Raman Scattering via Optical Tunneling through Random Parallel Nanostructures in Au Thin Films.* Journal of Physical Chemistry B, 2005. **109**(1): p. 401-405.
126. Santos, A.d.S., L. Gorton, and L.T. Kubota, *Nile blue adsorbed onto silica gel modified with niobium oxide for electrocatalytic oxidation of NADH.* Electrochimica Acta, 2002. **47**(20): p. 3351-3360.
127. Bedja, I., S. Hotchandani, and P.V. Kamat, *Photoelectrochemistry of quantized tungsten trioxide colloids: electron storage, electrochromic, and photoelectrochromic effects.* Journal of Physical Chemistry, 1993. **97**(42): p. 11064-70.
128. Gorton, L., *Chemically modified electrodes for the electrocatalytic oxidation of nicotinamide coenzymes.* Journal of the Chemical Society, Faraday Transactions 1: Physical Chemistry in Condensed Phases, 1986. **82**(4): p. 1245-58.
129. Hagfeldt, A. and M. Graetzel, *Light-Induced Redox Reactions in Nanocrystalline Systems.* Chemical Reviews (Washington, D. C.), 1995. **95**(1): p. 49-68.
130. Vogel, E., A. Gbureck, and W. Kiefer, *Vibrational spectroscopic studies on the dyes cresyl violet and coumarin 152.* Journal of Molecular Structure, 2000. **550-551**: p. 177-190.
131. Steinhurst, D.A. and J.C. Owrutsky, *Second harmonic generation from oxazine dyes at the air/water interface.* Journal of Physical Chemistry B, 2001. **105**(15): p. 3062-3072.
132. Pavia, D.L., G.M. Lampman, and G.S. Kriz, *Introduction to Spectroscopy.* 1996: Harcourt.
133. Du, H., et al., *Photochem CAD: a computer-aided design and research tool in photochemistry.* Photochemistry and Photobiology, 1998. **68**(2): p. 141-142.
134. Mulvaney, S.P. and C.D. Keating, *Raman Spectroscopy.* Analytical Chemistry, 2000. **72**(12): p. 145-157.
135. Vlckova, B., X.J. Gu, and M. Moskovits, *SERS Excitation Profiles of Phthalazine Adsorbed on Single Colloidal Silver Aggregates as a Function of Cluster Size.* Journal of Physical Chemistry B, 1997. **101**(9): p. 1588-1593.

136. Poliakov, E., et al., *Enhancement of nonlinear processes near rough nanometer-structured surfaces obtained by deposition of fractal colloidal silver aggregates on a plain substrate.* Physical Review B: Condensed Matter and Materials Physics, 1999. **60**(15): p. 10739-10742.
137. Jana, N.R., *Silver coated gold nanoparticles as new surface enhanced Raman substrate at low analyte concentration.* Analyst (Cambridge, United Kingdom), 2003. **128**(7): p. 954-956.
138. Srinivasan, R. and I.I. Suni, *Electroless deposition of Au onto Si(11) studied by surface second harmonic generation.* Surface Science, 1998. **408**(1-3): p. L698-L702.
139. Srinivasan, R. and I.I. Suni, *Kinetic analysis of Au deposition from aqueous HF onto Si(111) by surface second harmonic generation.* Journal of the Electrochemical Society, 1999. **146**(2): p. 570-573.
140. Chen, C.K., A.R.B. De Castro, and Y.R. Shen, *Surface-enhanced second-harmonic generation.* Physical Review Letters, 1981. **46**(2): p. 145-8.
141. Chen, C.K., et al., *Surface-enhanced second-harmonic generation and Raman scattering.* Physical Review B: Condensed Matter and Materials Physics, 1983. **27**(4): p. 1965-79.
142. Poliakov, E.Y., et al., *Nonlinear optical phenomena on rough surfaces of metal thin films.* Physical Review B: Condensed Matter and Materials Physics, 1998. **57**(23): p. 14901-14913.
143. Brasselet, S., et al., *Sub-microscopic probing of intrinsic and extrinsic enhancement of second harmonic generation of nano-structured gold surfaces.* NATO Science Series, II: Mathematics, Physics and Chemistry, 2003. **100**(Organic Nanophotonics): p. 339-353.
144. Shalaev, V.M. and A.K. Sarychev, *Nonlinear optics of random metal-dielectric films.* Physical Review B: Condensed Matter and Materials Physics, 1998. **57**(20): p. 13265-13288.
145. Rossiter, C. and I.I. Suni, *Atomic force microscopy of Au deposition from aqueous HF onto Si(111).* Surface Science, 1999. **430**(1-3): p. L553-L557.
146. Bruzzone, S., G.P. Arrighini, and C. Guidotti, *Some spectroscopic properties of gold nanorods according to a schematic quantum model founded on the dielectric behavior of the electron-gas confined in a box. I.* Chemical Physics, 2003. **291**(2): p. 125-140.
147. Link, S., M.B. Mohamed, and M.A. El-Sayed, *Simulation of the optical absorption spectra of gold nanorods as a function of their aspect ratio and the effect of the medium dielectric constant.* Journal of Physical Chemistry B, 1999. **103**(16): p. 3073-3077.
148. Raether, H., *Surface Plasmons: On Smooth and Rough Surfaces and on Gratings.* Springer Tracts in Modern Physics, ed. G. Hohler. Vol. 111. 1988, New York: Springer-Verlag.
149. Wang, H., et al., *Second harmonic generation from the surface of centrosymmetric particles in bulk solution.* Chemical Physics Letters, 1996. **259**(1,2): p. 15-20.

150. Link, S., et al., *Laser-Induced Shape Changes of Colloidal Gold Nanorods Using Femtosecond and Nanosecond Laser Pulses.* Journal of Physical Chemistry B, 2000. **104**(26): p. 6152-6163.
151. Jana, N.R., L. Gearheart, and C.J. Murphy, *Wet chemical synthesis of high aspect ratio cylindrical gold nanorods.* Journal of Physical Chemistry B, 2001. **105**(19): p. 4065-4067.
152. Yu, Y.-Y., et al., *Gold nanorods: electrochemical synthesis and optical properties.* Journal of Physical Chemistry B, 1997. **101**(34): p. 6661-6664.
153. Leontidis, E., et al., *Gold Colloids from Cationic Surfactant Solutions. 1. Mechanisms That Control Particle Morphology.* Langmuir, 2002. **18**(9): p. 3659-3668.
154. Nikoobakht, B. and M.A. El-Sayed, *Evidence for Bilayer Assembly of Cationic Surfactants on the Surface of Gold Nanorods.* Langmuir, 2001. **17**(20): p. 6368-6374.
155. Nikoobakht, B., J. Wang, and M.A. El-Sayed, *Surface-enhanced Raman scattering of molecules adsorbed on gold nanorods: off-surface plasmon resonance condition.* Chemical Physics Letters, 2002. **366**(1,2): p. 17-23.
156. Link, S., et al., *Laser Photothermal Melting and Fragmentation of Gold Nanorods: Energy and Laser Pulse-Width Dependence.* Journal of Physical Chemistry A, 1999. **103**(9): p. 1165-1170.
157. Mohamed, M.B., et al., *Thermal Reshaping of Gold Nanorods in Micelles.* Journal of Physical Chemistry B, 1998. **102**(47): p. 9370-9374.
158. Nikoobakht, B. and M.A. El-Sayed, *Surface-Enhanced Raman Scattering Studies on Aggregated Gold Nanorods.* Journal of Physical Chemistry A, 2003. **107**(18): p. 3372-3378.
159. Wang, D.S. and M. Kerker, Physical Review B: Condensed Matter and Materials Physics, 1981. **24**: p. 1777.
160. Wang, Z.L., et al., *Crystallographic facets and shapes of gold nanorods of different aspect ratios.* Surface Science, 1999. **440**(1-2): p. L809-L814.
161. Fleichmann, M. and I.R. Hill, in *Surface Enhanced Raman Scattering*, R.K. Chang and T.E. Furtak, Editors. 1982, Plenum Press: New York. p. 280.
162. Wang, Z.L., et al., *Surface reconstruction of the unstable {110} surface in gold nanorods.* Journal of Physical Chemistry B, 2000. **104**(23): p. 5417-5420.
163. Suzuki, M., et al., *Surface-enhanced nonresonance raman scattering of rhodamine 6G molecules adsorbed on gold nanorod films.* Japanese Journal of Applied Physics, Part 2: Letters & Express Letters, 2004. **43**(4B): p. L554-L556.
164. Caswell, K.K., et al., *Preferential end-to-end assembly of gold nanorods by biotin-streptavidin connectors.* Journal of the American Chemical Society, 2003. **125**(46): p. 13914-13915.
165. Dujardin, E., et al., *DNA-driven self-assembly of gold nanorods.* Chemical Communications (Cambridge, United Kingdom), 2001(14): p. 1264-1265.
166. Storhoff, J.J., et al., *One-Pot Colorimetric Differentiation of Polynucleotides with Single Base Imperfections Using Gold Nanoparticle Probes.* Journal of the American Chemical Society, 1998. **120**(9): p. 1959-1964.

From: CONTRACTS-COPYRIGHT (shared) [Contracts-Copyright@rsc.org]
Sent: Thursday, May 12, 2005 2:14 AM
To: cja@uvic.ca
Subject: RE: Permission Request Form: Chris Addison

Dear Dr Addison

The Royal Society of Chemistry hereby grants permission for the use of the material specified below in the printed or microfilm version of your thesis, via any restricted internal website that your university may have for the deposition of theses, via your university's Intranet or via your own personal website. The Royal Society of Chemistry is a signatory to the STM Guidelines on Permissions (available on request).

Please note that if the material specified below or any part of it appears with credit or acknowledgement to a third party then you must also secure permission from that third party before reproducing that material.

Please ensure that the published article carries a credit to The Royal Society of Chemistry in the following format:

[Original citation] - Reproduced by permission of The Royal Society of Chemistry

Regards

Alice Chapman
Contracts & Copyright Executive

Alice Chapman, Contracts & Copyright Executive
Royal Society of Chemistry, Thomas Graham House
Science Park, Milton Road, Cambridge CB4 0WF, UK
Tel +44 (0) 1223 432134, Fax +44 (0) 1223 423623 http://www.rsc.org and
http://www.chemsoc.org

-----Original Message-----
From: cja@uvic.ca [mailto:cja@uvic.ca]
Sent: 12 May 2005 05:53
To: CONTRACTS-COPYRIGHT (shared)
Subject: Permission Request Form: Chris Addison

Name : Chris Addison
Address :

Department of Chemistry
University of Victoria
PO Box 3065
Victoria, BC, Canada
V8W 3V6

Tel : (250)472-4908
Fax : (250)721-7147
Email : cja@uvic.ca

I am preparing the following work for publication:

Article/Chapter Title : n/a
Journal/Book Title : Three-dimensional Colloidal Gold Nanostructures

Editor/Author(s) : Christopher J. Addison
Publisher : University of Victoria

I would very much appreciate your permission to use the following material:

Journal/Book Title : Chemical Society Reviews
Editor/Author(s) : Campion, Alan; Kambhampati, Patanjali
Volume Number : 27
Year of Publication : 1998
Description of Material : Figure 1
Page(s) : 241-250

Any Additional Comments :

I am seeking to include Figure 1 of the above-mentioned article in my Master's thesis. Appropriate credit will be given.

425·125
YEARS OF PUBLISHING
TRADITION | EXCELLENCE

We commemorate the founding of the House of Elsevir in 1580 and celebrate the establishment of the Elsevier company in 1880.

ELSEVIER

23 May 2005

Our ref: HG/HDN/MAY05/J104

Mr Chris J Addison
University of Victoria
PO Box 3065
Victoria, V8W 3V6
Canada

Dear Mr Addison

***THIN SOLID FILMS, Vol 340, No 1 – 2, 1999, pp 183 – 188, Doron et al, "AFM Characterization...", 1 Figure Only***

As per your letter dated 3rd May 2005, we hereby grant you permission to reprint the aforementioned material at no charge **in your thesis** subject to the following conditions:

1. If any part of the material to be used (for example, figures) has appeared in our publication with credit or acknowledgement to another source, permission must also be sought from that source. If such permission is not obtained then that material may not be included in your publication/copies.

2. Suitable acknowledgment to the source must be made, either as a footnote or in a reference list at the end of your publication, as follows:

   "Reprinted from Publication title, Vol number, Author(s), Title of article, Pages No., Copyright (Year), with permission from Elsevier".

3. Reproduction of this material is confined to the purpose for which permission is hereby given.

4. This permission is granted for non-exclusive world **English** rights only. For other languages please reapply separately for each one required. Permission excludes use in an electronic form. Should you have a specific electronic project in mind please reapply for permission.

5. This includes permission for the National Library of Canada to supply single copies, on demand, of the complete thesis. Should your thesis be published commercially, please reapply for permission.

Yours sincerely

H Gainford

Helen Gainford
Rights Manager

**Your future requests will be handled more quickly if you complete the online form at**
**www.elsevier.com/locate/permissions**

From: customercare@copyright.com
Sent: Tuesday, May 10, 2005 12:14 PM
To: cja@uvic.ca
Subject: Thank you for your Rightslink / AVS The Science & Technology Society order

Importance: High

Thank you for placing your order through Copyright Clearance Center's Rightslink service. AVS The Science & Technology Society has partnered with Copyright Clearance Center's Rightslink service to license its content online. Note: Payee for this order is Copyright Clearance Center.

http://s100.copyright.com/CustomerAdmin/PrintableLicenseFrame.jsp?licenseID=2005050_1115752459493

Order Information
Licensee: Chris Addison
Order Date: May 10, 2005
License Number: 1225500859493
Publication: Journal of Vacuum Science & Technology A
Title: Nanosphere lithography: A materials general fabrication process for periodic particle array surfaces Type Of Use: Republish Portions
Cost: $0.00

The following credit line must appear with your reuse of this material: Reprinted with permission from John C. Hulteen, Journal of Vacuum Science & Technology A, 13, 1553 (1995). Copyright 1995, AVS The Science & Technology Society.

To access your account, please visit https://myaccount.copyright.com.

If you have any comments or questions, please contact Rightslink:

Copyright Clearance Center
Rightslink
Tel (toll free): 877/622-5543
Tel: 978/777-9929
E-mail: mailto:customercare@copyright.com
Web: http://www.copyright.com

v1.9

--